CHARACTERIZATION AND SIMULATION OF AN ADVANCED MICROCELLULAR INJECTION MOLDING TECHNIQUE FOR COMPOSITE AUTOMOTIVE COMPONENTS

by

Sara Andrea Simon

A dissertation submitted in partial fulfillment of
the requirements for the degree of

Doctor of Philosophy

(Mechanical Engineering)

at the

UNIVERSITY OF WISCONSIN–MADISON

2022

Date of final oral examination: 10/25/2022

The dissertation is approved by the following members of the Final Oral Committee:
Tim A. Osswald, Professor, Mechanical Engineering,
Lih-Sheng Turng, Professor, Mechanical Engineering
Pavana Prabhakar, Professor, Civil and Environmental Engineering
Lianyi Chen, Professor, Mechanical Engineering
Alejandro Roldan Alzate, Professor, Mechanical Engineering

Abstract

Increasing demand for lightweight and economical automotive components boosts development of advanced materials and new lightweighting technologies. This work employed both, discontinuous glass fiber-reinforced thermoplastics and the new microcellular injection molding technology Ku-Fizz™. To study this foaming process and make it a competitive technology for the automotive industry, correlations between processing conditions and the final microstructure need to be available to process and design engineers. The pressure-operating window, its corresponding effect on foam microstructure, and its relation to mechanical properties were studied. It was found that cell nucleation and growth modified the existing fiber microstructure. No modeling techniques are available to predict the foam microstructure of parts foamed with alternatives microcellular injection molding technologies, such as Ku-Fizz™. Therefore, a new approach is presented. First, the microcellular foaming tool in the mold filling simulation software Moldex3D was evaluated by correlating experimental with predicted foam microstructural data. Then, controlled studies were performed to determine correlations between pressures in the Ku-Fizz™ hopper unit and measured pressures in the plasticating unit to find an appropriate simulation input. A relationship was found and the models in Moldex3D were updated. The updated model was validated by predicting the foam microstructure in a SCANIA AB truck door panel with a margin of error of less than 20% error.

Acknowledgements

First and foremost, I am extremely grateful to my advisor and mentor, Prof. Tim A. Osswald for his invaluable advice, and continuous support during my PhD and for all the opened opportunities to grow as a researcher.

I would like to extend my sincere gratitude to the members of my dissertation committee: Prof. Lih-Sheng Turng, Prof., Pavana Prabhakar, Prof. Lianyi Chen, and Prof. Alejandro Roldán-Alzate for their insightful comments and suggestions.

I want to express my appreciation to all research assistants that supported me throughout my research work. This research was funded by Volkswagen, and I would like to express my gratitude for sponsoring this exciting project. Thank you, Jörg Hain and Dr. Christoph Kuhn for your support and advice.

In addition, I would like to thank all the members of the Polymer Engineering Center. It is their friendship, discussion of ideas, critical feedback, and support that helped me to be at this point today. Finally, I would like to express my gratitude to my family and my husband. Abrahan, thank you for your encouragement in the past few years to help me rise to this challenge.

Table of Contents

List of Figures

List of Tables

List of Abbreviations

Abbreviation	Meaning
GHG	Greenhouse gas
μCT	Micro-computed tomography
AMI	Algorithm of mode isolation
BEV	Battery electric vehicles
CD	Cell density
CF	Carbon fiber
CS	Cell size
DMA	Dynamic mechanical analysis
DSC	Differential scanning calorimetry
FC	Fiber concentration
FEA	Finite element analysis
FL	Fiber length
FLD	Fiber length distribution
FLD	Fiber length distribution
FO	Fiber orientation
FP	Fitting parameter
FPD	Fitting parameter determination
FRF	Frequency response functions
GF	Glass fiber
HDPE	High-density polyethylene
Hz	Hertz
IM	Injection Molding
LDPE	Low-density polyethylene
LFT	Long fiber-reinforced thermoplastics
LGF	Long glass fiber
MAC	modal assurance criterion

MAC	Modal assurance criterion
MF	Multi-phase
MIM	Microcellular injection molding
MIT	Massachusetts Institute of Technology
MS	Microstructure
MS	Microstructure
N_2	Nitrogen gas
OEM	Original equipment manufacturer
PBA	Physical blowing agent
PE	Polyethylene
PP	Polypropylene
PPGF	Glass fiber-reinforced polypropylene
PS	Polystyrene
ROI	Region of interest
RVE	Representative volume element
SABIC	Saudi Basic Industries Corporation
SCF	Super critical fluid
VW	Volkswagen

List of Symbols

Symbol	Meaning
F_{AD}	Aerodynamic resistance
F_{RR}	Rolling resistance
F_{GR}	Gradient resistance
F_{AD}	Aerodynamic resistance
F_{ACC}	Acceleration resistance
ρ	Density
C_D	Aerodynamic drag coefficient
v	velocity
A_f	Car frontal area
f_{RR}	Rolling resistance ce
g	Gravity
m_V	Vehicle mass
I	Moment of Inertia
α	Road gradient
a	Vehicle acceleration
m	Mass of diffusing tissue
$tan\delta$	Damping property
E	Elastic modulus
E'	Storage modulus
E/ρ	Normalized specific modulus
t	Time
D	Diffusion coefficient
A	Area
ρ	Density
c	Concentration
D_0	Constant for gas/polymer system

E_d	Activation energy of diffusion
R_g	Gas constant
T	Temperature
S	Solubility coefficient
P_m	Melt pressure
T_{poly}	Temperature of melt
S_0	Preexponential solubility constant
E_s	Solution of enthalpy
G_{hom}	Free energy
R, r	Radius
γ_{bp}	Interfacial surface tension of bubble/polymer
r^*	Critical radius
N_{hom}	Homogenous nucleation rate
C_0	Gas concentration in solution
f_0	Fitting parameter
G^*_{hom}	Maximum Gibb's free energy
K	Boltzmann constant
Z	Zeldovich factor
β	Rate of added molecules to nucleus
G_{het}	Gibbs's free energy
A_{bp}	Bubble/polymer interface
A_{ab}	Additive/bubble interface
A_{ap}	Additive/polymer interface
γ_{ab}	Interfacial surface tension of additive/bubble
γ_{ap}	Interfacial surface tension of additive/polymer
N_{het}	Heterogenous nucleation
C_1	Concentration of heterogeneous nucleation sites
f_1	Frequency factor for heterogeneous nucleation
G^*_{het}	Critical change in free energy

θ_w	Angle between polymer/gas/additive
$\mathbf{u}$	Velocity vector
η	Viscosity
C_p	Specific heat
$\mathbf{k}$	Thermal conductivity tensor
$\dot{\gamma}$	Shear rate
P_D	Gas pressure inside bubble
P_c	Melt pressure at outer boundary of bubble
γ	Surface Tension
P_{sat}^*	Gas saturation pressure
$J(t)$	Nucleation rate
R_0	Initial cell size
c_∞	Gas concentration for away from cell
c_R	Gas concentration on cell wall
δ	Concentration boundary thickness
F	Fitting parameter
$\mathrm{M_w}$	Gas molecular weight
N_A	Avogadro number
$\bar{c}$	Average dissolved gas concentration in polymer
k_H	Solubility parameter
V_{L0}	Volume of polymer matrix
L_N	Number average fiber length
L_W	Weight average fiber length
ω_n	Natural Frequency associated with the n^{th} -mode
α_n	Eigenvalue
$H(\omega)$	Frequency response functions
Im	Imaginary part
Re	Real part
M_t	Quantity of diffusing substance

M_∞	Quantity of diffusing substance at t_∞
J_0	Bessel functions of the first kind of order zero
α_n	Roots of Bessel functions of the first kind of order zero
S_c	Corrected solubility
X_c	Extent of crystallinity
X_a	Gas solubility in amorphous region
P_{hopper}	Hopper pressure
P_{nozzle}	Nozzle pressure
E	Elastic modulus

1 Introduction

1.1 Lightweighting in Automotive

The transportation sector is the largest contributor of greenhouse gas (GHG) emissions in the United States, with 28% of the total amount. Within this sector, light-duty vehicles constitute 59% of all GHG emissions [1]. Any moving vehicle experiences energy losses due to air resistance, rolling, acceleration and gradient, as shown in Figure 1.1. Driving resistances directly affect required fuel consumption, and thus, CO_2 emissions [2]. Except for aerodynamic resistance, the energy required to move a car is directly proportional to its mass.

$$F_{AD} = \frac{\rho_{Air}}{2} * C_D * v^2 * A_f$$

$$F_{RR} = m_V * f_{RR} * g * \cos(\alpha)$$

$$F_{GR} = m_V * g * \sin(\alpha)$$

$$F_{ACC} = (m_V * I_{RP}) * a$$

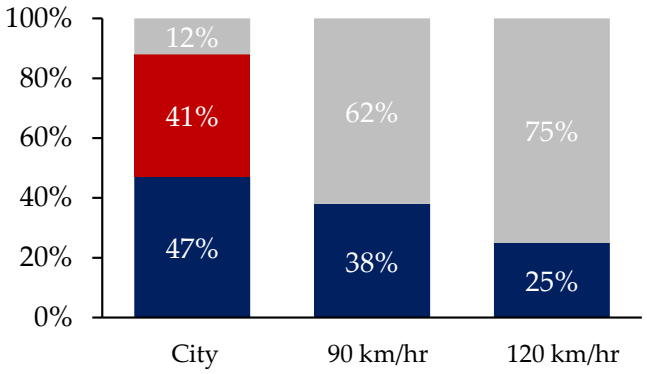

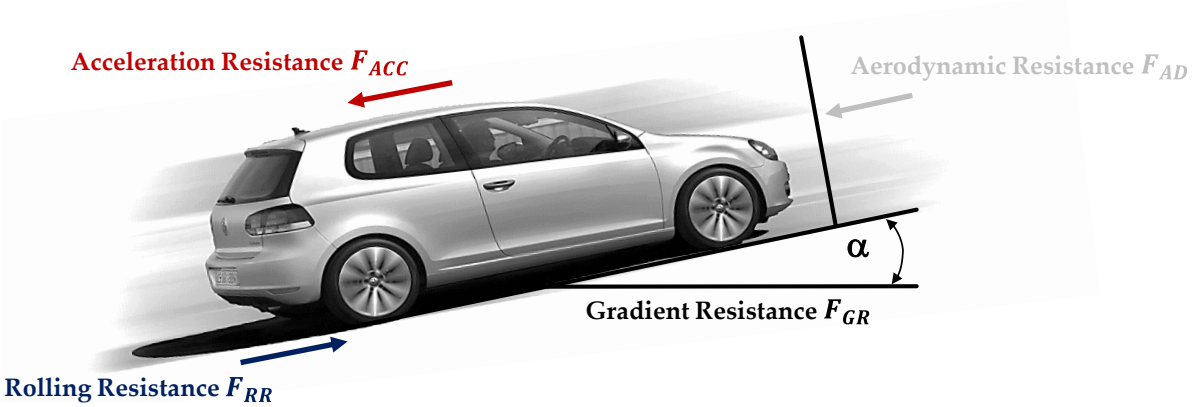

Figure 1.1. Resistances experienced by a moving car. Modified from [2,3].

Reducing driving resistances contributes considerably to reach emission targets [2]. However, this requires car manufacturers to re-work traditional vehicle concepts. Efforts include developing new rubber compounds for tires and prohibiting tires with high rolling resistance coefficients, incorporating vehicle body designs that allow the car to be smoother and more streamlined, and reducing power train losses with sealing optimization, electrification, and downsizing. Fuel saving potentials through vehicle mass

have not been fully exploited yet [4]. A 20% reduction in vehicle weight results in a 9% fuel economy improvement as less energy is required to accelerate a lighter object (Figure 1.2) [5]–[7].

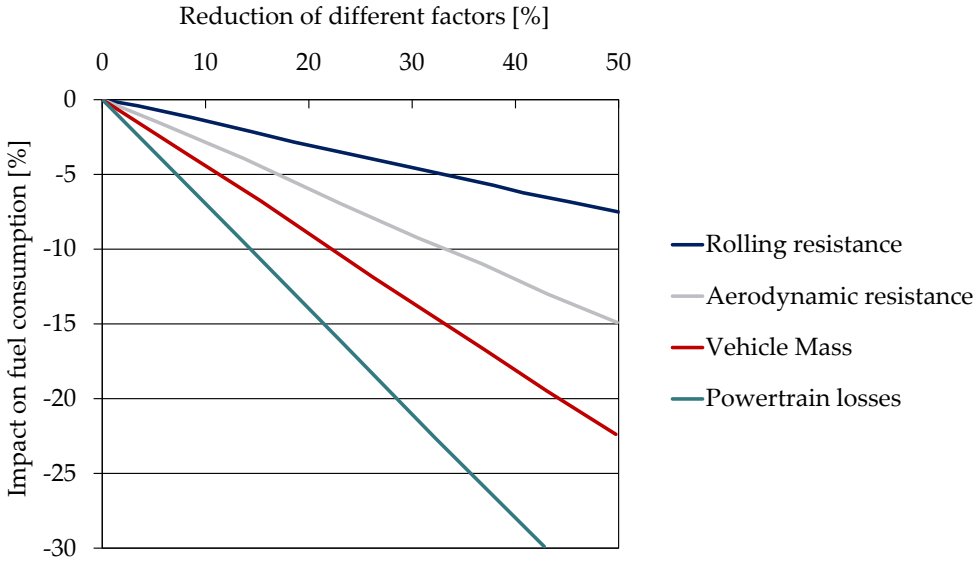

Figure 1.2. Effect of resistances on fuel consumption. Modified from [8].

As more efficient engines, electrical powertrains and sleeker vehicle bodies will not carry the whole load, OEMs are compelled to develop new lightweighting technologies and investigate advanced materials to meet the stringent governmental regulations. One option is to retrofit existing structures made of steel with materials such as high-strength steel, aluminum, magnesium, composites and plastics due to their lightweighting potential [9]. Long fiber-reinforced thermoplastics (LFTs) have gained wide acceptance in the automotive industry due to their high performance in terms of mechanical properties, resistance to numerous corrosive media, low density, and ability to be shaped and tailored to satisfy performance requirements [10]–[13]. In addition of using advanced materials, car manufacturers also investigate new technologies to reduce the vehicle weight even further. Introducing gas into the polymer, commonly known as microcellular injection molding (MIM), can cut back the weight by an additional 15% as a cellular structure is created within the molded part [14], [15].

Physical foam molding has demonstrated its potential in the automotive industry [14]–[22]. Specifically, the MIM technology MuCell® has gained popularity and acceptance among car manufacturers. The technology employs a physical blowing agent (PBA) which is introduced as a supercritical fluid (SCF) into the polymer melt. Injection of the gas laden melt into the mold cavity induces cell nucleation. Cells grow until the melt freezes [14], [23]–[25]. MuCell has been utilized for visible and non-visible parts in the vehicle sector. The center console of the Mercedes-Benz C-Class (W 205) was produced with the MuCell technology

and a weight reduction of 20% was reported (Figure 1.3) [17]. Ford foamed an instrument panel for the 2012 Ford Escape/Kuga and recorded 0.5 kg saving in materials, 15% reduced cycle times, and a total part cost of 3$/vehicle. The Inalfa Roof Systems Group molded a one-piece short glass-PP integrated sunroof module for the 2010 Cadillac CTS (Figure 1.3). The part achieved 12% weight savings versus the traditional four-piece design and a 15 sec reduction in cycle time. Johnson Controls foamed an interior door trim panel for a European automaker which reduced production expenses by 50% [22]. Volkswagen developed a foamed instrument panel for the VW Golf 7, which also exhibited a 0.5 kg weight reduction versus the prior model [18]. Engel also foamed an instrument panel which will be shown at this year's K 2022 (Figure ***1.3***) [21].

Instrument Panel | Sunroof Module Cadillac CTS | Center console Mercedes Benz C-Class car (W 205)

Figure 1.3. Microcellular foamed automotive components.

Even though foamed components show advantages over their compact counterparts, their potential is hardly utilized yet. One reason is that the path from concept to a reliable series production is long and requires elaborate research and development work [17]. Additionally, upgrading injection molding (IM) machines to offer MIM capabilities requires a high upfront capital investment. As an example, the upgrade costs for a Krauss Maffei KM 650-4300 CX IM machine are 35% of the machine cost [26]. Required modifications include a plasticizing unit with a specially designed screw to generate a single-phase solution and a SCF metering, delivery, and dosing system. These modifications lead to additional complexity in controlling the process [15], [27], [28]. All these limits the implementation of MIM techniques in practice [12,18–20].

1.2 Basics of Microcellular Injection Molding

1.2.1 Basic Considerations

The traditional MIM process can be divided into four steps: generation of a single-phase solution, cell nucleation, cell growth, and part shaping [14]. In a first step SCF is injected into the polymer melt during plasticization. Injection of the gas laden melt into the mold cavity induces cell nucleation due to the thermodynamic instability generated by a rapid change in pressure. Cells grow until the melt freezes or until the gas concentration inside the bubbles equals that of the melt [16]. A cellular structure within the plastic part is created with cell densities (CD) as high as 10^9 cells/cm^3 and cell sizes (CS) in the order of 10 μm [23]–[25]. Figure 1.4 illustrates the steps in MIM.

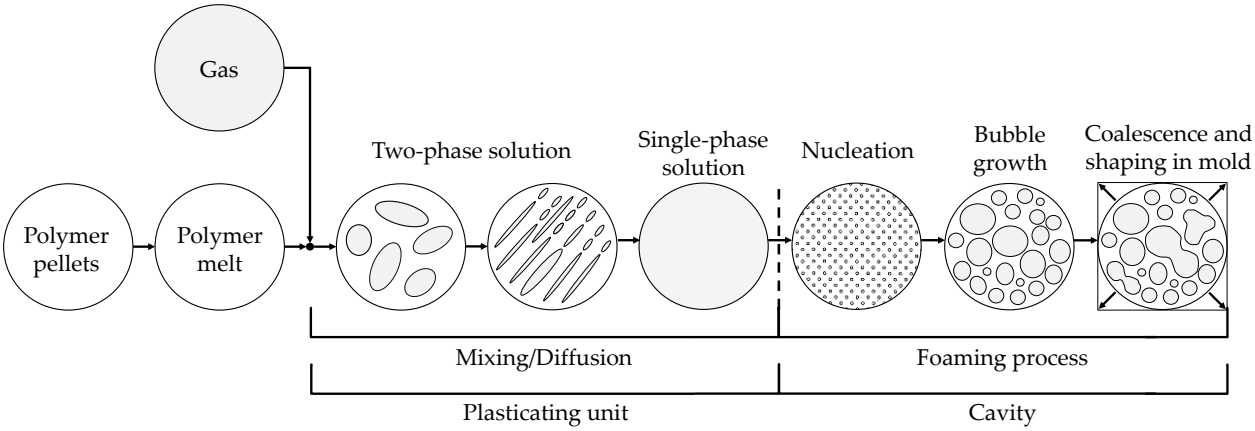

Figure 1.4: Schematic description of the physical MIM process. Modified from [30]–[33].

1.2.2 Gas Mixing and Dissolution

During SCF injection, big gas droplets are formed as the gas flow is briefly interrupted every time the screw flight wipes over the barrel. The size of these droplets heavily depends on gas pressure, gas flow rate, polymer viscosity and screw rotational speed. Due to drag flow at the top of the screw channel and pressure back flow at the bottom of the channel, a strong shearing field is present. The gas droplet will be elongated until reaching the critical Weber number. As the surface tension is overcome by shear force, droplets will break up forming many small gas bubbles. Xu found that the Weber-Number increases 5-times when the screw speed increases 3-times [34]. Shear deformation will once again elongate bubbles, increasing the area-to-volume ratio, thus decreasing striation thickness of the polymer between gas droplets. This accelerates gas diffusion rate. Ideally, an entire dissolution of sheared gas pockets occurs, creating a single-phase

solution. Due to short screw recovery times and even shorter gas-polymer mixing times a single-phase solution is mostly not formed [35]–[37].

MIM technologies usually employ gases in supercritical states to increase solubility and diffusion rates. At this state gases show liquid-like properties, such as heavy liquid-like densities as well as gas-like properties including low viscosity and surface tension. The ability of a polymer to uptake gas is described by its solubility. Diffusivity is the rate at which gas molecules moves through molten polymer driven by concentration, pressure, and temperature differences [14], [37], [38].Experimental and theoretical techniques exist to determine the diffusivity and solubility of gases in polymers.

The transport mechanism of the SCF within the polymer is described by diffusivity. The diffusivity is linked to molecules moving through the polymer melt [14], [38]. Experimental approaches to determine diffusivity include pressure-decay methods, gravimetric methods, and permeation methods for steady state diffusion. Theoretical methods exist for steady and unsteady diffusion [39], [40]. The speed at which concentration differences are equalized for a 1D mass transport can be described by Ficks's first law of diffusion

$$\frac{dm}{dt} = -DA\rho\frac{dc}{dx} \tag{1}$$

where m is the mass of the diffusing tissue, t the time, A the area, ρ the density, c the concentration, x a direction coordinate, and D the diffusion coefficient which is described by an Arrhenius function as follows

$$D = D_0\, e^{-\frac{E_d}{R_g T}} \tag{2}$$

where D_0 the constant for the polymer-gas system, E_d the activation energy for diffusion, R_g the ideal gas constant, and T the absolute temperature [35], [40]–[42]. Equation 1 states that the higher concentration difference, the faster the mass transportation. Equation 2 shows that diffusion speed increases with temperature following an Arrhenius relationship. Additionally, the higher the crystallinity, the lower the diffusivity [42].

It needs to be noted that during gas diffusion, there is a point where a saturation limit is reached [38]. There are experimental methods for solubility determination including gravimetric, piezoelectric, manometric, chromatographic, and spectroscopic methods as well as theoretical thermodynamic approaches including Flory-Huggins, Sanchez-Lacombe, Simha-Somcynsky, and statistical association fluid theories [39], [41], [43]. A simplified model which can describe absorption processes is Henry's law:

$$C = S\left(P_m, T_{poly}\right) P_m \tag{3}$$

where C represents the concentration of dissolved gas in polymer, P_m the molten polymer pressure, T_{poly} the molten polymer temperature, and S the solubility coefficient which is described by an Arrhenius function as follows

$$S(t) = S_0 \, e^{-\frac{E_s}{R_g T}} \tag{4}$$

with S_0 as the preexponential constant, E_s as heat of solution (=solution of enthalpy), R_g a gas constant, and T as the temperature [14], [24], [42], [44]. Equation 3-4 indicate that solubility increases with higher pressure and decreases with higher temperatures.

Molecular simulations can also be used to obtain solubility and diffusion coefficients [45], [46]. Several researchers have studied the solubility and diffusivity of gases in polymer melts. Sato et al., measured solubility and diffusion coefficients of N_2 and CO_2 in PP, HDPE and PS [41], [47]–[49]. Aionicesei et al. investigated the solubility of several gases into PP, LDPE, PS, PE and HDPE [50], [51]. Li et al., determined the solubility of N_2 and CO_2 in linear/branches PP [43], [52]. Wang et al, determined the solubility and diffusion coefficient of CO_2 in PS dynamic melt [40].

1.2.3 Cell Nucleation

When the gas-polymer mixture is injected into the cavity, many nucleation sites form due to the pressure drop from the sprue to the mold cavity. This rapid thermodynamic instability causes solubility to decrease, and the polymer melt to becomes supersaturated with PBA. The PBA will subsequently separate from the single-phase solution, and nuclei are generated [14], [31], [53]. Nucleation is divided into homogenous and heterogenous nucleation. It has been shown that for typical MIM processes the rate of homogenous nucleation is negligible and heterogenous nucleation is dominant due to the presence of impurities, additives, and fillers [54]–[56].

The classical nucleation theory is based on Gibbs free energy required for creating a bubble in a liquid, and centers around the concept of a critical bubble in mechanical and thermodynamic equilibrium with the surrounding liquid [57], [58]. The change in Gibb's free energy assuming no shearing and spherical bubbles is given by

$$\Delta G_{hom} = -\frac{4}{3}\pi r^3 \Delta p + 4\pi r^2 \gamma_{bp} \tag{5}$$

where G_{hom} represents the change in free energy, r the bubble radius, Δp the gas bubble pressure, and γ_{bp} the surface tension [14]. Cells below the critical bubble size will collapse and re-dissolve, whereas cells larger than the critical bubble size are stable and will grow further. Figure 1.5 displays the relationship between ΔG_{hom} and r. The creation of a small bubble increases until the radius of the nucleated cell is larger than a critical size (r^*). The critical size occurs when $\frac{dG}{dr} = 0$. If $r < r^*$, the system can lower its free energy by the dissolution of nuclei. If $r > r^*$ cells are stable and grow, and bubble growth leads to a reduction of free energy [14], [56], [59], [60]. The interfacial energy (second term equation 5) increases quadratically with the radius, whereas the free energy (first term equation 5) decreases proportional to r^3 [59].

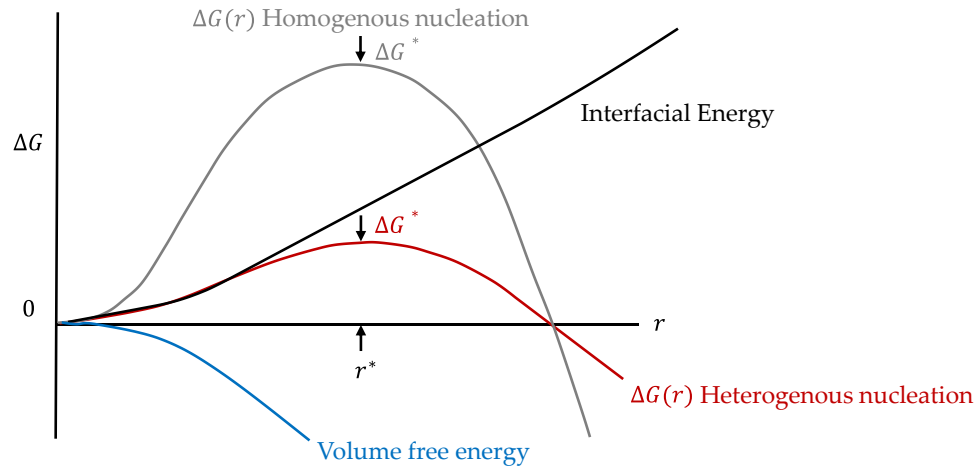

Figure 1.5. Free energy as a function of nucleus radius during homogenous and heterogenous nucleation. Modified from [14]

The homogenous nucleation rate can be expressed by

$$N_{hom} = C_0 f_0 e^{\frac{-\Delta G^*_{hom}}{KT}} \tag{6}$$

where N_{hom} is the number of nuclei created per volume and second, C_0 the concentration of gas molecules in solution, f_0 the frequency factor, G^*_{hom} the maximum Gibb's free energy, K the Boltzmann's constant, T the absolute temperature.

$$\Delta G^*_{hom} = \frac{16\pi}{3\Delta P^2}\gamma^3_{bp} \tag{7}$$

$$f_0 = Z\beta \tag{8}$$

$$\beta = (4\pi r^{*3})R_1 \tag{9}$$

where γ_{bp} is the interfacial surface tension of the bubble/polymer, Z the Zeldovich factor, and β the rate of added molecules to the nucleus [14].

For heterogenous nucleation, less energy is required for cell nucleation (Figure 1.5). Colton et al., 1987, reported that filled materials have a higher chance to start a stable nucleation compared to neat materials [61]. It has been shown that for MIM processes the rate of homogenous nucleation is negligible and heterogenous nucleation is dominant due to the presence of impurities, additives, and fillers [14], [54], [55]. Tatibouët et al., found that dissolved gas tends to aggregate on the surface of nucleating agents which then become nucleation sites during foaming [62]. Sykutera et al., and Leung et al., also showed that fibers act as heterogenous nucleation sites as they provide crevices to trap gas and from nuclei [62]–[64].

This leads to the following expression for heterogenous nucleation

$$\Delta G_{het} = -V_b \Delta P + A_{bp}\gamma_{bp} + A_{ab}\gamma_{ab} - A_{ap}\gamma_{ap} \tag{10}$$

where G_{het} is the change of Gibbs's free energy, A_{bp}, A_{ab}, and A_{ap} are bubble/additive interfaces with the polymer, and γ_{bp}, γ_{ab}, and γ_{ap} are interfacial surface tension of the bubble/additive and polymer. The rate of nucleation is then described as

$$N_{het} = C_1 f_1 e^{\frac{-\Delta G^*_{het}}{KT}} \tag{11}$$

$$\Delta G^*_{het} = \frac{16\pi}{3\Delta p^2}\gamma^3_{bp} S(\theta_w) \tag{12}$$

where N_{het} represents the rate of heterogeneous nucleation, C_1 the concentration of heterogeneous nucleation sites, f_1 the frequency factor for heterogeneous nucleation, G^*_{het} the critical change in free energy, and $S(\theta_w)$ a function depending on the wetting angle θ_w between polymer and gas or the second-phase particle [14].

1.2.4 Cell Growth

Once nuclei reach their critical radius, cells begin to grow due to the diffusion of gas into the cells. This growth is controlled by the temperature and pressure during the molding. Cells grow until they reach their ultimate equilibrium size (pressure inside cell and pressure of the melt are equalized) or until the melt viscosity is too high leading to suppressed cell growth [14], [59]. Bubble growth is a complex process which depends on the system's pressure and temperature, gas diffusion, hydrodynamic interactions between bubble and melt, and rheological properties of the gas/melt mixture. For example, as cells grow, gas diffusion and cell expansion promote cooling of the melt. This increases viscosity and thus, oppose cell growth [65]. As cells grow bigger the chances for cell coalescence is increased. Numerous bubble growth

models have been proposed to explain cell growth [66]. Their detailed description can be found in the Modeling chapter.

1.2.5 Part Shaping

Part shaping depends on the mold design which determines the weight reduction, warpage, surface, weld lines, cell morphology, and the skin/core architecture [14], [59]. Additionally, melt viscosity affects part shaping as well. As melt temperature decreases, bubble growth slows down and the residual gas pressure contained within the cells push the melt against the mold walls. Cell growth ends by achieving an equilibrium of forces, which is the pressure inside the cell versus the forces needed for further cell growth defined by surface forces and stresses in the viscoelastic cell wall [37], [67]. Freezing of the melt ultimately leads to fixation of the foam and to parts with characteristic skin-core-skin structures.

1.3 Microcellular Injection Molding Technologies

Microcellular foams were first developed by Dr. Nam Suh at the MIT in the early 1980s [14]. However, Trexel Inc. first combined the concept of microcellular foaming and IM, patented, and commercialized the technology worldwide under the name MuCell® [24], [68]–[70]. Wittmann Battenfeld Inc. built physical foam IM machines 20 years before Trexel. Trexel's MuCell and Wittman Battenfeld's Cellmould technology use the same concept and agreed not sue each other's customers [71]. Only MuCell has gained acceptance among car manufacturers and is currently the leading MIM technology. In MuCell and Cellmould, SCF is directly injected into the polymer melt. Injection of the gas laden melt into the mold cavity induces cell nucleation followed by cell growth [17]. As outlined in previous chapters, upgrading traditional IM machines to offer MIM capabilities requires significant modifications to the plasticating unit as well as additional equipment (Figure 1.6). This leads to a high upfront capital investment and additional complexity in controlling the process [14], [15], [27], [28]. Other alternative process techniques have emerged next to MuCell as shown in Table 1.1.

Table 1.1. Overview of microcellular injection molding technologies.

Trademark	Technology	Pressure range [bar]	Reference
MuCell	SCF injection into melt	80-200	[68], [69]
Cellmould	SCF injection into melt	up to 330	[72], [73]
Optifoam	Special mandrel SCF injection nozzle plus static mixer	400	[74]–[77]
Ergocell	Dynamic mixer for SCF dosing plus plunger for injection	N/A	[14], [15], [75]
SmartFoam	Injection into runner during melt filling phase	N/A	[77]
ProFoam	Gas fed to pellets in special hopper unit	5-50	[78]–[80]
Ku-Fizz™	Gas fed to pellets in special hopper unit	5-30	[27], [28], [81]

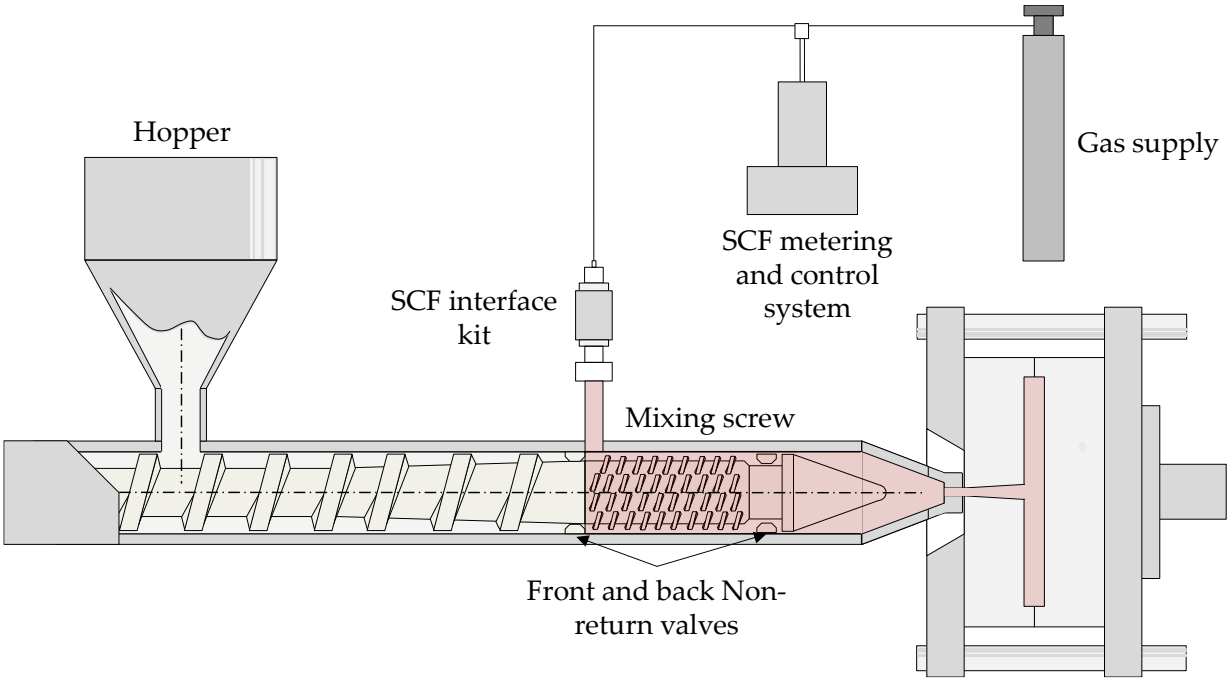

Figure 1.6. MuCell (cost $180k-300k) and Cellmould plant concept.

Optifoam and ProFoam were developed at the IKV - Institute for Plastics Processing, Ergocell was invented by Sumitomo-Demag, and Ku-Fizz™ was developed by Volkswagen AG. All these technologies use the same principle: Gas is dissolved into the polymer melt before melt injection into the cavity. The key difference between those technologies is how the SCF is dosed into the melt. Optifoam uses a special nozzle as the SCF dosing element where melt is loaded with gas during the injection phase. The nozzle sleeve has many ports to let gas go through as tiny droplets. The melt flow through the nozzle is divided into a thin film between the nozzle channel and the metal sleeve so gas diffusion times are shortened. The gas-laden melt is then mixed in a static blender channel that is located downstream of the nozzle dosing sleeve (Figure 1.7, left). The Ergocell system is an external assembly of an accumulator, a dynamic mixer, gas supply, and a hydraulic plunger that is mechanically integrated between the end of the barrel and the mold (Figure 1.7, right). As Ergocell costumers are required to buy Trexel MuCell licenses, a special assembly needs to be developed for each screw diameter, and only CO_2 can be used as PBA, this technology was not commercialized [14]. The SmartFoam process injects SCF directly into a mixing area within the runner system [77].

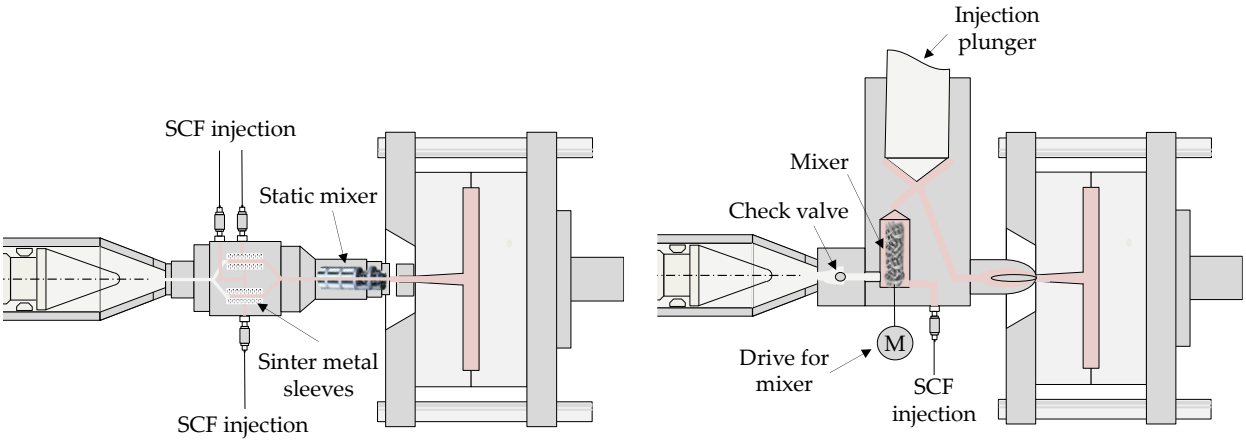

Figure 1.7. left: Optifoam concept. Modified from [74]. Right: Ergocell concept (cost $ 70k). Modified from [71], [82]

In ProFoam and Ku-Fizz™, gas at relatively low pressures is added to polymer pellets by employing special hopper unit. Gas and granules enter the barrel together and PBA diffuses into the polymer along the plasticating unit. Due to the prolonged exposure time between gas and polymer along the plasticizing unit, sufficient gas diffuses into the polymer and eliminates the need of additional mixing elements. The main difference between these two technologies are interior design variations in the hopper. The Ku-Fizz™ plant concept is shown in Figure 1.8. Suppliers for the hopper unit are Zimmermann Formenbau, FISAS Navaro and Stieler Kunststoff Service.

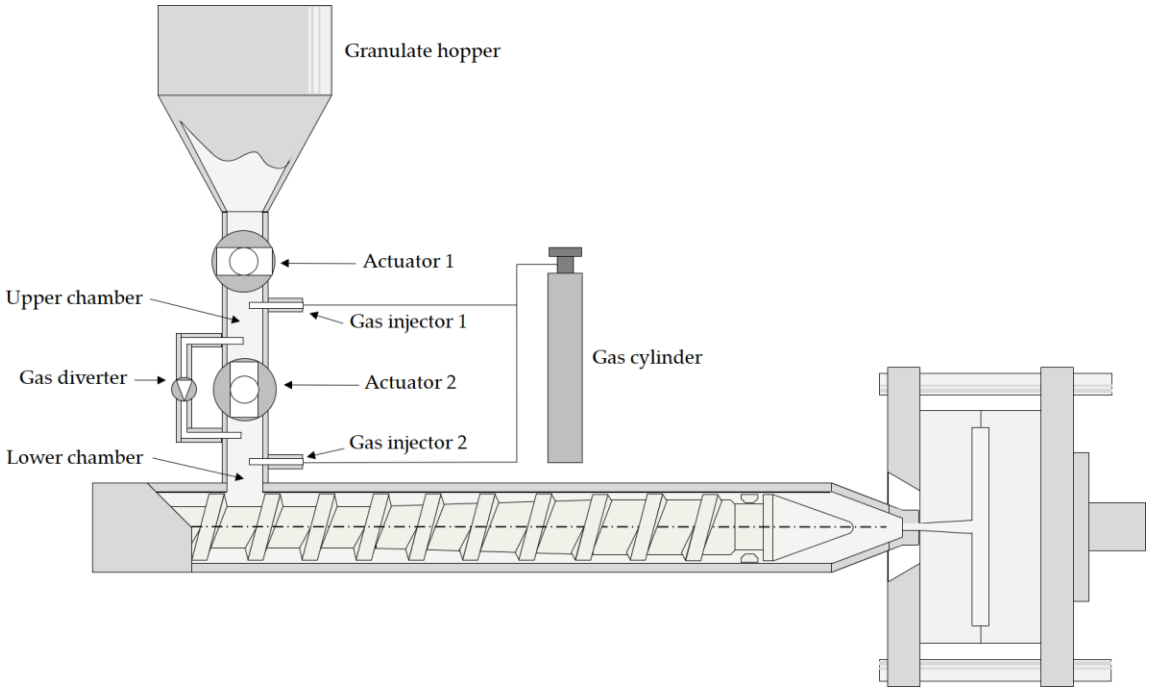

Figure 1.8. Ku-Fizz™ plant concept (costs $ 60-70k, without high pressure seals). Modified from [27].

Ku-Fizz™ is the MIM technology investigated in this work. The system is designed for PBA pressures up to 30 bar, to which the gas can be directly supplied from the cylinder. Gas is not raised to a SCF condition. The hopper unit contains two gas injectors, which introduce the PBA, valves, to regulate the gas flow and two actuators, to allow the material to pass through the unit and to lock each chamber (Figure 1.8). Initially, both actuators are closed, and the chamber is free from material and PBA. When actuator 1 opens, material from the hopper drops into the upper chamber. The chamber is locked, and the PBA is injected. Actuator 2 opens the airlock between both chambers and pellets fall into the lower chamber, which is connected to the injection unit. PBA fills the available space. A second gas injector adds PBA to the lower chamber to ensure a constant gas pressure. Pellets are transported away by a standard reciprocating screw and gas diffuses into pellets and melt. Actuator 1 opens, refills the upper chamber and the cycle is repeated. Ku-Fizz™ is controlled by gas pressure, thus, can be fully automated, and driven by an electronic system regardless the original software control of the IM machine [28].

Another foaming approach is to impregnate polymer pellets with PBA before feeding them into an IM machine. Lee et al., 2021, developed the supercritical fluid-laden pellet IM foaming technology (SIFT). The gas-laden pellets are produced by injecting PBA during extrusion. The extruded material is cooled down to prevent gas from foaming the polymer. The super-saturated pellets are then fed into a conventional IM machine to mold parts with a microcellular structure [83]–[86].

1.4 Modeling

For successful implementation of the MIM process for automotive applications, accurate numerical simulations must be available to predict the part's microstructure (MS) to then run FEA analysis and verify the molded product conforms with regulations. To describe foaming under polymer flow, a combination of nucleation models, diffusion-induced growth models and fluid models is required. Complex models on nucleation and cell growth have been developed. An overview of these mathematical models is given by [87]–[97].

Commercial simulation software for plastic IM such as Moldex3D®, Moldflow®, and CADMOULD® implemented nucleation and cell growth models to allow the prediction of MIM. In this work Moldex3D was used to predict the foam morphology of Ku-Fizz™ foamed parts. Moldex3D predicts CS and CD by considering nucleation and cell growth simultaneously. Interactions between cell formation and melt flow are considered by dynamic cell growth models. The user can select between four growth models: Han &

Yoo, modified Han & Yoo, Payvar, and Shafi. Han and Yoo is the default setting in Moldex3D and is commonly used in published work [27], [59], [98], [99]. Material properties such as gas diffusion coefficients, gas solubility parameter and surface tension, are based on experimental measurements and are available in Moldex3D for common gas-matrix systems.

In Moldex3D, the polymer/gas mixture is considered a General Newtonian compressible fluid. Thus, the non-isothermal 3D flow motion can be mathematically described by mass conservation, momentum conservation, and energy conservation as follows

$$\frac{\partial \rho}{\partial t} + \nabla \cdot (\rho \mathbf{u}) = 0 \tag{13}$$

$$\frac{\partial}{\partial t}(\rho \mathbf{u}) + \nabla \cdot \left(\rho \mathbf{u}\mathbf{u} - \eta(\nabla \mathbf{u} + \nabla \mathbf{u}^T)\right) = -\nabla p + \rho g \tag{14}$$

$$\rho C_p \left(\frac{\partial T}{\partial t} + \mathbf{u} \cdot \nabla T\right) = \nabla \cdot (\mathbf{k} \nabla T) + \eta \dot{\gamma}^2 \tag{15}$$

where ρ represents the polymer density, t the time, $\mathbf{u}$ the velocity vector, η the viscosity, p the pressure, g the gravity, C_p the specific heat, T the temperature, $\mathbf{k}$ the thermal conductivity tensor, and $\dot{\gamma}$ the shear rate [100], [101].

The dynamic behavior of cell growth can be written as

$$\frac{dR}{dt} = \frac{R}{4\eta}\left(P_D - P_c - \frac{2\gamma}{R}\right) \tag{16}$$

with R as the bubble radius, P_D as the gas pressure inside the cell, P_c as melt pressure at the outer boundary of the cell, and γ as the surface tension at the interface of melt and the gas [100]. The gas saturation pressure (P_{sat}^*) is $P_D(t=0)$ or P_{DO} . Thus, if the simulation input P_{sat}^* is set to 2 MPa, then $P_D(t=0) = 2\ MPa$. The larger P_D, the higher the nucleation speed $J(t)$, and the larger the CD. The initial cell size (R_0) is dependent on the gas saturation pressure P_{DO}, however the effect of P_D in the bubble growth equation is weak. Since the gas saturation concentration is fixed, the larger the bubble number density, the smaller the size of each bubble. A high $P_D(t=0)$ causes a small initial CS (R_0) and the bubble growth rate dR/dt is large. If $P_D(t=0)$ is small, R_0 is high and dR/dt is small. Therefore, the final bubble size R cannot be inferred qualitatively from equation 18. Since the cell nucleation equation dominates CD, it ultimately determines the bubble size due to a fixed gas saturation concentration.

P_D is determined by diffusion, while the pressure at the outer boundary of the cell, P_c, is determined by the molding process. Initially cell growth is driven by the pressure difference of internal gas pressure inside the cells and the surrounding polymer. At this stage growth speed depends on surface tension and

viscoelastic properties of the melt and is not controlled by diffusion. Diffusion-controlled growth starts when gas from the gas-laden melt is moved into the cell, and cell growth is shifted from a pressure dominated process to a diffusion dominated process [102]. The dissolved gas concentration profile along the radial direction of the polymer shell is given by

$$\frac{\partial c}{\partial t} = D\left[\frac{1}{r^2}\frac{\partial}{\partial r}\left(r^2\frac{\partial c}{\partial r}\right)\right] \tag{17}$$

where D is the diffusion coefficient of the gas in the polymer melt and c the dissolved gas concentration [53], [89], [100]. Figure 1.9 shows the cell growth model for an isolated cell in the polymer matrix.

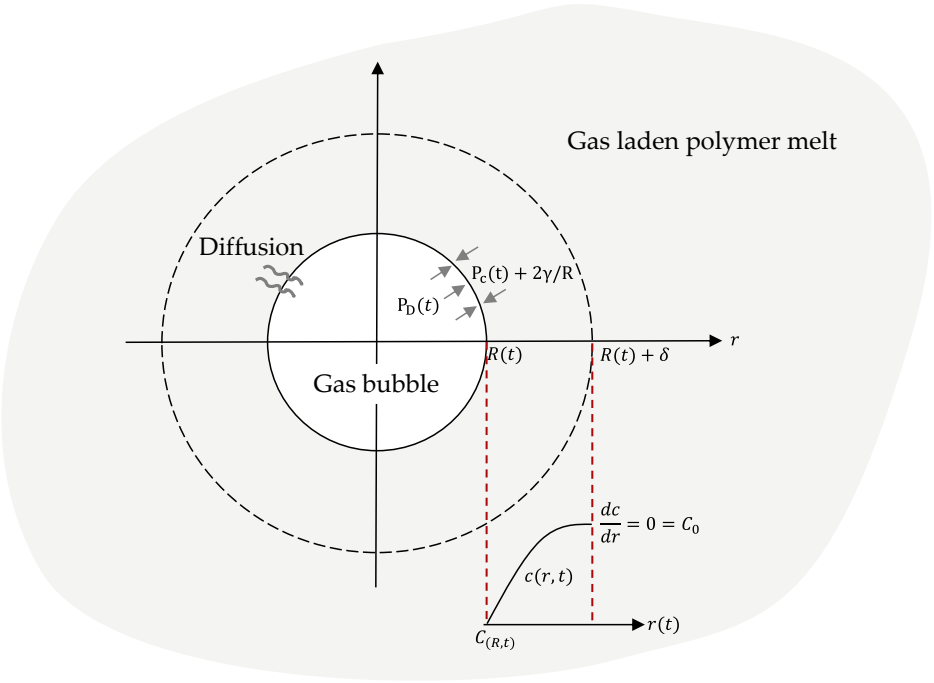

Figure 1.9: Cell growth of cell in polymer matrix, with $c(t)$ as time dependent gas concentration in the shell, $R(t)$ as the time dependent cell radius, and $R(t) + \delta$ as the time dependent radius of shell. Modified from [53].

During cell growth an increasing area is influenced, thus, mass transfer must be considered. Numerous mass transfer equations have been proposed to describe the gas mass transfer at the cell surface. Their equations and derivations can be found in [87], [88], [90]–[94]. A graphical comparison between three models is shown in Figure 1.10. Shafi's model shows the slowest change in cross-sectional area. The Han and Yoo model is faster, while Payvar's model is the fastest. Taki showed for a PP/CO_2 mixture that Han and Yoo's model best matched experimental data while for a PS/CO_2 mixture Payvar's model was closest to experimental results [89]. As published work on bubble growth model evaluations is sparse, the Han and Yoo model is currently the default model for foaming simulations.

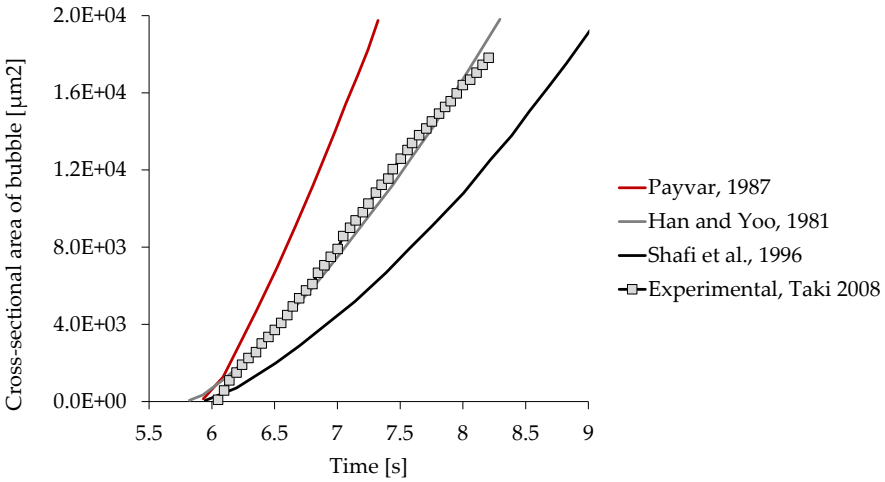

Figure 1.10: Comparison between experimental data and numerical simulations. Modified from [89].

Using Han & Yoo's model, the mass balance at the interface of the cell is written as

$$\frac{d}{dt}\left(P_D R^3\right) = \frac{6D\left(R_g T\right)\left(c_\infty - c_R\right)R}{-1+\left\{1+\frac{2/R^3}{R_g T}\left(\frac{P_D R^3 - P_{D0} R_0^3}{c_\infty - c_R}\right)\right\}^{1/2}} \tag{18}$$

where R_g represents the ideal gas constant, c_∞ the gas concentration for away from the cell, c_R the gas concentration on the bubble wall, P_{D0} the saturation pressure, and R_0 the initial bubble radius [100]. The gas concentration follows

$$\frac{c_\infty - c}{c_\infty - c_R} = \left(1 - \frac{r-R}{\delta}\right)^2 \tag{19}$$

where δ is the concentration boundary thickness [100].

Numerous cell nucleation rate $J(t)$ equations have been proposed [95], [103]–[106]. They all include a preexponential function followed by an exponential function. The most widely used cell nucleation rate equation which is also implemented in Moldex3D is

$$\mathrm{J_t} = f_0 \left(\frac{2\gamma}{\pi \mathrm{M_w}/N_A}\right)^{1/2} \exp\left(-\frac{16\pi\gamma^3 \mathrm{F}}{3\mathrm{KT}\left(\frac{\bar{c}(t)}{k_H} - P_c(t)^2\right)}\right) \mathrm{N_A}\bar{c}(t) \tag{20}$$

$$\bar{c}(t)V_{L0} = c_0 V_{L0} - \int_0^t \frac{4\pi}{3} R^3(t-t',t') \frac{P_D(t-t',t')}{R_g T} J(t') V_{L0} dt' \tag{21}$$

where f_0 and F represent fitting parameter (FP), $\mathrm{M_w}$ the gas molecular weight, N_A the Avogadro number, K as Boltzmann constant, $\bar{c}(t)$ the average dissolved gas concentration in the polymer at time t, k_H as

solubility parameter, $P_c(t)$ is the melt pressure, V_{L0} the volume of polymer matrix, and P_D the bubble pressure [100].

For a valid quantitative comparison of simulation and experimental data, an accurate set of FP (f_0, F) needs to be employed. The physical meaning of f_0 can be interpreted as the correction factor of the Zeldovich factor which gives the probability that a nucleus will go on to form a new phase, rather than dissolve [89]. f_0 is directly proportional to the nucleation rate, thus an increase in f_0 will result in an increase in the nucleation rate. F is the correction factor of the free energy barrier of the cell nucleation rate. In the presence of additives and fillers the energy barrier is reduced [89]. A decreased F will increase the nucleation rate.

Most published work uses Moldex3D's default FP [27], [59], [99]. However, these parameters are only valid for specific gas-matrix systems which show homogenous nucleation. Taki and Xi et al., determined f_0 and F by fitting experimental data to numerical results [89], [98]. Taki used the change in the number density of bubbles obtained by visual observation experiments of batch physical foaming. The author changed the values of f_0 and F by trial-and-error until a good fit was achieved [89]. Xi et al., obtained the FP by nonlinear regression of experimental CS and CD [98]. Xi et al., then used the found FP to predict the CS and CD of iPP/nan-$CaCO_3$ composites using Moldex3D. A good fit was found for different processing conditions with average relative deviations less than 15 % [98].

It needs to be noted that all simulation efforts have been focused on relatively simple parts (Table 1.2). Additionally, no attempts have been made to predict the foam MS for alternative MIM processes, such as Ergocell, Optifoam, ProFoam and Ku-Fizz™.

Table 1.2. Parts used for Moldex3D predictions.

Part Geometry	Reference
ASTM-D638 tensile bar	[98]
Square plate	[107]
Cylindrical bars	[108]
ASTM Type I tensile test bar	[109]
Hemispherical shell	[110]
Sleeve with flange	[111]
Box	[112]

1.5 Motivation and Objectives

The Ku-Fizz™ MIM technology has the potential to be a cost-effective competitor to leading the foaming technology MuCell. However, for its progress a better understanding of the process and development of simulation models are required.

To achieve this objective, the following steps will be taken:

i. The process's gas pressure operating window and its effect on the foam MS will be studied to verify if the cell properties obtained with Ku-Fizz™ are at par with those obtained with MuCell. MS as a function of N_2 pressure will be determined from simple plate geometries to directly relate MS CD and CS with processing conditions.

ii. An automotive component foamed with Ku-Fizz™ will be studied. First, the foam and fiber MS will be characterized. Second, the mechanical response of the component for different loading conditions will be investigated. Finally, a correlation between the mechanical response and the microstructure will be drawn.

iii. Foaming models implemented in Moldex3D will be evaluated and updated to describe the behavior observed in Ku-Fizz™ foamed plates, boxes, and inner door panels. To achieve this, first, gas dynamics in Ku-Fizz™ will be calculated, second, the current MuCell foaming tool in Moldex3D will be evaluated for the use of Ku-Fizz™. Third, screw pull out experiments will be conducted to understand the gas mixing behavior during plastication and propose a pressure correction factor for Moldex3D models. Finally, the new proposed foaming model will be validated with a complex automotive door panel.

2 Effect of gas pressure on the microstructure of Ku-Fizz™ foamed parts

2.1 Introduction

The technology and the pressure operating window for MuCell and Ku-Fizz™ are quite different. MuCell injects SCF into the plasticating unit at 80-200 bar gas pressures, while Ku-Fizz™ introduces gas at 5-30 bar into the plasticating unit. Thus, Ku-Fizz™ needs to be studied to evaluate if an acceptable foam MS can be achieved at such low gas pressures. In this work, fiber-reinforced PP was foamed under various gas pressures and the effect on the MS was analyzed. The presence of fibers causes a refined foam MS due to heterogenous cell nucleation, but also adds complexity since the foamed composite's performance will additionally depend on fiber orientation (FO), fiber length (FL), and fiber concentration (FC) [113]. To determine the performance based on the MS, a multiphase foamed composite was tested in COMSOL Multiphysics.

2.2 Experimental

2.2.1 Materials and Processing Conditions

The material used was a 30 wt% glass fiber in a PP matrix (STAMAX PPGF30 YM 243) commercially available from SABIC™. The material was supplied in the form of coated pellets with a nominal length of 15 mm, which also represents the initial and uniform length of glass fibers. The used E-glass fibers (ϱ = 2.55 g/cm^3) are chemically coupled to the PP matrix (ϱ = 0.91 g/cm^3). The fiber diameter was measured to be 19 ± 1 μm using an optical microscope.

To remove any moisture in the material, it was dried at 80 °C for at least four hours before processing. Parts were molded on a Krauss Maffei 200-1000/390/CZ Multinject IM machine (KraussMaffei Group GmbH, Germany) equipped with a Ku-Fizz™ unit. The IM machine had a clamping force of 2000 kN and a screw diameter of 55 mm. A simple plate geometry was chosen in this work to allow for a direct correlation between processing conditions and microstructure. The rectangular plates had dimensions of 400 x 100 mm and a thickness of 3.5 mm, as shown in Figure 2.1. Plates were foamed at various gas pressures while the other processing conditions were kept constant (Table 2.1). N_2 was used as the PBA for all trials. A PSA MIDIGAS nitrogen generator (Parker-Hannifin Corporation) was employed to recover high-purity

nitrogen from air. The gas had a purity of 99.9 % with an oxygen amount of < 500 ppm in continuous operation.

Table 2.1. Processing conditions for compact and microcellular injection molding trials.

Molding parameter	Compact	Foamed
Gas pressure [bar]	0	7.5, 10, 15, 20, 25
Melt temperature [°C]	230	230
Mold temperature [°C]	50	50
Screw speed [mm/s]	200	200
Shot volume [cm³]	230	190
Injection pressure [bar]	1500	1500
Injection speed [cm³/s]	150	150
Filling time [s]	1.4	1.4
Packing pressure [bar]	250	used gas pressure
Packing time [s]	10	10
Cooling time [s]	35	23

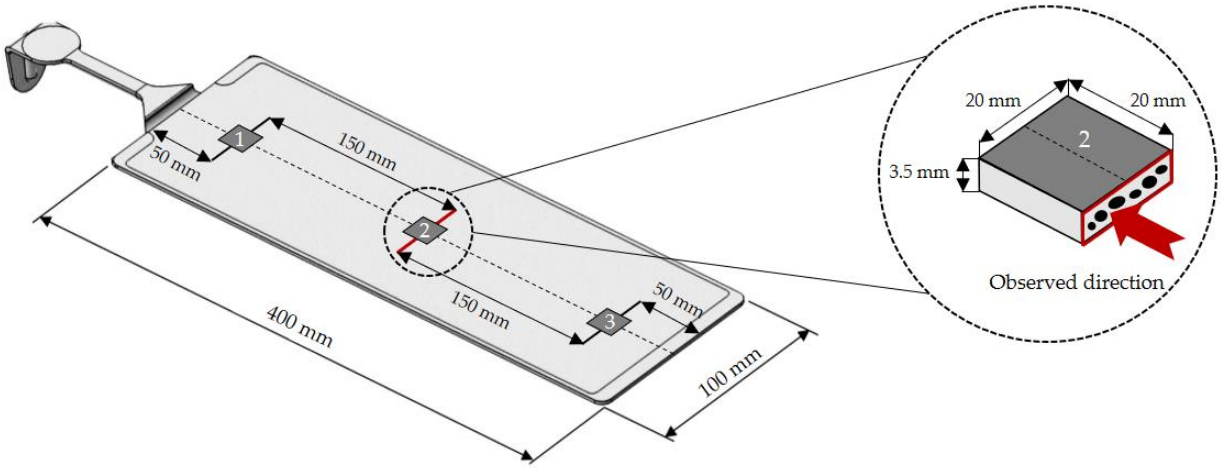

Figure 2.1. Plate geometry with sample locations for foam and fiber microstructure analysis.

2.2.2 Measurement of Foam Microstructure

The microcellular structure was studied transversal to the melt flow direction at three locations along the center line of the part: close to the gate (R1), in the center of the plate (R2), and at the end of the flow path (R3) (Figure 2.1). Samples were extracted, cold mounted in acrylic resin, and their cross-sections were grinded and polished with a Metprep 3™ Grinder/Polisher system (Allied High Tech Products Inc). Multiple overlapping micrographs were taken (Motic BA310Met microscope equipped with a digital AmScope MA1000 camera) and stitched together to cover the entire cross-sectional area of each specimen. A magnification factor of 5 ensured that bubbles as small as 3 μm could be captured. Monterde, did

preliminary work on Ku-Fizz™ foamed plates, and by using SEM analysis, it was shown that only 1.5 % of all cells are smaller than 5 μm [28]. Thus, the employed analysis method was found as sufficiently precise. Micrographs were adjusted for an appropriate level of contrast (thresholded) and the foam microstructure was analyzed with the 2D Image Pro analysis software (Media Cybernetics Inc., Rockville, MD). Thickness-wise CS, CD, aspect ratio data were obtained by assigning 15 regions of interests (ROIs) across the plate's thickness and conducting an analysis in each ROI. CD was estimated by

$$Cell\ density = \left(\frac{n}{A}\right)^{\frac{3}{2}} \tag{22}$$

where n is the number of cells in the micrograph or in the respective ROI for thickness-wise data, and A the area of the micrograph or the ROI in cm², respectively [114]. The mean CS was calculated from optical micrographs as follows

$$Cell\ size = \frac{\sum_{i=1}^{n} d_i}{n} \tag{23}$$

where d_i is the average diameter of the cell, n the number of cells in the micrograph or in the respective ROI [115]. For thickness-wise information, large cells protruding multiple ROIs were attributed to the corresponding ROI where the cell's majority was located. Interconnected or clustered cells were counted individually if a boundary was evident. If no boundary could be detected and it was not possible to identify single cells constituting to a larger, deformed cell, the cluster was counted as one bubble. Due to the high occurrence of irregularly shaped cells, the aspect ratio was determined as the ratio between major axis and minor axis of an ellipse equivalent to the region of the cell. At least five plates per testing condition were analyzed to ensure accuracy and repeatability of results.

2.2.3 Measurement of Fiber Microstructure

FO and FC were determined by using the X-ray microcomputed tomography (μCT) approach. Discs of dimensions 21 mm² x 3.5 mm were scanned with an industrial μCT system (Metrotom 800, Carl Zeiss AG, Oberkochen, Germany). Previous studies with the same material have shown that a voxel size of 5 μm adequately captures the glass fiber geometry [116], [117]. Table 2.2 summarizes the acquisition parameters for the μCT scans in this work.

The μCT data set was processed with VG StudioMAX (Version 2.2, Volume Graphics GmbH, Heidelberg, Germany) to obtain the through thickness values of fiber volume fraction [116] and second-order orientation tensor components [116], [118], [119].

The FL measurement technique presented in [120] was employed in this work. This technique consists of fiber dispersion and a fully automated image processing algorithm to quantify the fiber length distribution (FLD). The Kunc-correction was applied to all results, as down-sampling methods preferentially capture longer fibers and thus skew the real FLD [121].

Table 2.2. X-ray microcomputed tomography settings.

Parameter	Value
Voltage [V]	80
Current [A]	110
Integration time [ms]	1000
Gain [-]	8
Number of projections [-]	2200
Voxel size [μm]	4.5

2.3 Results and Discussion

2.3.1 Effect on Foam Microstructure

The molded plate weight as a function of gas pressure is shown in Figure 2.2. A 16% plate weight reduction is seen with an applied maximum gas pressure of 25 bar. The plate weight decreased almost linearly with increasing gas pressure starting at 10 bar. For 7.5 bar and 10 bar, a similar weight reduction of 5% was noticed. Obeloer [80] who worked with ProFoam, recorded a maximum weight reduction of 12.4% and 13.9% for plates foamed at 5 bar and 10 bar, respectively. A weight reduction of 1% was observed when the gas pressure was increased from 7.5 bar to 10 bar, while with Ku-Fizz™ only a 0.1% weight reduction was noted. Obeloer noticed the linear increase in weight reduction stopping at 35 bar as the curve started to level off [80]. This behavior could not be seen in Figure 2.2. Starting at 30 bar the ball sector valves employed in the Ku-Fizz™ hopper unit reach their working limit and cannot close properly. Gas escapes through the hopper, leading to a weight reduction and foam microstructure resembling the one seen at 25 bar. While custom-made ball sector valves are available up to 50 bar gas pressure, they are expensive and defeat the cost-effectiveness of Ku-Fizz™, thus will not be used in production.

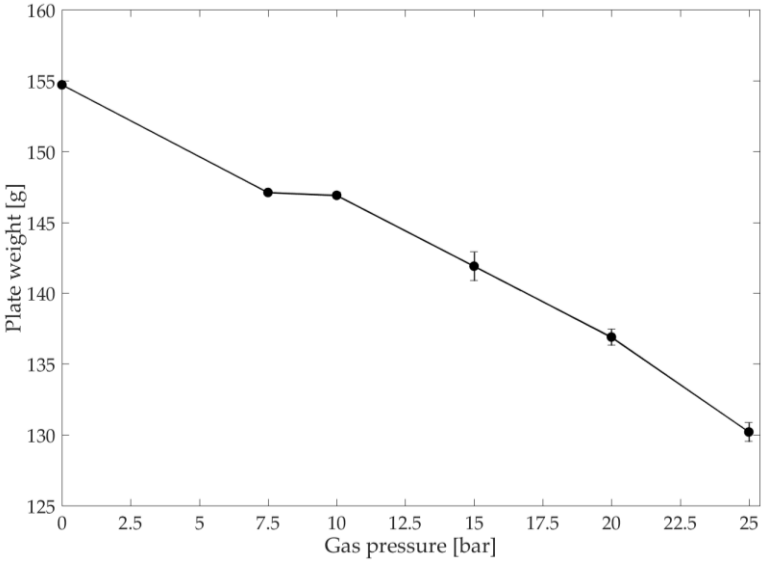

Figure 2.2. Plate weight as a function of gas pressure.

The cell morphology under different gas pressures is shown in Figure 2.3. Dark areas indicate cells, grey areas represent the polymer, and fibers are shown in white. As the gas amount increases, CD increases and thus CS decreases. An increased gas pressure leads to a higher gas concentration in the melt and causes a higher cell nucleation rate [14], [98], [122]. This finding aligns with literature as shown in Table 2.3. At low gas pressures (7.5 bar and 10 bar), the nucleation rate is low. Due to the small number of formed cells, the diffusion paths of PBA are considerably longer. Thus, only a small available percentage of PBA can contribute to cell growth [80]. Cells that have nucleated however, have a high growth rate leading to large bubbles which can have a maximum diameter of up to one fifth of the plate thickness. Such large, coalesced cells can cause the mechanical properties of a part to deteriorate rapidly. Figure 2.3 further illustrates, that a well-defined cell structure was achieved for the 25 bar setting. Consequently, indicating that the PBA content employed in Ku-Fizz™ is sufficient to manufacture a microcellular composite.

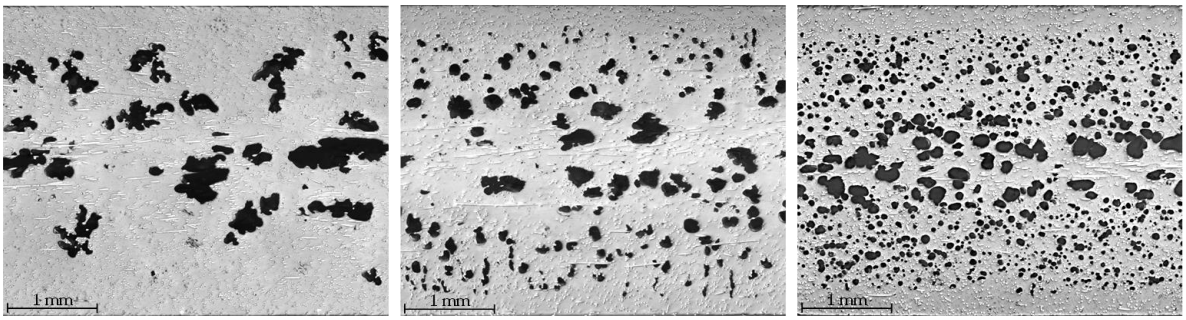

Figure 2.3. Microscopic images in R2 of cross-sections of microcellular injection molded samples.

Table 2.3. Published work determining the influence of PBA on foam MS. SGF indicates short glass fiber, LGF represents long glass fiber reinforced materials. + positive effect, - negative effect, and 0 no effect was observed.

Material	CD	CS	Technology	Reference	Year
30 wt% SGF PA66	+	-	MuCell	[63]	2020
Nano&micro filled PBS	+	-	MuCell	[123]	2020
20 wt% SGF PP	+	-	MuCell	[122]	2019
15-30 wt% GF PP	+	-	ProFoam	[80]	2012
PP & LDPE	+	-	MuCell	[124]	2011
HDPE & PVC	+	-	MuCell	[14]	2010

While at low gas pressures (7.5 bar and 10 bar) the cell structure is mostly uniform across the sample thickness, a pronounced core-shell structure develops with increasing gas pressure, which is inherent to the IM process and thick MIM parts [14]. This structure shows a solid skin layer, a center core layer, and a transition layer (shell) between skin and core. During processing the temperature distribution along the thickness direction of the plate has a bell-shape, in which the temperature in the core layer is higher than at the shells. The cells, therefore, grow more in the core due to the low matrix viscosity. Near the mold surface, cells are smaller due to the faster matrix solidification [14], [122], [125], [126]. Zhang et al. indicated that an increasing stress in the polymer melt promotes bubble nucleation [125]. Since the shear stress is higher in the shell layers, an increased CD can be found in those regions. All samples showed a distinct skin layer which reduces in thickness with increasing gas pressure and flow path. Compact skin layers are a result of the following: rapid solidification of the melt after contacting the mold surface, redissolution of PBA within cells into the polymer melt and a restraint of foaming by high cavity pressure [127].

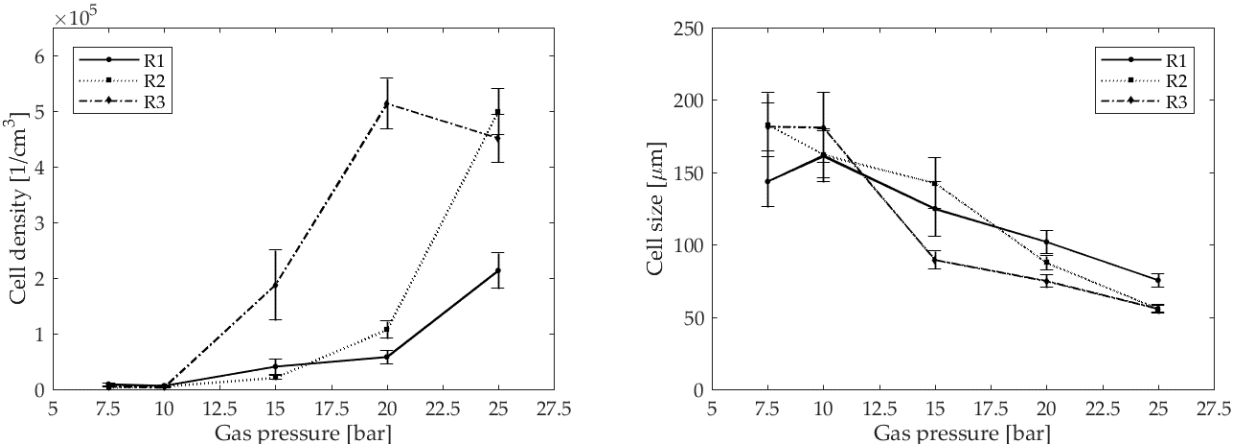

Figure 2.4. Effect of gas pressure on global CD and CS, analyzed close to gate (R1), center of the part (R2), and end of flow path (R3).

Global CD and CS data as a function of gas pressure are shown in Figure 2.4. As visible in Figure 2.3, CD increases while the CS decreases with increasing gas pressure. This trend corresponds with work published by [14], [63], [78], [122], [124], [128]–[130] investigating the effect of gas pressure on foamed parts. At higher gas pressures the nucleation energy barrier is lower, and the nucleation supersaturation degree can be achieved faster. Therefore, cells nucleate earlier and more often, leading to a higher nucleation rate and CD. As cell nucleation and growth are two competitive factors, a fast nucleation rate equals a low cell growth rate. Thus, smaller cells are formed [128]. Cells have an average size of 170 µm and a CD of $6*10^3$ cells/cm^3 at low gas pressures. At 25 bar, an average CS of 55 µm and a CD up to $5*10^5$ cells/cm^3 were recorded. A maximum CD of $5.1*10^5$ cells/cm^3 was reported at the end of flow path for the 20 bar setting. Typical MuCell foamed parts show a CS of 100 µm or less and a CD of around 10^6 cells/cm^3 [124], [128].

Zhang et al. showed that temperature decreases slightly along the part's flow path [125]. A lower temperature represents an increased viscosity, thus a higher growth resistance. Bubbles in R3 are generally smaller than in R2 and R1. Close to the gate (R1), the material cools down slower, causing cell growth [122]. CD generally increases along the flow path with R3, showing the highest CD (R1<R2<R3). Our results do not align with the data published by Zhang et al. and Lee et al., as an increasing CS and a decreasing CD from the center of the plate towards the end of flow path were observed in these studies [125], [130]. Both found the pressure state decreasing along the part and showed a bigger pressure drop closer to the gate, which promotes cell nucleation. On the contrary, Ahmadzai et al. foamed a simple plate geometry with polystyrene and found that CD increased towards the end of the cavity [131]. As by [125], [130] the seen trend was explained with the dropping system pressure towards the end of the cavity. However, Ahmadzai et al. argued that a high system pressure tends to suppress cell growth and may even cause cells to collapse. Hence, the number of nucleated cells is smaller near to the gate and larger towards the end of the cavity [131], [132]. Other researchers also recorded the average cell diameter decreasing with distance from the gate and thus an increasing CD [14], [63], [133], [134]. Monterde, performed preliminary work with Ku-Fizz™ by comparing its foam microstructure to parts manufactured with MuCell. The results from Ku-Fizz™ evidenced CD was the highest in R1, followed by R3 and R2. The largest cells were located at the end of the cavity. Pressure state, diffusivity and concentration of the gas, temperature and shear stress distribution are all interdependent factors that affect the final foam microstructure.

Through-thickness CD and CS data as a function of gas pressure and location are shown in Figure 2.5. The boundary between different regions becomes more defined with increasing gas pressure, as CD and CS transition from a mostly uniform distribution across the sample thickness to a pronounced core-shell

structure. An increased standard deviation can be noticed for plates foamed at low gas pressures, since cell shape and size were very large and irregular. In some cases, individual cells covered 20% of the plate's thickness. Close to the gate (R1), flow entry effects are present, creating a more homogenous core-shell structure, compared to R2 and R3 where the structure is more pronounced.

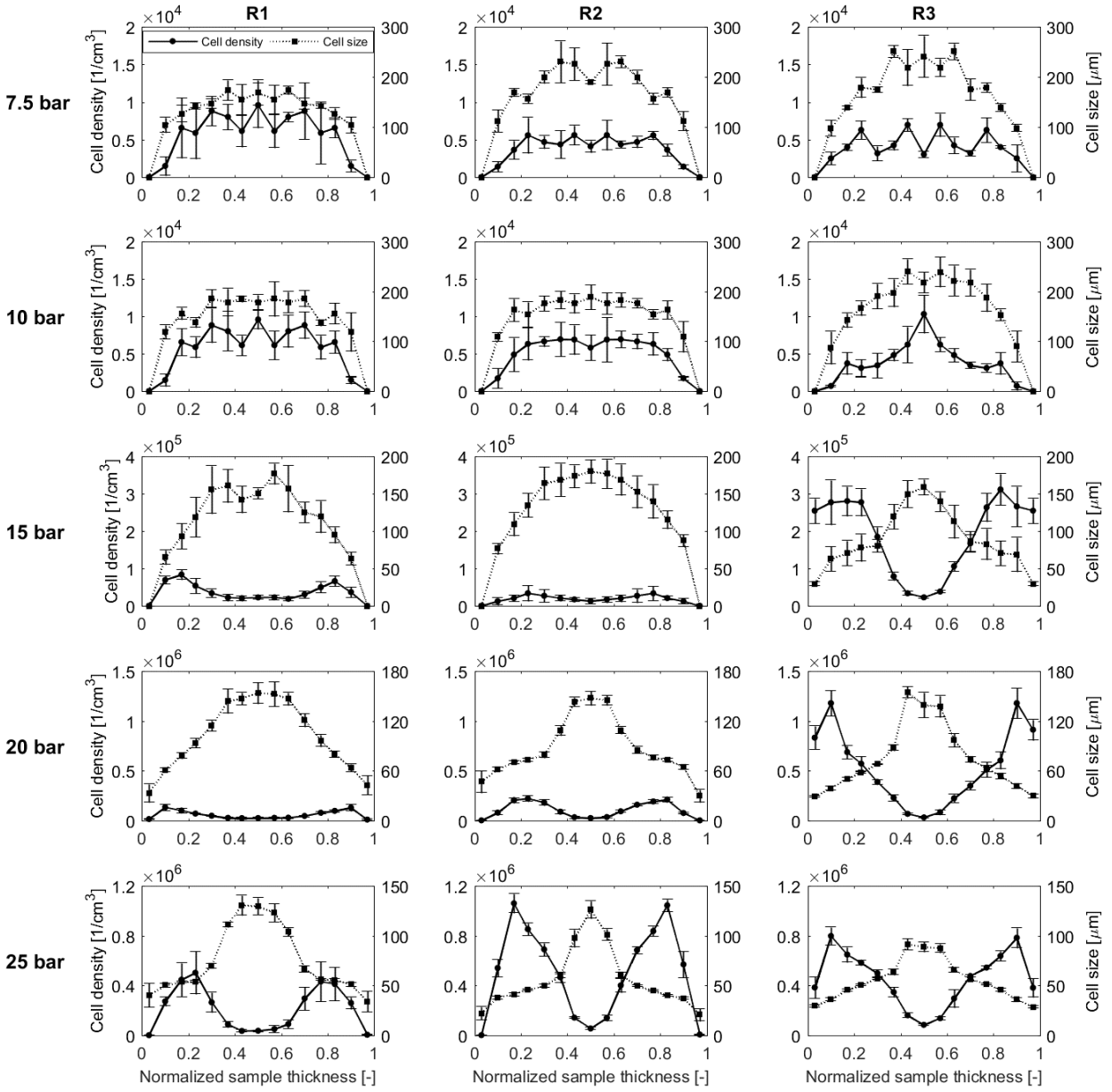

Figure 2.5. CD and CS through sample thickness at varying gas pressures and plate locations (R1-R3).

Global and thickness wise aspect ratio are shown in Figure 2.6 and Figure 2.7. With increasing gas pressure, cells transform from highly irregular shapes to more spherical ones. To keep cells uniform, spherical and

small is desired to truly take advantage of the MIM technology. However, non-uniform CS distributions are common for MIM PP parts [14]. Generally, cells become more spherical along the flow path, as they reduce in size. This trend does not align with data published by Wang et al., as for regions far away from the gate cells became severely deformed [133]. In this work, the foam microstructure was only analyzed transversal to the melt flow direction as cells are preferentially aligned in melt flow direction. Consequently, possible deformations visible in parallel to the melt flow could not be captured.

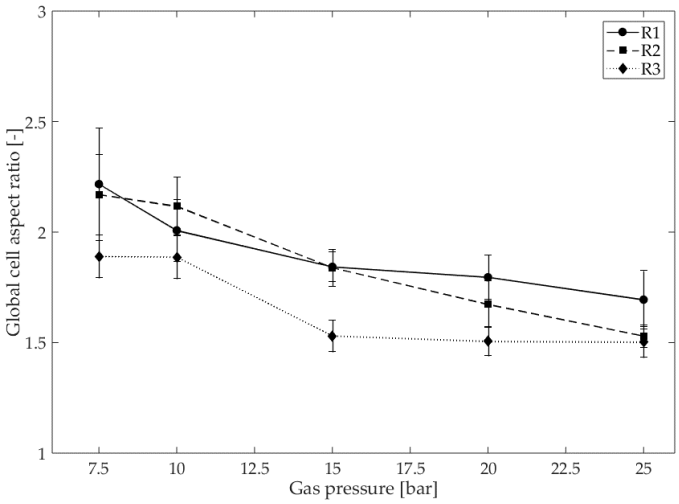

Figure 2.6. Global cell aspect ratio as a function of gas pressure and plate location.

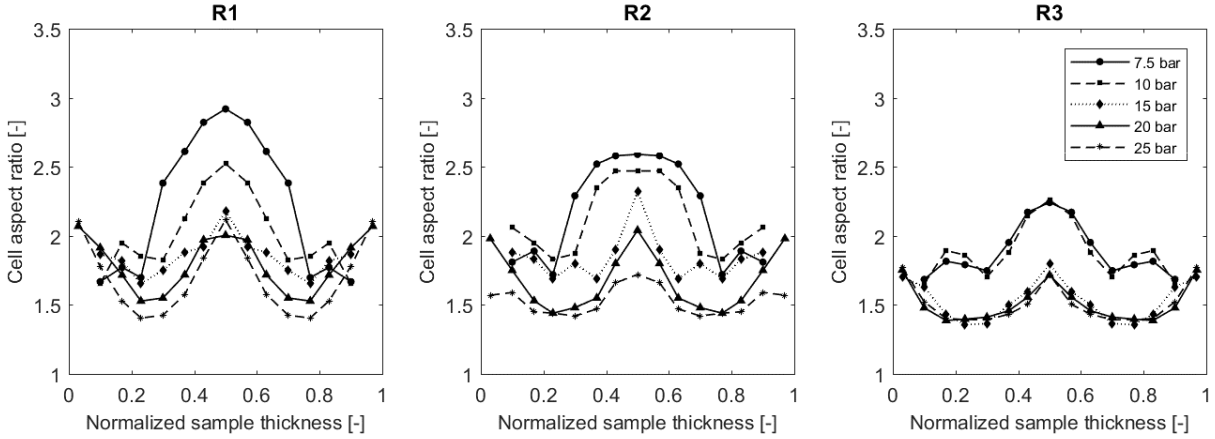

Figure 2.7. Bubble aspect ratio through sample thickness at varying gas pressures. Data does not include error bars to ease in trend visualization. Standard deviation is on average 0.2 [-].

During the mold filling stage, the melt flow is a laminar shear flow that exhibits the fountain flow effect at the flow front [133], [135]. This effect forces the melt at the flow front towards the cavity surface. Since bubbles do not have inertia, they follow the streamlines of the polymer. The melt flow velocity is smaller at the cavity wall than in the center layer of the mold cavity. This results in a large shear rate gradient. In

such flow field, cells will be deformed by the shear stress. Close to the cavity wall, the shear stress is high, and cells will be deformed to an ellipsoidal shape with a large axis ratio [133]. This explains the observed increased aspect ratio close the mold walls, as shown in Figure 2.7. Deformation increases as the melt moves forward, additionally stretching the bubbles. For parts with a large flow length to wall thickness ratio, cells can transform to long and thin strips which eventually break up into a series of smaller bubbles or cause the evolved gas in bubbles to redissolve into the polymer melt [133]. Wang et al. reported that in the center layer, cells have a nearly ideal spherical shape due to a zero-shear rate [133]. In this study, cells had the highest aspect ratio in the center layer, which can be attributed to the temperature gradient that is at a maximum in the center region. Increased temperature allows prolonged cell growth. Some cells are so close and big, that they can overlap and then either experience wall rupture, merge into larger even more deformed bubbles, or they stay clustered together [14], [122]. Deformed cells tend to orientate slightly along the melt flow direction. The degree of orientation of the bubbles depends upon shear rate, melt viscosity, surface tension and bubble size [133], [135].

2.3.2 Effect on Fiber Microstructure

The presence of glass fibers promotes nucleation and refines the cell structure. Fibers act as heterogenous nucleation sites during foaming. They provide crevices to trap gas and form nuclei [63], [136]. As shown in Figure 2.8, FL significantly increases with gas pressure. Shear viscosity and pseudoplasticity of the matrix play a dominant role in fiber attrition. Dissolved gas acts as a plasticizer and reduces the melt viscosity and thus the occurrence of fiber breakage during processing [12], [137]. In the center of the plate, L_W for compact samples is 1.23 mm and was increased to 1.64 mm at 25 bar gas pressure. Zhang et al. also reported less fiber breakage with increasing PBA. The authors found that the introduction of PBA increased the non-Newtonian behavior and blunted the shape of the velocity profile. This reduced the quantity of fibers experiencing shear flow and lowered fiber rotation and thus the occurrence of fiber breakage [12]. It can be further seen in Figure 2.8 that FL increases with melt flow direction. This trend was also observed by Goris and Phelps et al., where IM LFT samples showed an increased FL at the end of flow path [116], [137]. Goris explained this phenomenon with a higher nominal FC present in the region, suggesting that the last filled portion of the part carries longer fibers [116]. Phelps et al. attributed it to the fountain flow effect [137]

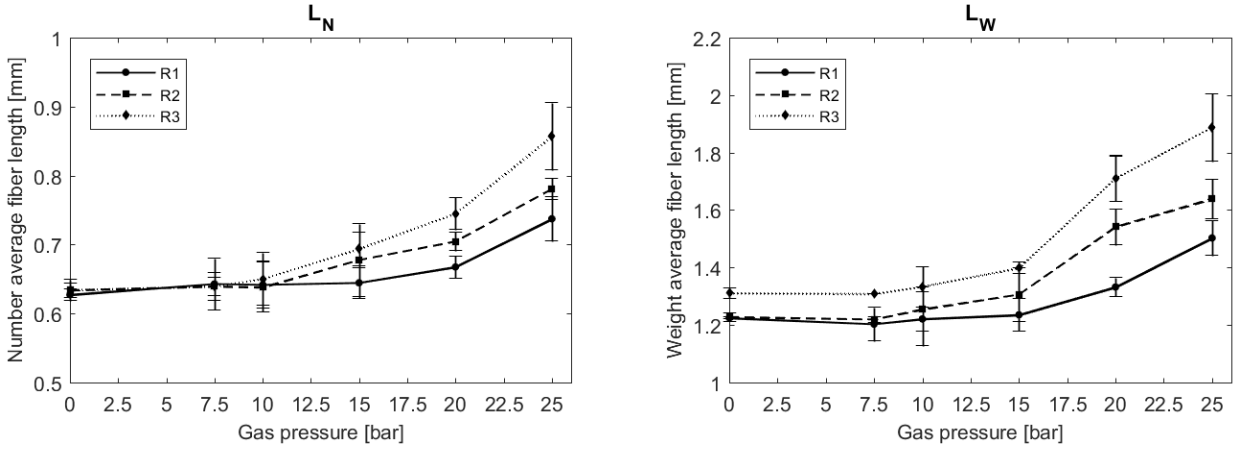

Figure 2.8. FL as a function of gas pressure and sample location, close to gate (R1), center (R2), and end of flow path (R3). Initial fiber length before processing is 15 mm.

FO is a crucial microstructural parameter that affects the mechanical properties, shrinkage, and the dimensional stability of molded parts [138]. As seen in compact IM, fibers arranged in a multi-layer orientation pattern, commonly referred to as core-shell structure (Figure 2.9). The core layer consists of fibers predominantly aligned in crossflow direction (a_{22}), while fibers in the shell are oriented along the flow direction (a_{11}) due to the fountain flow effect and the no-slip condition on the mold [116], [139]. The orientation in thickness direction (a_{33}) is mostly uniform with average values of 0.06.

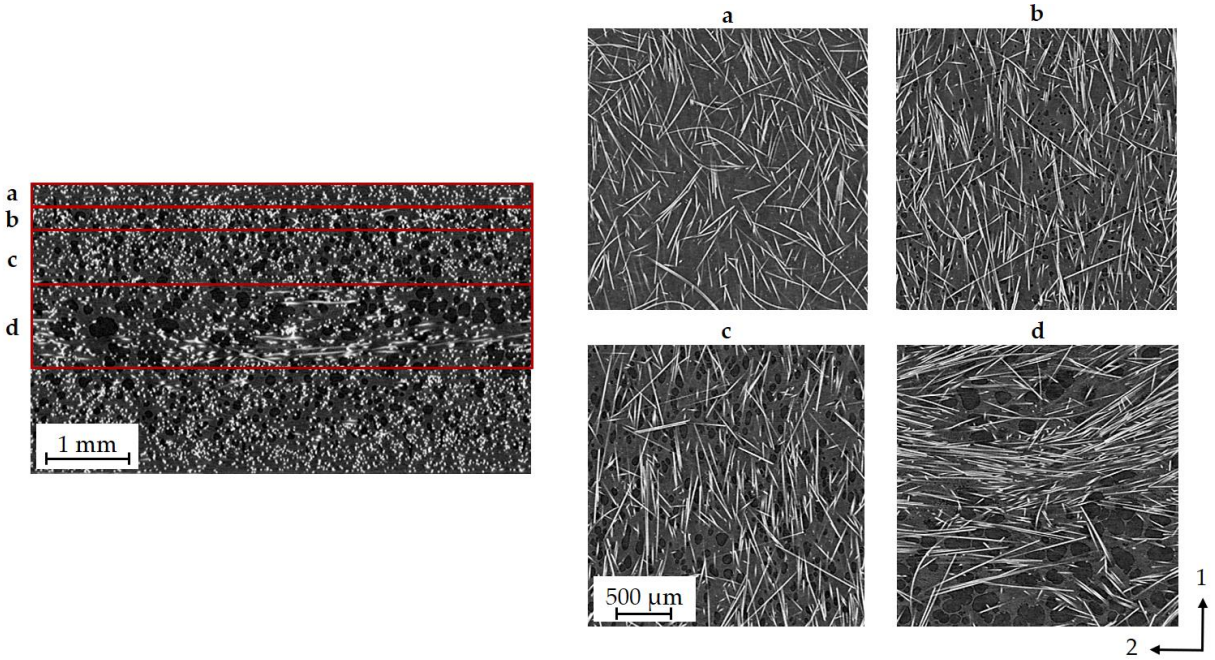

Figure 2.9. Typical core-shell microstructure of MIM molded parts. 1 indicates melt flow direction and 2 the crossflow direction. (a) skin layer with no cells and fibers mostly oriented in flow direction, (b) shell layer with small cells and the majority of fibers still being oriented in flow direction, (c) shell layer closer to center region with increased cell size, and (d) core layer with large cells and fibers oriented in cross-flow direction.

The global diagonal components of the orientation tensor are shown in Figure 2.10. It can be observed that with increasing gas pressure, fibers become oriented in flow direction. This trend is explained by analyzing Figure 2.12. As the PBA content rises, the core region becomes thinner, and thus the shell region becomes thicker. In the shell, fibers are predominantly oriented in flow direction, therefore attributing to an increased global value of a_{11}. As the core becomes thinner, less fibers are oriented in crossflow direction, causing a_{22} to decrease. μCT data (Figure 2.11) also showed core thinning and underlined the trend seen in Figure 2.10 and Figure 2.12. Green/blue regions demonstrate fibers that are aligned in flow direction (a_{11}), whereas red/orange regions represent a crossflow orientation state (a_{22}). The green/blue shell layers become wider with PBA content. Along the melt flow direction, samples close to the gate showed a wider core layer than those at R2 and R3 (Figure 2.12). A broader core layer gives rise to an increased a_{22}. This is caused by the radial flow near the gate. In R2 and R3, the flow is fully developed, and its flow characteristics do not change anymore. Therefore, a constant FO was reached, and a defined core-shell structure is visible.

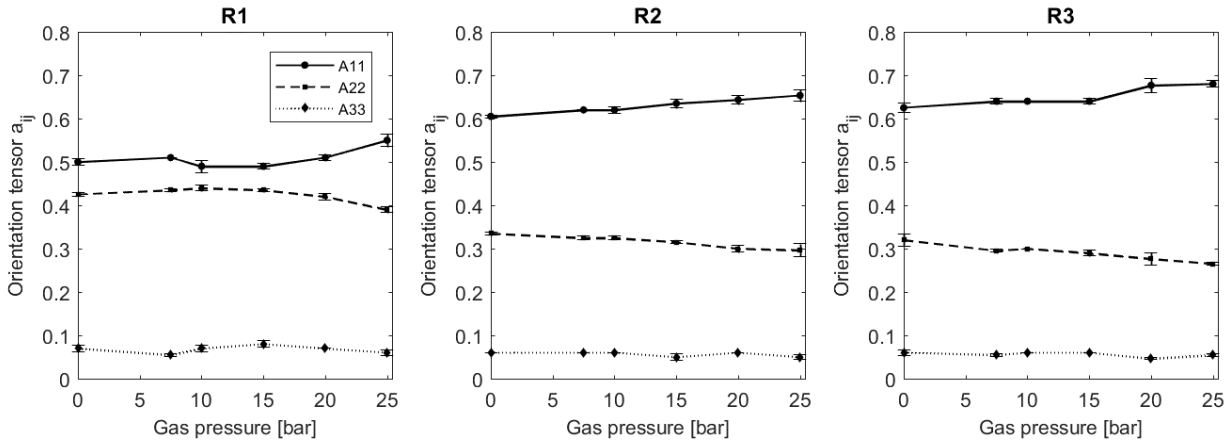

Figure 2.10. Global FO as a function of gas pressure and location. Close to gate (R1), center (R2), and end of flow path (R3).

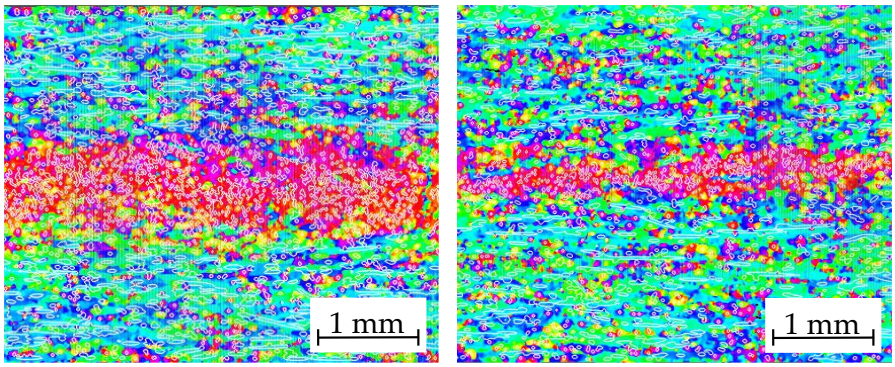

Figure 2.11. FO through thickness at sampling region R2 (center) from VG StudioMax analysis, left: 7.5 bar, right: 25 bar.

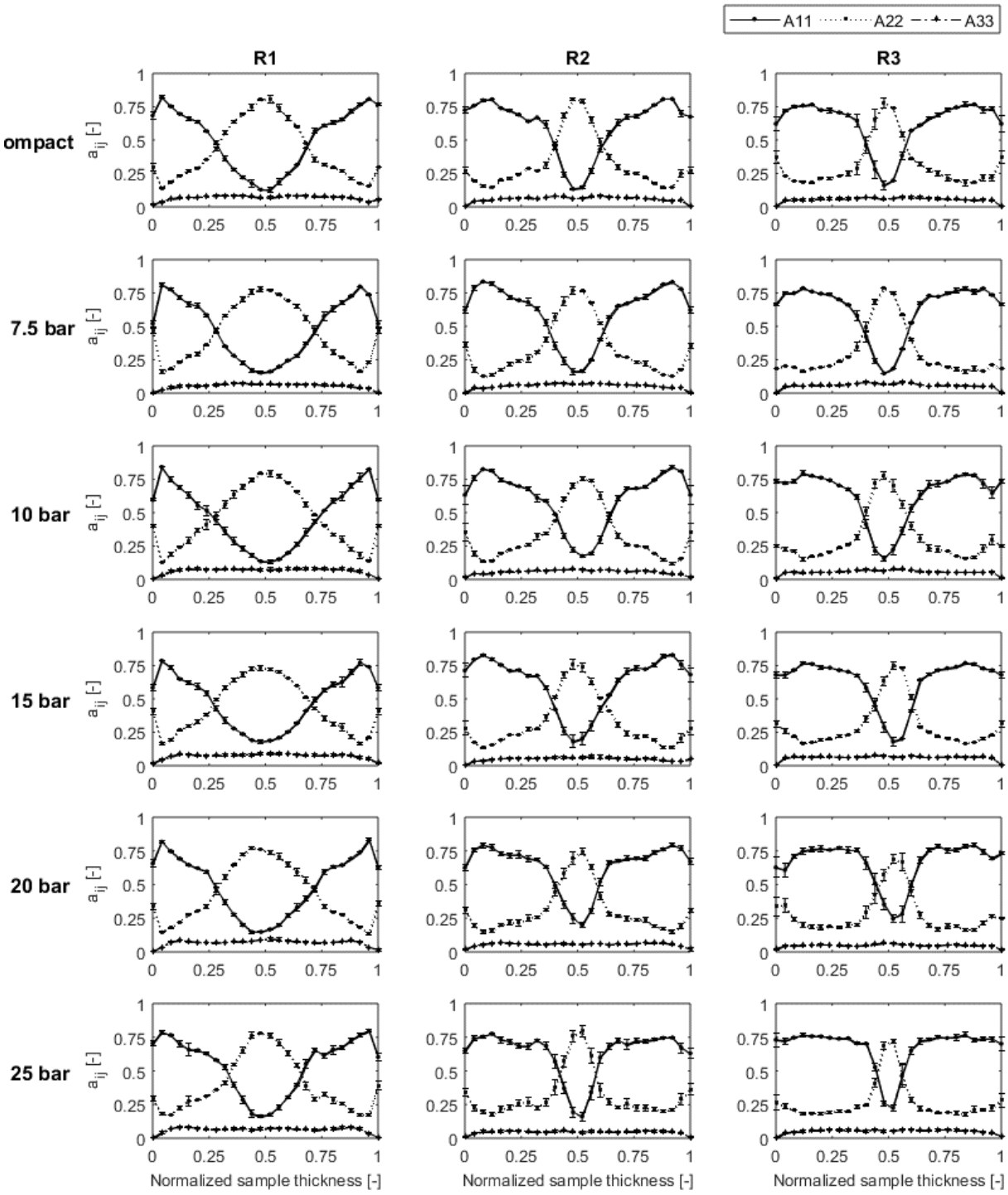

Figure 2.12. FO as a function of gas pressure and location. Close to gate (R1), center (R2), and end of flow path (R3).

While FO is mainly dependent on processing conditions for compact IM, Figure 2.10 and Figure 2.12 clearly showed that PBA content has an impact on the final FO in MIM parts. Gas acts as a plasticizer and changes the rheology of the matrix material, hence giving fibers the ability to rotate easier [12], [140]. However, the

high FC present in this work increases melt viscosity and favors fiber-fiber interactions. Both can act as obstacles that hinder fiber rotation [140]. Additionally, it has been reported that the presence of gas causes fiber disorientation due to cell growth around fibers [14], [138], [141]. Shaayegan et al. experimentally studied carbon fiber rotation during bubble growth in polystyrene melt. They reported that fibers in close proximity to a growing cell experience rotational and translational displacements or a combined motion of both due to the melt's biaxial stretching [141]. Shaayegan et al. also showed that a growing bubble continuously increases the fiber's angle and its distance from the cell center. Additionally, multiple fibers move closer to each other in the radial direction as the cell grew. Fibers with a closer initial location to a bubble exhibited a greater magnitude and rate of rotation. It was also found that fibers with a smaller initial angle resulted in a greater degree of FO [141]. It can be clearly seen that the presence of gas results in a more complex FO distribution analysis, as growing cells push fibers out-of-plane [138], [141], [142]. A displacement of glass fibers due to bubble growth can be seen in Figure 2.13.

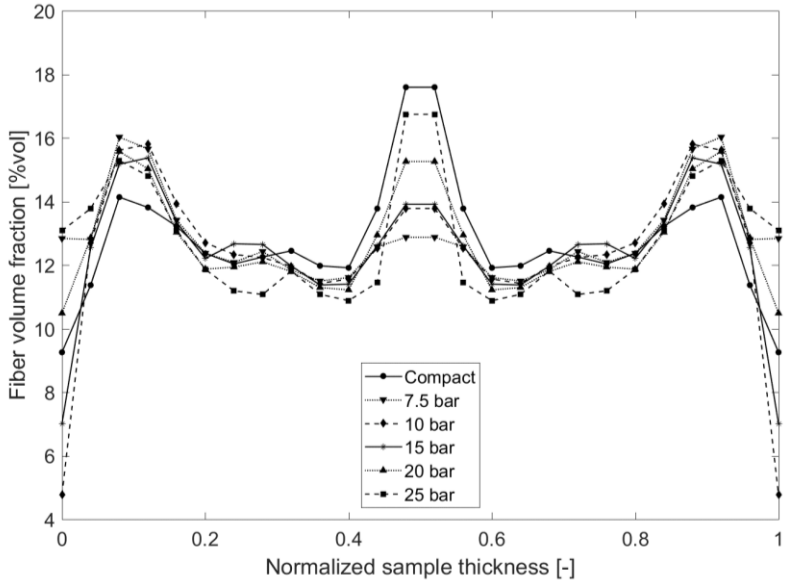

Figure 2.13. Symmetrical FC as a function of gas pressure at location R2 (center). Data does not include error bars to ease visualization. Standard deviation is on average 0.5 vol%.

Measurements indicated a maximum fiber volume fraction in the core layer for compact samples. Shell layers and surface regions showed fewer fibers. At 7.5 bar and 10 bar, the FC dropped by 27% and 22% in the core when compared to compact IM samples as fiber volume becomes occupied by growing cells. At low gas pressures, cells have a high growth rate, resulting in large bubbles (Figure 2.3). As those cells keep growing, fibers are significantly displaced towards the shells, visible in a FC increase of 16% and 14%,

respectively. This results in FC distributions which have their maximum in the shell layers rather than the core. At high gas pressure (25 bar), cell growth rates slow down, and cells are smaller. Fibers are only slightly displaced from the core, resulting in a FC peak that resembles the compact one. Only a 5% FC reduction was recorded in the core. FC dropped in the shells compared to lower pressure settings, however, the FC was still elevated when compared to compact plates. It was further noticed that FC reduced in the transition layer between core and shells with increasing gas pressure. Figure 2.12 shows that fibers in that transition layer are predominantly oriented in flow direction. Thus, growing cells not only displace fibers from the core, but also induce a fiber re-orientation along the flow direction (Figure 2.14). This factor contributes to the increase in global a_{11} observed in Figure 2.10.

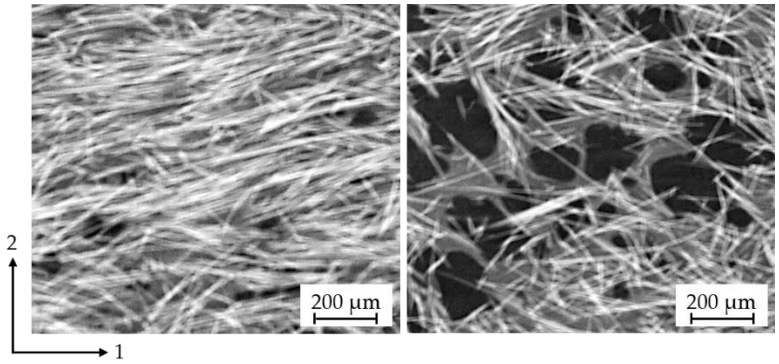

Figure 2.14. Core region of compact and 7.5 bar specimen in the center of the plate (R2). Left: fibers orderly oriented, right: displaced fibers due to cell growth.

2.3.3 Impact on Flexural Properties

Interior automotive components are mainly exposed to bending loads; thus, their mechanical flexural behavior is from high interest [143]. To correlate the obtained MS of foamed parts to their flexural modulus, Digimat-MF and COMSOL Multiphysics were used.

Through-thickness fiber and cell data were discretized into 15 layers. A global FL value was employed. The discretized data was used to create a representative volume element (RVE) using Digimat-MF, a mean field homogenization tool (Figure 2.15). For each layer, the tool uses as input the full orientation tensor, the fiber volume fraction, the global FL, the void volume fraction, the cell aspect ratio, and the mechanical properties of each of the phases. A two-step homogenization procedure was employed to determine the stiffness constants for each individual layer. First, pseudo-grains were formed and homogenized using the Mori-Tanaka homogenization model. Mori-Tanaka can accurately estimate effective properties of two-phase composites for volume fractions of inclusions less than 25% [144]–[146]. Since the maximum fiber and void

volume fraction were measured to be below 17% and 7%, respectively, the use of the Mori-Tanaka model is appropriate. Second, the effective response of the homogenized pseudo-grains was computed with the Voigt model [146]. The stiffness matrix for each layer was obtained for the elastic regime of 2% deformation.

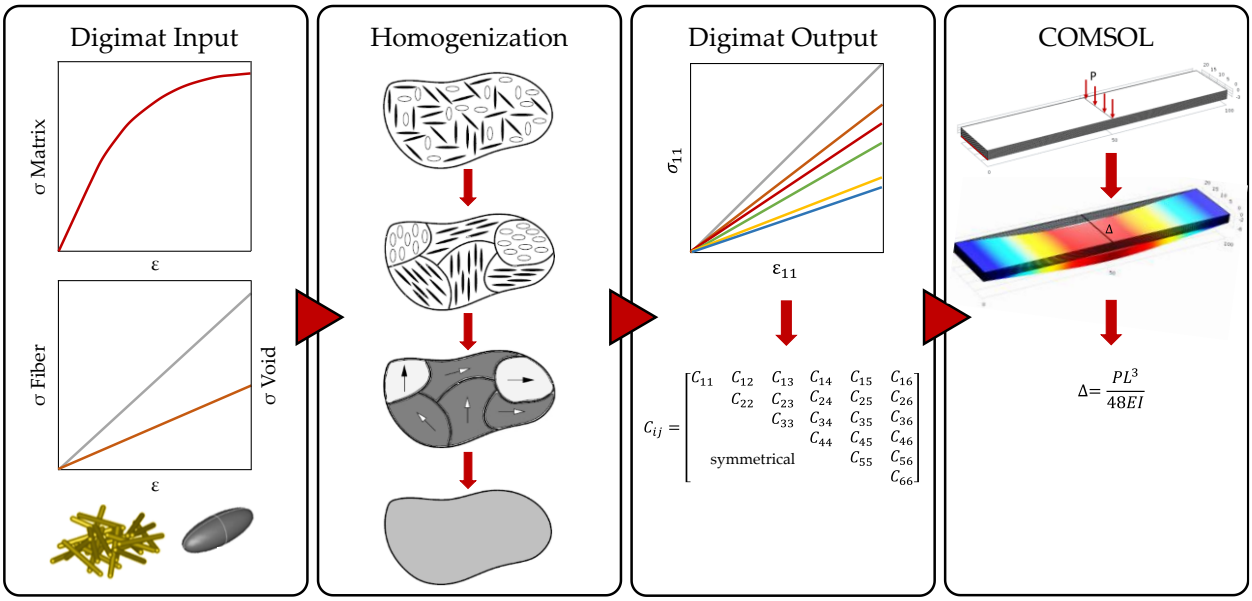

Figure 2.15. Workflow for flexural modulus determination.

A 15 layered composite beam was generated in COMSOL Multiphysics (Figure 2.15, right). For each layer the corresponding stiffness matrix was imported from the Digimat MF analysis. A 3-Point bend test was performed with an applied vertical center load of 200 N/m. With the obtained deformation (Δ), the modulus E was calculated as follows

$$\Delta = \frac{PL^3}{48EI} \tag{24}$$

where Δ represents the deformation, P the applied force, L the beam length, and I the moment of inertia. The thickness-wise equivalent elastic modulus used for COMSOL predictions is shown in Figure 2.16. As discussed in the previous chapter, the presence of gas affects the fiber MS. Cell growth pushes fibers from the core towards shell regions. This explains the lower elastic modulus seen in the center of the plate for foamed parts. In the shell regions, however, the modulus increased compared to compact samples.

Mechanical properties of MIM parts depend on morphological parameters such as CS, CD distribution and cell aspect ratio; however, their effect is from lower importance than part density and skin thickness [42], [147]. Since stresses are mainly supported by the exterior layers during bending, foamed plates with

ultimately the strongest outer layer (thickest skin (Figure 2.17, center), highest FC, highest global alignment in a_{11}) will show the highest modulus.

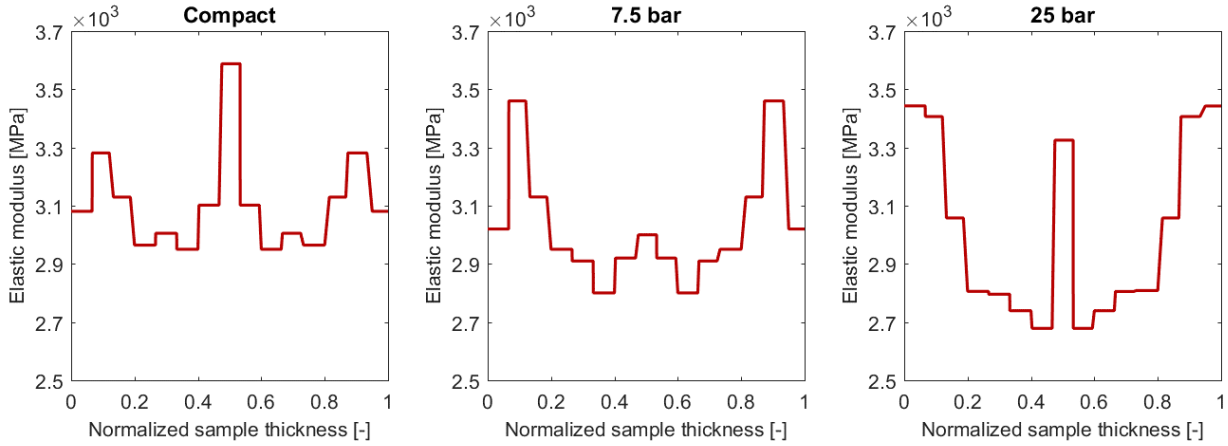

Figure 2.16. Elastic modulus for compact and foamed specimen measured at the center of the plate (R2).

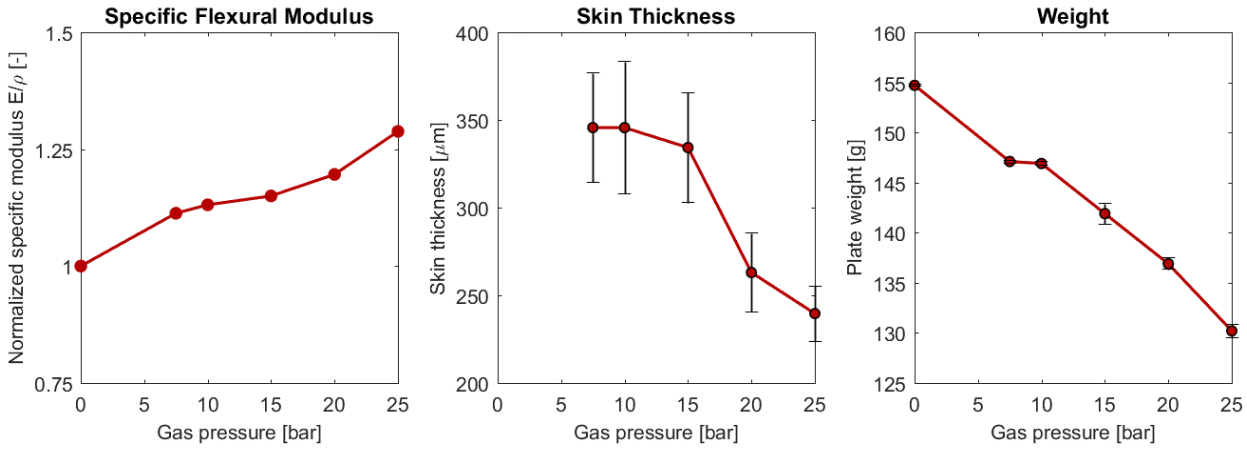

Figure 2.17. Left: Normalized specific flexural modulus, Center: skin thickness, and Right: part weight.

Interior automotive parts are required to have high a stiffness to weight ratio. Thus, composite materials are foamed to improve specific mechanical properties per unit weight. The normalized specific modulus (E/ρ) as a function of gas pressure is shown in Figure 2.17, left. As expected, E/ρ increases with PBA content. This means that parts become stronger per unit of weight. Under a bending load the normal stresses are maximum at surfaces and zero at the neutral axis. The foamed core reduces the density of the MIM part, and less material is available to support stresses. However, since in bending stresses are zero or low in the foamed core, the specific flexural modulus can be higher than that of solid materials.

2.4 Conclusions

This chapter studied the gas pressure operating window of the novel MIM technology, Ku-Fizz™, and its effect on the cell and fiber MS. Experimental results showed foamed plates exhibiting a shell-core-shell behavior for cell and fiber MS due to the fountain flow. CD predominantly increased, and CS decreased with gas pressure and with melt flow direction. As CD increased, the bubble aspect ratio decreased. At high gas pressure settings, Ku-Fizz™ was able to achieve CDs as high as $5.1*10^5$ cells/cm^3 and CSs as low as 55 μm. FL increased with gas pressure due to the reduced melt viscosity. A distinct narrowing of the core and a marked change in global FO were recorded with increasing gas pressure. It appears that growing cells induce a fiber re-orientation along the flow direction. FC distribution graphs showed fibers moving towards the mold surface due to cell growth. This phenomenon was more notable for low gas pressures due to the increased growth rate. Introducing gas causes a complex foam and fiber MS that affects the mechanical and physical properties of the final part. By using Digimat MF and COMSOL Multiphysics the effect of different MSs on the flexural behavior was analyzed. The introduced anisotropy due to bubble growth led to stiffer shells and increased specific modulus of foamed parts.

3 Mechanical response of fiber-filled automotive body panels manufactured with the Ku-Fizz™ MIM process

3.1 Introduction

The previous chapter has shown that the foam and fiber MS obtained with Ku-Fizz™ differs from the leading microcellular foaming technology, MuCell [148]. We reported that the introduction of gas and the presence of foam cells significantly modified the fiber MS. Thus, the next step involved evaluating how this particular MS impacts the mechanical response of molded components. For this purpose, the mechanical response of a SCANIA AB inner truck door panel was evaluated, and the difference in response of the foam and compact (=unfoamed, standard density IM part.) part was assessed. This door panel is used in all SCANIA trucks and is assembled to the cab door. Several components, such as an electric control unit, a door lock, a door window winder mechanism and motors are assembled to the door panel.

The principal design attributes for these assembled door bodies are static stiffness, strength, fatigue durability, crashworthiness, and vibration frequency response [149]. The typical door assembly needs to withstand and channel loads into the body of the car. These loads could be horizontal and vertical in nature, such as the force applied in opening or closing doors while leaning/resting on them or when stepping on the armrest to access the roof, [150], [151]. Door panels also need to withstand a side impact collision to protect the occupant's chest and pelvis from door contact [152]. Studies on a Sedan showed doors being one of the highest energy absorbing components (15%) during a side impact event [153]. Door panels also respond dynamically to loads, which is measured in terms of their vibration [154]. Body panels are designed to avoid resonance with vehicle vibration occurring during normal operation (Table 3.1) [155]. Vibrations are induced by a number of sources, including road surface conditions, revolutions of the engine, the brake/suspension system, and the tire imbalance [149], [156], [157].

Table 3.1. Sources of vibration. Frequency value for (*) a light truck equipped with automatic transmission, 787 mm tires, traveling at 80 km/h in overdrive, and (°) assuming a maximum engine speed of 6000 rpm.

Vibration source	Frequency [Hz]	Reference
Suspension and wheel	~10	[158], [159]
Engine*°	<100	[158]
Body	25-40	[159]
Driveline	50-150	[158], [159]
Road defects	<200	[159]–[162]
Door slam	<170	[163]

3.2 Experimental

3.2.1 Material and manufacturing of door panels

The material used in this study was a commercially available 30 wt% long glass fiber-reinforced polypropylene (SABIC STAMAX™). Pultruded pellets have a nominal FL of 15 mm. The fiber diameter was measured to be 19 ± 1 μm using an optical microscope. The material was dried at 80 °C for 4 hours to remove any moisture.

SCANIA AB R-Series truck door panels (813 mm x 457 mm x 2.2/2.0 mm) were molded by Idé-Pro on a 1000-ton Demag Ergotech 1000/1400-5200 IM machine equipped with a Ku-Fizz™ hopper unit (Figure 3.1). The processing settings are summarized in Table 3.2. The processing conditions are kept constant unless noted otherwise. The cavity was filled from 5 gates.

Figure 3.1. SCANIA AB R-Series truck door panel manufacturing process.

Table 3.2. Processing conditions for the IM trials.

Setting	Compact	Foamed
Gas pressure [bar]	0	20
Melt Temperature [°C]	245	245
Mold Temperature [°C]	50	85
Back Pressure [bar]	110	80
Injection Pressure [bar]	900	1200
Injection Time [s]	250 ccm/s	2.4
Holding Pressure [bar]	270	270
Holding Time [s]	15	0

3.2.2 Measurement of Microstructural Characteristics

The foam morphology and its representative values, CD and CS, were determined by the procedure outlined in [148]. The technique consists of grinding and polishing the embedded specimen, followed by a microscopy and an image processing step. Sampling locations are shown in Figure 3.2.

FO and FC were obtained with the X-ray microcomputed tomography approach described in [148]. The FL measurement procedure presented in [120] was employed in this work. This technique consists of fiber dispersion and a fully automated image processing algorithm to quantify the FL distribution. The Kunc-correction was applied to all results [121]. Sampling locations are shown in Figure 3.2.

3.2.3 Dynamic Mechanical Analysis

Viscoelastic and damping properties were analyzed with the TA Instruments Rheometric Series RSA 3 DMA equipped with a 35 N load cell. Tests were performed using a 3-point bending configuration with a 40 mm span. Specimens (44 mm x 12.7 mm x 2.06 or 2.15 mm) were extracted at various angles with respect to the flow direction as shown in Figure 3.2. As viscoelastic properties are independent of strain at low strain amplitudes, a strain sweep from 0.001-1% at 1 Hz was conducted to identify the linear elastic strain limit. Frequency sweeps from 0.1 – 100 Hz at a dynamic strain of 0.05% were conducted to obtain damping abilities ($tan\delta$) and storage modulus (E') for compact and foamed door panels. All tests were performed at room temperature.

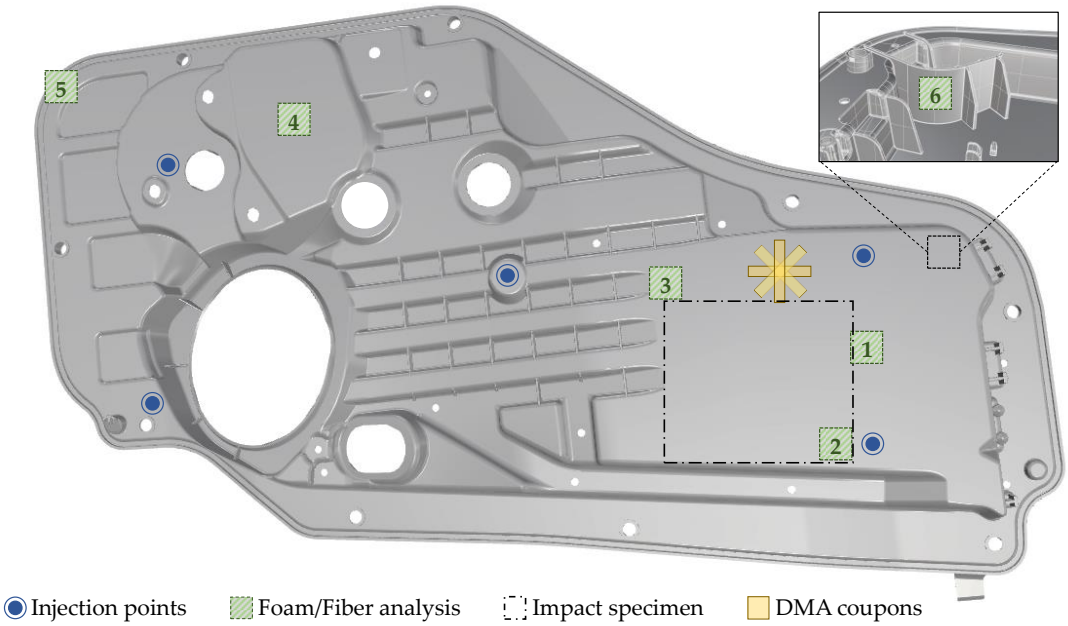

Figure 3.2. Sampling locations for full microstructure analysis (FL, FC, FO), foam analysis, impact tests, and DMA studies.

3.2.4 Drop-Tower Impact Testing

Rectangular specimens (152.4 mm x 101.6 mm x 2 mm) cut from the door panel (Figure 3.2) were tested under dynamic impact loading in accordance with ASTM D7136 [164]. Drop-weight impact tests were performed using the INSTRON CEAST 9350 Accelerated Drop Tower Impact System fitted with a 5.72 kg hemispherical striker at the University of Wisconsin-Madison. The impact energy was set to 5 J (1.35 m/s); determined from preliminary tests at various energy values. In total, one compact and three foamed samples were tested. The CEAST DAS 8000 JUNIOR data acquisition system with a sampling rate of 500 kHz recorded force, displacement, and energy versus time responses. An anti-rebound mechanism was activated to avoid multiple impacts on the specimens. The Photron FASTCAM Nova S6 high-speed camera with a frame rate of 15000 fps was used to record sample deformation and assess consequent damage propagation.

3.2.5 Vibration Testing

To estimate the modal properties of the door panels, a free-free vibration hammer tap test was performed. The panels were hung on an adjustable steel frame with elastic strings as shown in Figure 3.3a.

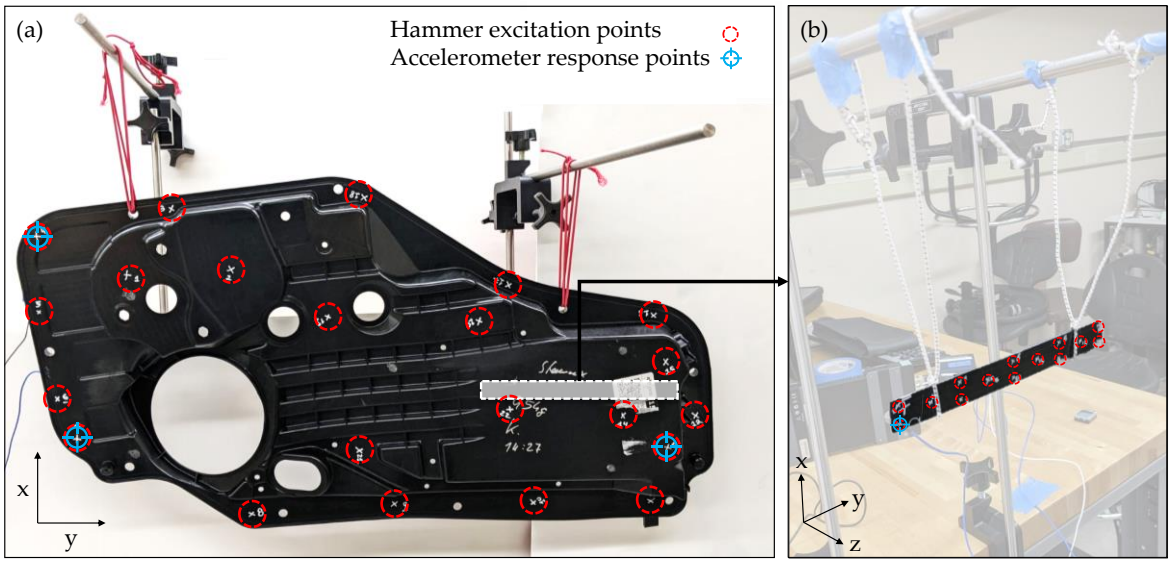

Figure 3.3. Input and response locations for the hammer tap test. Accelerometers are placed on the backside of parts. (a) Door panel. (b) Beam extracted from door panel.

Three accelerometers (PCB Piezotronics Model 353B15) were adhered to the panels using Petro Wax at edge positions that would allow detection of bending and torsion in the panel. The accelerometer wire was fixed to the table holding the steel frame. This reduced unwanted noise in the data and minimized the effect of the wire on the stiffness of the elastic suspension of the beam. The part was tapped with a nylon-tipped

impact hammer (PCB Piezotronics Model 086C03) on 22 different locations spaced along the door panel, including the accelerometer locations. The locations of the accelerometers and the hammer input locations are shown in Figure 3.3a.

For each hammer input location, the hammer signal and the three-accelerometer signals were recorded with a data acquisition system (Bruel & Kjaer Lan-Xi 3160 A-042 Generator Module). The time domain signals were processed to estimate the frequency response functions (FRF) for each of the three accelerometer locations versus the hammer input location. This was repeated for five hammer taps at each input location, and the resulting FRFs were averaged. Each hammer tap that contributed to the average was verified to ensure the hammer made a single contact with the door panel. Figure 3.4a shows an example of the measured signal from a hammer input. The sharp peak represents a 9.82 N impulsive force. In Figure 3.4b decaying oscillatory signal is shown with a maximum initial peak which decays to near zero after 0.8 seconds of response time.

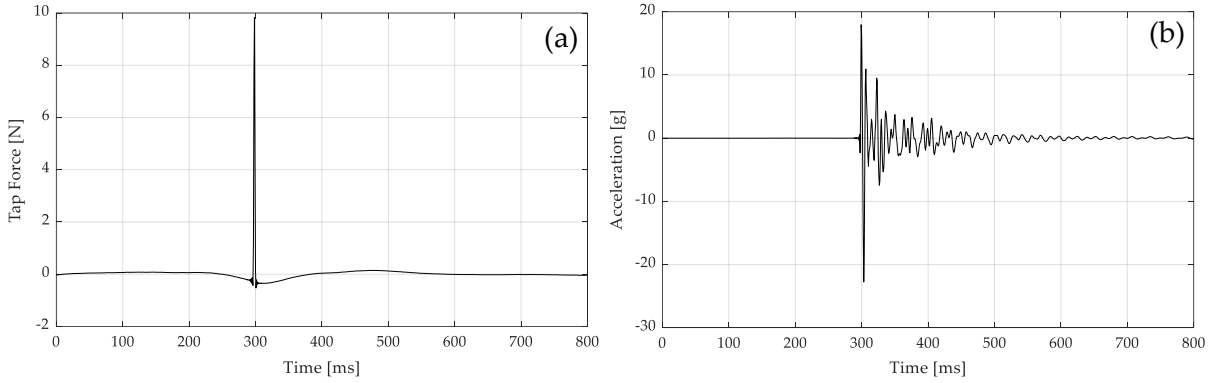

Figure 3.4. (a) Example of the time response of a hammer tap. (b) Accelerometer response.

The algorithm of Mode Isolation (AMI) was used to determine the natural frequencies and damping ratios of modes in the response [165]. First, the 22 sets of measurements and the associated FRFs were organized into a FRF matrix. The FRF matrix was input to AMI. AMI fits a multi-modal model to a composite of all FRFs. The fit was verified against the FRFs from the measured results to verify the best possible fit was achieved.

A modal assurance criterion (MAC) analysis was conducted to examine the similarity between compact and foamed mode shapes [166]. The MAC was calculated according to equation 27, where mode j is compared to mode k

$$MAC_{jk} = \frac{\left|\phi_j^T \phi_k\right|^2}{\left|\phi_j^T \phi_j\right|\left|\phi_k^T \phi_k\right|} \tag{25}$$

Additionally, testing of beams (Figure 3.3b) was conducted to estimate specific bulk material properties. Beams of dimensions of 23.0 mm x 25.5 mm x 2.2/2.0 mm were cut from door panels as shown in Figure ***3.3*** (compact specimen have increased thickness). The testing protocol outlined for door panels was followed. One accelerometer was used. The beam was tapped at 14 different locations uniformly spaced along the beam. FRFs were estimated from the time signals. Five responses were averaged, and modes were fitted to the resulting FRFs using AMI. As a first approximation of how microcellular foaming affects the average properties of the composite material, the mode fits were used to estimate the elastic modulus E of the beam samples as follows

$$E = \frac{\omega_n^2 \rho A L^4}{\alpha_2^4 I} \tag{26}$$

where ω_n is the n^{th} natural frequency associated with a particular mode shape, ρ the material density, A the cross-sectional area of the beam, L the beam length, the α_n as the eigenvalue, and I the cross-sectional second moment of inertia about the z-direction. This estimate was achieved by assuming beams could be represented by a classical Bernoulli-Euler beam model. The development of this model can be found in [167]. The density was calculated to be 1120.02 kg/m^3 and 1024.1 kg/m^3 for compact and foamed beams, respectively.

3.3 Results and Discussion

3.3.1 Foam Microstructure

Ku-Fizz™ produced a cellular structure within the foamed door panels, providing a reduction in material usage and part weight of 90 g or 10 %. Figure 3.5 illustrates the MS of a compact and foamed specimens. No voids were found for compact panels. A well-defined cell MS was present even in thinner features such as ribs and insert holders. At the stagnating weldline (Location 1) a reduced CD was observed, which can be caused by a combination of factors. First, the head-on collision of two melt fronts results in a spike of pressure. Cell nucleation and growth could be suppressed or even reversed by this sudden pressure increase (Figure 3.6). Second, FC at the melt front is higher (8 %) than the nominal FC [116]. Since fibers are nucleation points, the melt front fills with many small cells which are easily collapsed by the pressure spike.

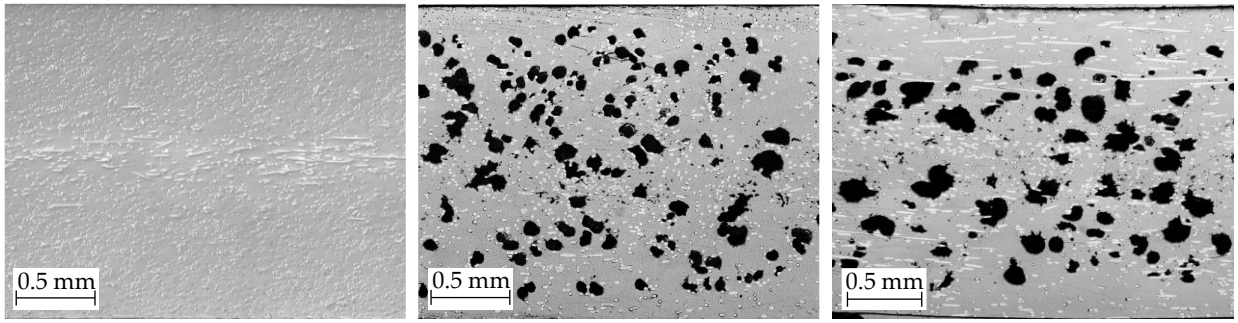

Figure 3.5. Microscopic images of cross-sections of compact and foamed specimen. Small black dots in the core region represent polishing defects.

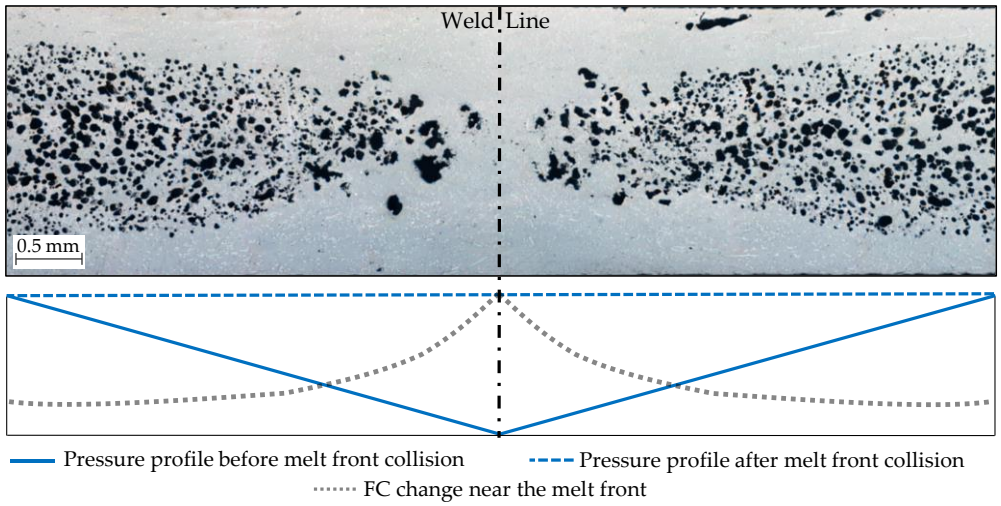

Figure 3.6. Top: Microscopic image of weldline. Bottom: Schematic of pressure as a function of sample for before and after melt front collision.

Global and thickness-wise CD and CS data can be found in Figure 3.7 and Figure 3.8, respectively. CS gradually increases towards the core region. The core has increased melt temperature and reduced matrix viscosity which allows cells to grow for a prolonged time. As cell growth and cell nucleation are competing mechanisms, CD drops in the core layer and increases in the shell regions [14], [122], [125], [126]. All samples showed a solid skin layer which is caused by the rapid solidification of the melt [127], [134]. Similar to fiber microstructure, CD and CS distributions impact the mechanical response of foamed components [143].

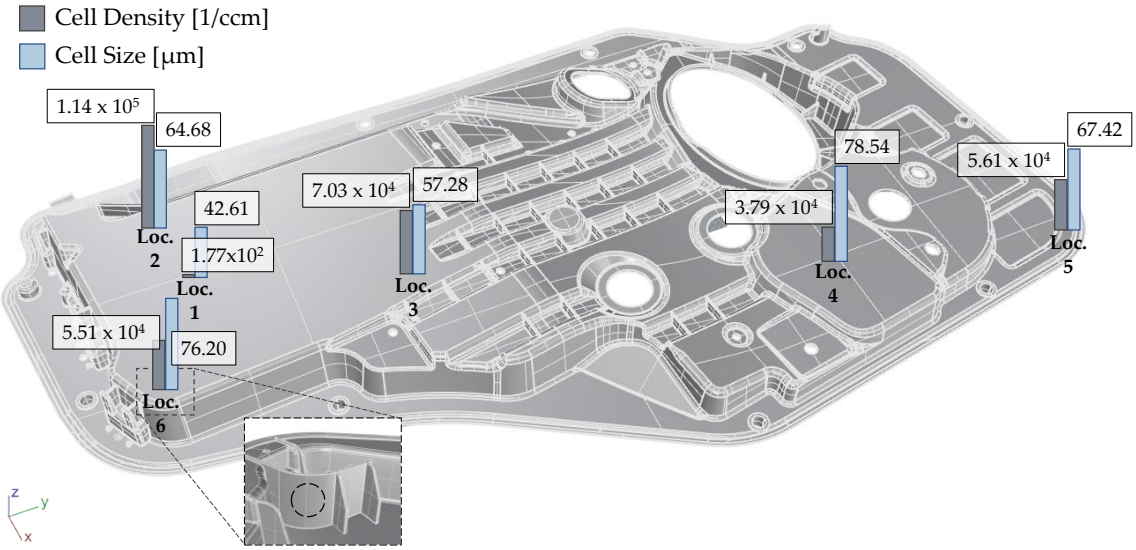

Figure 3.7. Global characteristic values of foam microstructure.

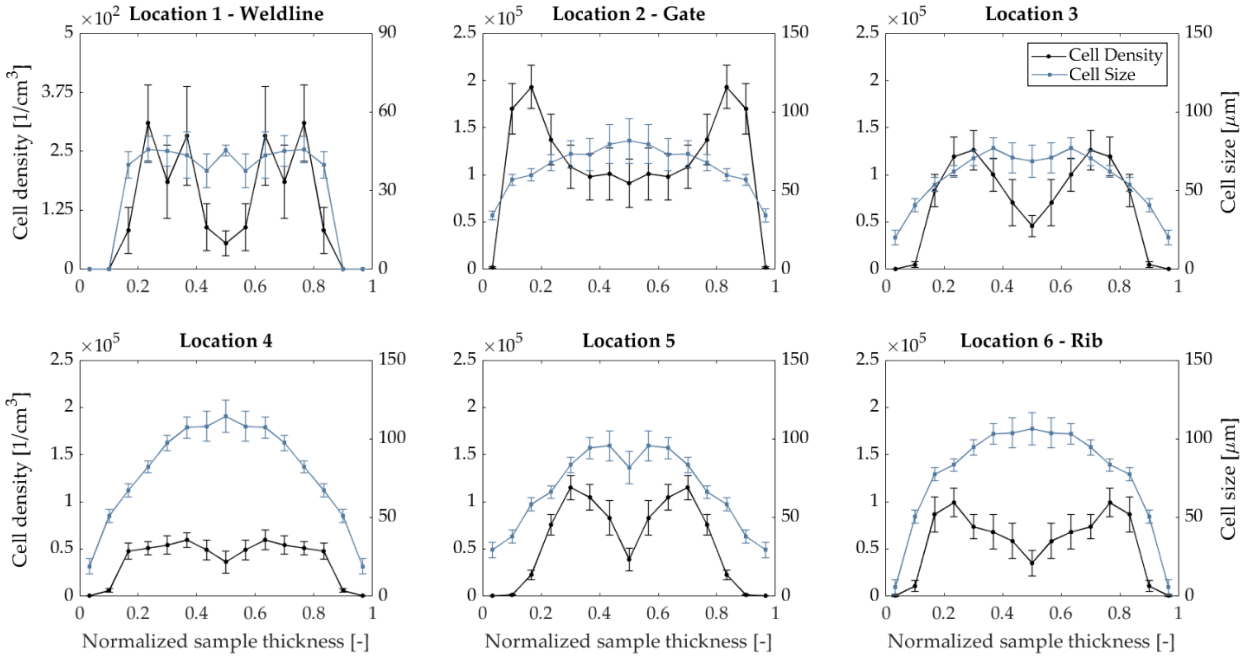

Figure 3.8. Cell density and cell size across the part thickness for compact and foamed door panels.

3.3.2 Fiber Microstructure

As shown in Figure 3.9 and previous work [12], [148], processing of glass fiber-reinforced PP in the presence of gas reduces the occurrence of fiber breakage during processing. For foamed and compact panels, a weight average length, L_W, of 1.89 mm and 1.67 mm were recorded, resulting in a 14% increase in FL. While L_W values significantly differ, a number average length, L_N, of 0.82 mm was obtained for both, compact and

foamed parts; this implies that very long fibers were preserved in the foamed panels. Dissolved gas acts as a plasticizer, reduces melt viscosity, and thus reduces fiber attrition [12]. Largest Lw values were recorded at the gate and at the edges of the panels (Figure 3.9). Close to the gate, fibers experienced shorter flow length and therefore have experienced a gentler stress history leading to an increased Lw. As shown by Bechara, 2021, longer fibers tend to accumulate at the melt front and are deposited where the melt front stops. Fibers travelling in the melt front come from the core layer where stresses are low and, thus, damage is reduced [168]. Increased FL at the end of the flow path was also noted by Goris and Phelps et al [116], [137]. Partially undispersed fiber bundles were observed in compact and foamed panels (Figure 3.10). Since dissolved gas acts as a plasticizer, it would be expected that foamed parts have poorer dispersion and more undispersed fiber bundles. However, no significant difference was observed between foamed and compact parts. Intact fiber bundles act as stress concentrators and result in aesthetic problems.

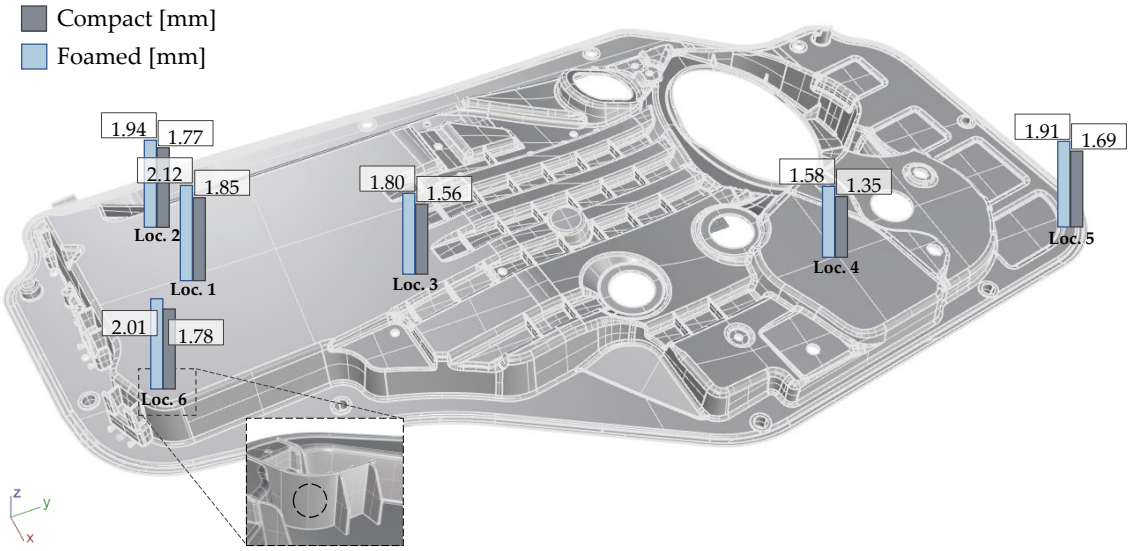

Figure 3.9. Global characteristic values Lw of fiber microstructure.

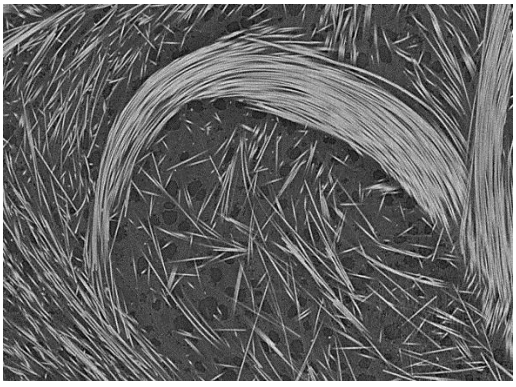

Figure 3.10. Undispersed fiber bundle in foamed door panel at location 3.

The presence of gas changes the matrix rheology, effectively modifying the velocity profile and its effect on FO. Additionally, bubble growth displaces and re-aligns fibers [12], [140], [148]. The global FO for compact and foamed panels is shown in Table 3.3. Close to the gate FO is mostly random due to the shorter flow length and the limited time for fiber alignment under the radial flow inside the cavity. Fibers gradually become aligned perpendicular to the flow direction (A_{xx}) as the flow distance increases [169]. Location 1 represents a weldline of about 0.5 mm in width extending throughout the part thickness. It can be seen in Figure 3.11 and Figure 3.12 that fibers at the weldline are predominantly oriented parallel (A_{YY}) to the weldline [170].

Table 3.3. Fiber orientation tensors for compact and foamed panels.

	Compact Panels			Foamed Panels		
Location	**A_{xx}**	**A_{yy}**	**A_{zz}**	**A_{xx}**	**A_{yy}**	**A_{zz}**
1 Weldline	0.22	0.75	0.03	0.28	0.68	0.04
2 Gate	0.39	0.56	0.05	0.46	0.50	0.05
3	0.60	0.35	0.05	0.64	0.32	0.04
4	0.50	0.43	0.07	0.53	0.44	0.03
5	0.52	0.40	0.08	0.59	0.37	0.04
6 Rib	0.05	0.26	0.69	0.04	0.19	0.77

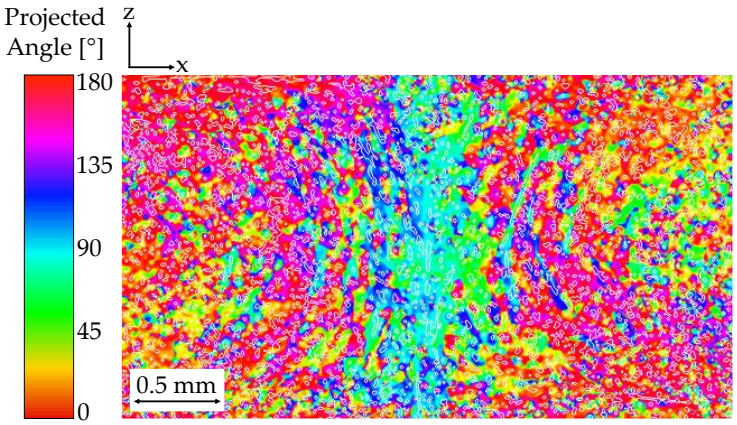

Figure 3.11. FO gradient approaching the weldline. Blue/turquoise colors indicate increased FO in A_{YY}. Red/pink fibers show alignment in A_{XX}.

Foamed panels presented slightly less alignment in flow direction when compared to their compact counterparts. These findings agree with published studies. Kim et al., 2019, found that cell growth induced randomization of the FO in MuCell foamed glass fiber-reinforced PP plates [171]. Yang et al., 2022, noted that foamed specimens exhibited a lower fiber alignment along the flow direction when compared to solid samples [172]. As FO is an important variable for fibrous composites, these changes in fiber alignment will impact the mechanical properties of the door panel.

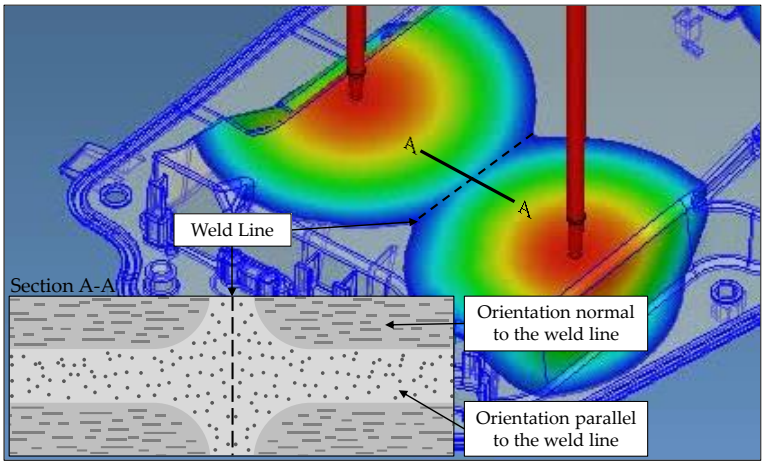

Figure 3.12. Schematic representation of the FO at a stagnating weldline. Moldex3D mold filling simulation was conducted by SimpaTec Inc.

Cell growth in the core region tends to displace fibers towards the mold surface, effectively changing the FC profile [148]. This phenomenon was observed for all sampled locations. Figure 3.13 shows how foaming impacts FC at three different locations. Even at the weldline, where cell growth is limited, a slight reduction of FC in the core is observed. Thickness wise fiber migration is an important effect as it directly impacts bending stiffness [116], [173], [174].

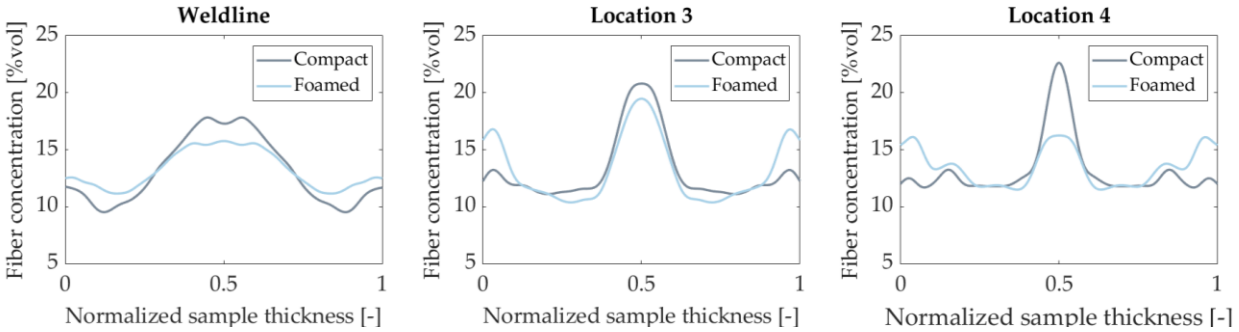

Figure 3.13. Symmetrical FC for compact and foamed panels at various sampling locations.

3.3.3 Dynamic Mechanical Properties

The behavior experienced during the dynamic strain sweep can be seen in Figure 3.14. Storage modulus (E') remains constant until a dynamic strain limit of 0.05% is reached. Above this value, collapsing of cells and non linearity of the matrix can occur.

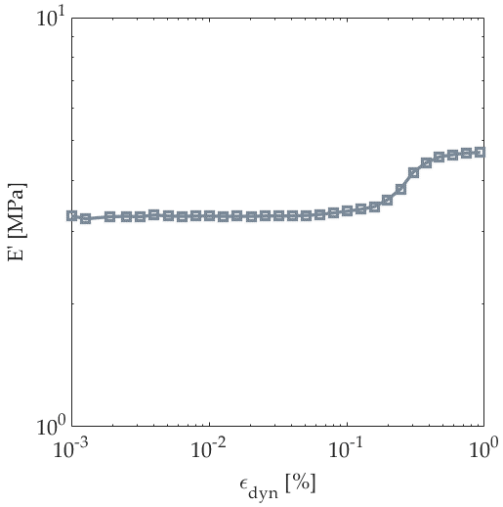

Figure 3.14. (a) Strain sweeps at constant frequency for composite door panels.

To study the difference in E′ between compact and foamed panels, coupons were cut in various orientations with respect to the flow direction to randomize the effect of FO. Measurements were taken until 46 Hz, as samples would lose contact with the bending fixture. Results from the isothermal frequency sweeps provide valuable insight into the behavior of door specimens at different time scales (Figure 3.15). E′ increases with frequency as the material appears stiffer. An average E′ of 5.99 GPa and 5.02 GPa was determined for compact and foamed specimens, respectively. Unfoamed panels showed a 20% higher E′ over the tested frequency range. However, when comparing the specific storage moduli, this gap was reduced to 9%. This finding highlights that foamed panels perform similar per unit of weight, making Ku-Fizz™ a good alternative for lightweighting of automotive door components.

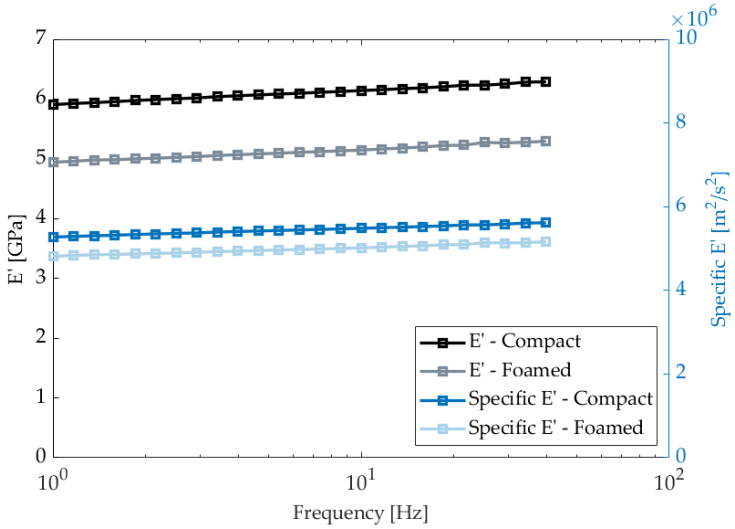

Figure 3.15. Average storage moduli and specific storage moduli for compact and foamed panels.

Average $tan\delta$ values of 0.0391 and 0.0394 were found for foamed and compact conditions, respectively, over the tested frequency range. The presence of cells does not significantly impact material damping. This can be attributed to the lack of cells near the coupon surface; the region that carries most of the bending stress. $tan\delta$ values showed little variation along the tested frequencies as glass fibers reduce $tan\delta$'s frequency dependence. These results align with previous DMA studies conducted on long glass-fiber reinforced PP [175].

3.3.4 Mechanical Response from Impact Tests

Figure 3.16a shows the representative force-displacement response of compact and foamed specimens. Based on the force-displacement responses, the equivalent impact stiffness was 222 N/mm and 310 N/mm for foamed and compact parts, respectively. The compact specimen exhibited a sharper drop in the post-peak regime, which indicates higher damage as higher energy is dissipated over a short global deformation (Figure 3.16a). Open-type curves, that is, no rebound, can be seen for all tests, indicating complete penetration and perforation of both types of samples [176], [177].

Figure 3.16b shows an increased impact force for a compact specimen as air bubbles near the surface cause foamed parts to fail more easily. To account for the difference in densities, the impact force was normalized with the respective sample weight. The gap in impact force reduced from 20% to 2% when values are normalized (Table 3.4). Thus, foamed door panels can compete with compact ones for weight-sensitive parts.

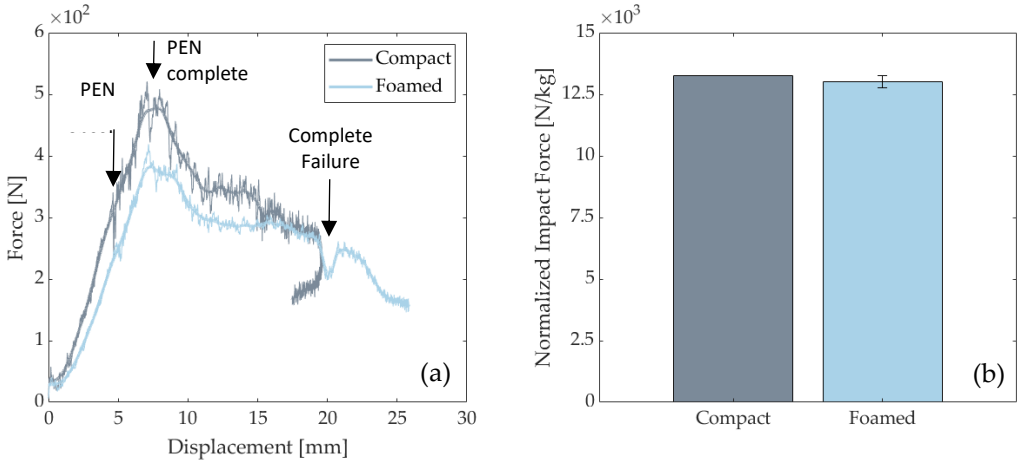

Figure 3.16. (a) Force-displacement plots of original and smoothed for compact and foamed specimens. PEN indicates penetration (b) Impact force normalized with sample weight.

Both compact and foamed specimens absorb impact energy by a complete failure. Figure 3.17a shows the energy-time graphs, where absorbed and impact energies are indicated. Figure 3.17b presents the weighted

normalized absorbed energy. Foamed specimens absorbed 33% more energy prior to complete failure than compact samples (Table 3.4). This is partially explained by the presence of air bubbles in the foam core, which act as dampeners. Additionally, the introduction of gas modifies the fiber MS, which also influences impact response. This explains the different energy/time curve types in Figure 3.17a as the foamed MS has the capacity to absorb higher energy per unit of mass.

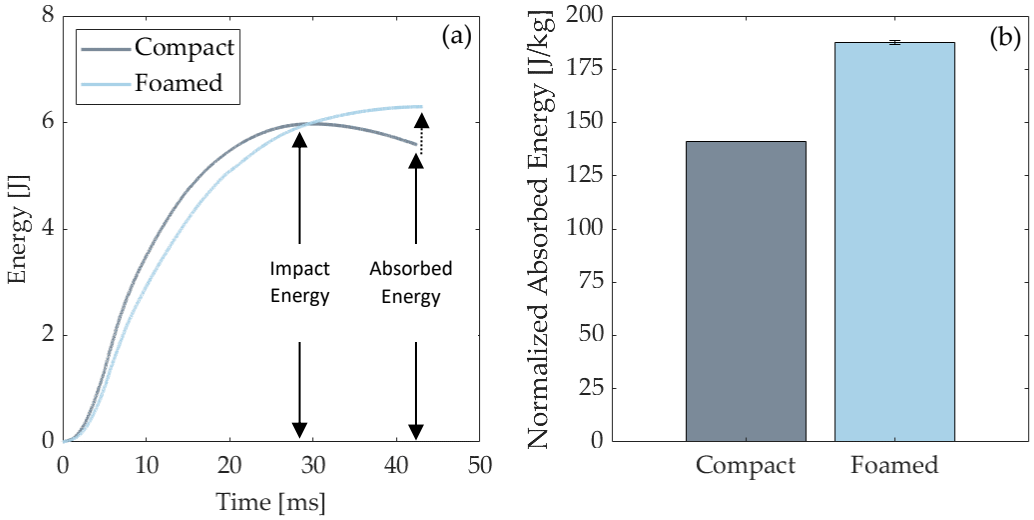

Figure 3.17. (a) Energy vs. time output. (b) Normalized absorbed energy for 5 J energy levels. Samples were normalized to their respective weights.

Table 3.4. Representative values for foamed and compact samples from drop-tower impact testing.

Specimen	Normalized Impact Force [kN/kg]	Normalized Equivalent Impact Stiffness [kN/mm/kg]	Normalized Absorbed Energy [J/kg]
compact	13.25	2.19	141.01
foamed	13.01±0.25	1.86±0.003	187.63± 1.07

Figure 3.18 shows the stages of the impact test. Upon impact, one can see elastic deformation (indentation and elastic bending), which is followed by the formation of cracks and ultimately complete penetration. As seen in the last frame for the foamed sample (t=10.5 ms), the crack propagates in the same direction as the flow path during mold filling. Since fibers are predominantly aligned with the flow, the sample is more resistant to failure due to bending in this direction [116]. Figure 3.19 illustrates the anisotropic microstructure and how fibers in plane B-B are normal to the load direction in the outer regions where stresses are highest. In this plane (B-B), the matrix will carry most of the load near the part surface leading

to an earlier failure, most likely due to debonding. This mode of failure is known as transverse cracking [178], [179].

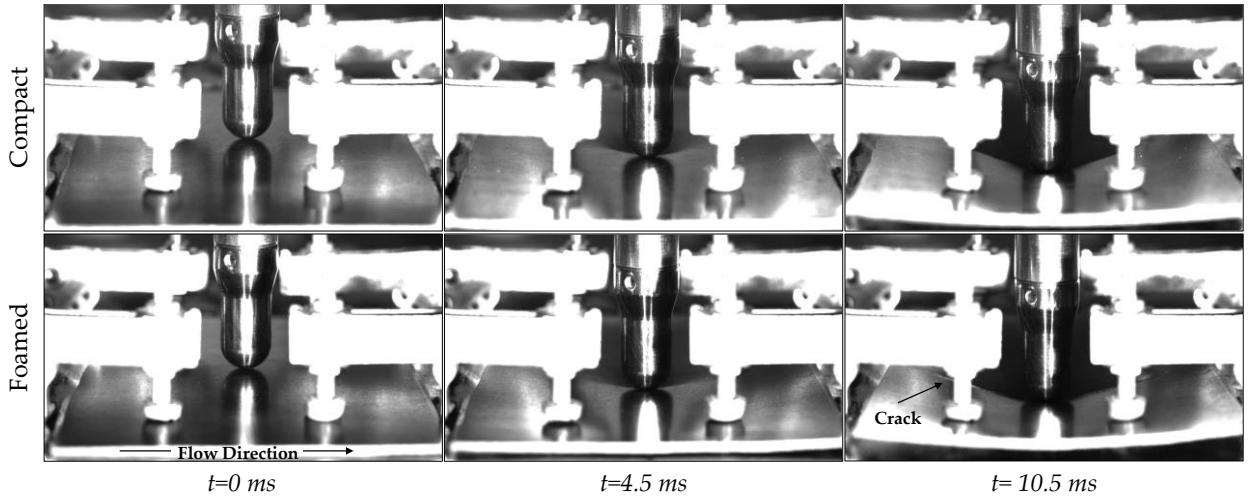

Figure 3.18: High speed camera images showing the impact event, the bending, and the deformation and fracture of a compact and foamed specimen.

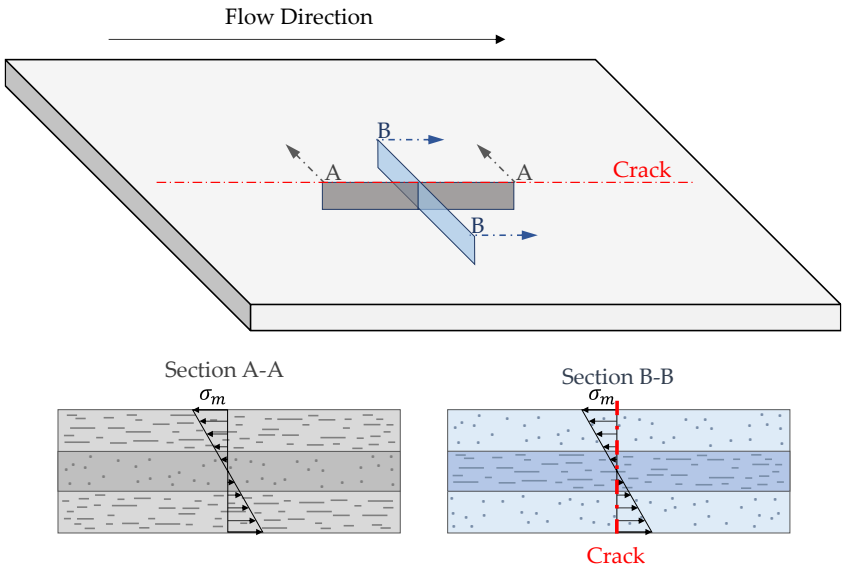

Figure 3.19. Anisotropic response of impact specimens.

Crack propagation was evaluated using micro-CT scans. Figure 3.20 shows examples of the secondary cracks formed perpendicular to the main crack direction. The presence of the foam core can have different effects on the crack propagation behavior due to hindrance caused by air cells. This can force the crack to undergo a tortuous path, which reduces the extent of crack propagation. In some cases, the crack can deviate from a straight path by following a weaker path generated by large cells and changes in fiber

density. For example, Figure 3.20 (left) shows the upper crack avoiding a high FC region caused by undispersed fiber bundles. In other cases, cells can relieve the high stresses at the tip of the crack and stop crack propagation [180], [181].

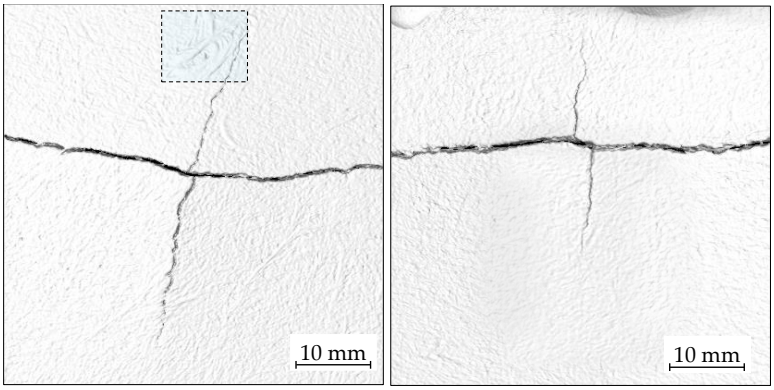

Figure 3.20. Transversal crack propagation on the back surface for compact and foamed samples. The highlighted area shows a high concentration of fibers due to undispersed fiber bundles.

Table 3.5 presents the length of transverse cracks. It can be seen that voids reduce transversal crack propagation by 50% on the impact plane, and 38% on the part's back side. This highlights how cells can reduce crack propagation in a similar way as drilled holes arrest crack growth in wind shields or aerospace panels [182].

Table 3.5. Transverse crack propagation length for compact and foamed specimen.

	Crack Propagation Length [mm]	
Specimen	**Impact side**	**Back side**
compact	15.15	21.10
foamed	7.58± 1.50	13.17± 1.45

3.3.5 Vibration Testing - Modal Analysis

Hammer-tap tests were conducted to determine the effect of MIM on the vibration response. Natural frequencies from modal analysis of acceleration FRFs were estimated by fitting prominent peaks in the composite FRF with AMI. The first two peaks in the range of zero to five Hz were not fitted as these modes were identified as rigid body modes of the panels on the suspension system and were omitted. Following all the individual fits, AMI refines a multi-mode model that includes all the individually fit peaks. Figure 3.21a shows an example of the AMI fit for a compact door panel. The composite of all 66 FRFs is shown in the solid line (FRF Data), the fit of the composite of the multi-mode fit (Fit) is represented by the dashed

line, and the difference between the FRF Data and the Fit (Residual) is shown by the solid red line. The residual is reduced from the FRF data by an order of magnitude for most of the frequency range, thus the fit matches the composite FRF curve well. Figure 3.21b shows the complex plane plot, also known as the Nyquist plot of the FRF. The peak with the highest magnitude in Figure 3.21a, corresponds to the crescent furthest to the right in Figure 3.21b.

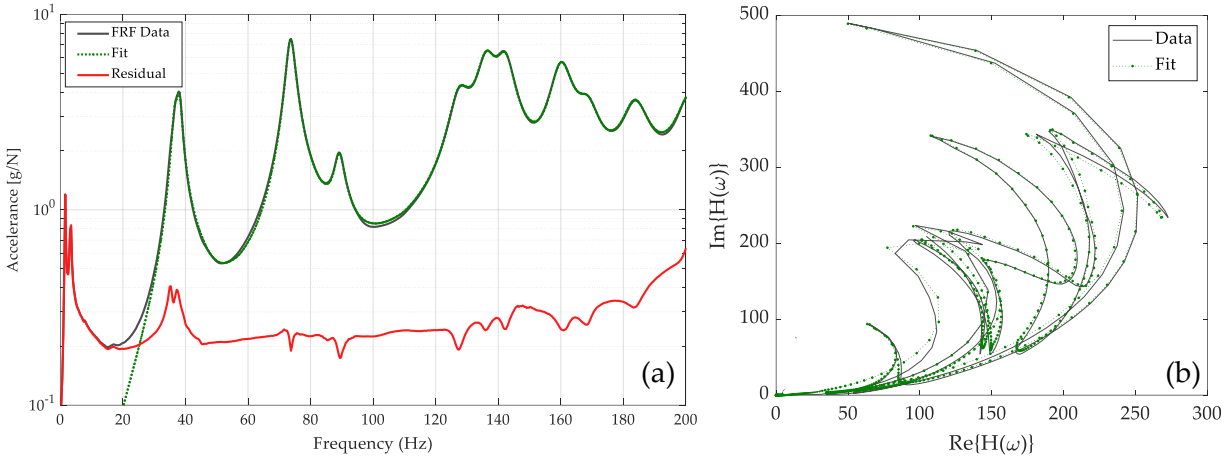

Figure 3.21. (a) Compact panel FRFs. The dark gray line indicates experimental FRF data, the green dotted line represents the AMI fit and the red line shows the residual (error) after refinement of a multi-mode model fit. (b) Complex plane plot of composite. H(w) is the FRF.

The composite FRF for the compact and the foamed door panels is shown in Figure 3.22. The natural frequencies and damping ratios were extracted from the AMI results (Table 3.6). Eleven modes were detected for both panels with frequencies that ranged from 36 Hz to 200 Hz, however, only the first 9 modes were reliable (low noise). The modes of the foamed panel are shifted in their locations of peaks and heights of peaks. Generally, the presence of gas in the MIM process shifted modes to lower frequencies as the static modulus decreases, the material becomes softer, and thus frequency decreases [183].

Regarding the damping of composite plates, it can be noticed that compact door panels exhibited better damping properties for modes 1, 3, 4, and 7-9 than their microcellular counterparts. This phenomenon could be explained by the presence of localized large voids introduced by the dynamic nature of MIM [184]. In addition, Suarez et al.,1985, reported increased damping characteristics for composites with low fiber aspect ratios [185]. In this work, compact panels showed reduced FL when compared to their foamed counterparts. For modes 2, 5, and 6, increased damping ratios were recorded for foamed parts. The presence of gas increases the crystallinity of the material, which in turn can increase damping properties [186]–[188]. Additionally, gas reduces the matrix viscosity which alters FO and FC, and thus effects frequency and

mode characteristics [148], [189], [190]. Bozkurt et al., 2016, found that the damping characteristics of basalt/epoxy composite laminates strongly depend on FO [191]. In general, material damping in fiber-reinforced composites is a complex phenomenon that causes difficulties in obtaining accurate damping ratios. This is likely caused by measurement errors that are large in comparison to the FRF amplitudes, thus making quantification difficult.

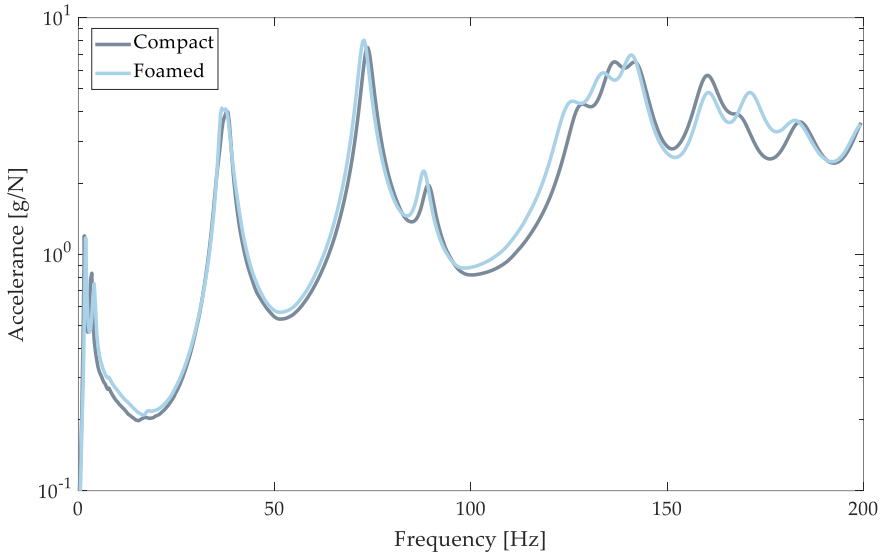

Figure 3.22. Composite FRF of compact (solid gray) and foamed (solid blue) door panels.

Table 3.6. Estimated natural frequencies, mode descriptions and damping ratios for the first 9 modes of door panels.

	Frequency [Hz]		Damping Ratio [%]		Mode Description
	Compact	Foamed	Compact	Foamed	
Mode 1	36.73	36.37	2.95	1.99	Plate Mode 1
Mode 2	38.06	37.79	2.15	2.72	Bending along y-axis
Mode 3	73.65	72.67	1.98	1.92	Plate Mode 2
Mode 4	89.20	88.04	1.87	1.78	Bending along x-axis
Mode 5	127.62	124.67	2.44	2.64	Plate Mode 3
Mode 6	136.21	133.38	2.19	2.41	Plate Mode 4
Mode 7	142.36	141.03	2.11	2.00	Bending along y-axis
Mode 8	160.11	160.30	2.10	2.01	Bending along x-axis
Mode 9	168.60	170.90	2.15	2.00	Bending along y-axis

Plate mode shapes for compact and foamed panels are shown in Figure 3.24. Their corresponding mode descriptions based on visual inspection can be seen in Table 3.6. Modes are labeled as plate modes if they display both bending and torsion prominently, where corners opposite each other on a diagonal across the

panel deflect with the same phase but are out of phase with the nearest corner on an edge. Modes are labeled as bending modes if the shape is dominated by bending and exhibits minimal torsion. Analyzing Figure 3.24, similarities between mode shapes are evident, with local differences in deflections. For example, mode 1 for the compact panel deflects more relative to the rest of the panel when compared to its foamed counterpart. More differences can be noted. However, quantifying these variations visually proves difficult as door panels are large, complex specimens with complicated features and cutouts. To study the similarities and differences between modes quantitively, a MAC analysis was performed (Figure 3.23). If modes are identical, the orthogonality properties of modes yield a value of 1. If mode shapes differ, a low MAC value is attained. Typically, diagonal values greater than 0.95 and off-diagonal terms less than 0.1 are desired to confirm mode shape alignment. Figure 3.23 shows four diagonal values less than 0.95, with the lowest diagonal term being 0.74. There are 17 off-diagonals greater than 0.1, with the largest off-diagonal term of 0.29. Modes 1, 2, 8, and 9 show differences between compact and foamed door panels. Modes 2, 8, and 9 are primarily bending modes. Variations in these modes indicate that the MS of foamed panels affect bending strains more significantly than torsional strains.

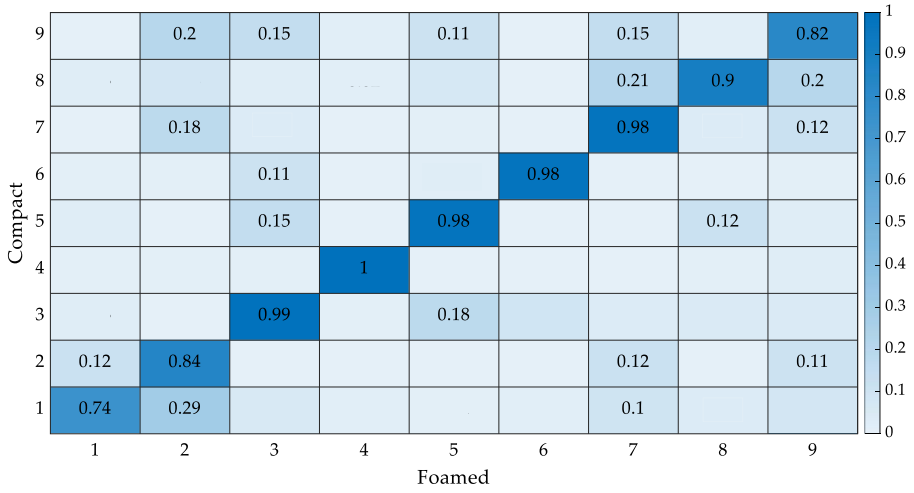

Figure 3.23. MAC matrix. Mode shapes above a MAC value of 0.1 are displayed.

It is important to note that the composition and structure of the object, material anisotropy, part density, L/T ratios, and the manufacturing process all influence the vibration response at various degrees, and thus, changes in modes and their shapes cannot be reduced to one physical characteristic. Vibration response characteristics and thus mode shapes are affected by cell generation, which in turn affects the fiber microstructure. This work has shown that the presence of gas results in an increase of FL, modifies the FC

profile, and increases normal to flow fiber alignment due to reduced matrix viscosity. Longer fibers and higher fiber volume fractions increase the stiffness of foamed panels and therefore increase natural frequencies [191]. During injection, cell nucleation and bubble growth cause fiber migration towards mold walls, leading to door panels with stiffer shells; simultaneously, the presence of a foam core reduces stiffness. Additionally, mode shapes vary with physical characteristics such as density and part thickness [192]. Part mass decreased by 10% and average part thickness decreased by 6% when using MIM. As shown by Talekar et al., 2020, and Shishir et al., 2022, for bending, as part thickness decreases, natural frequencies decrease as well [193], [194]. This decrease was also observed in the present study.

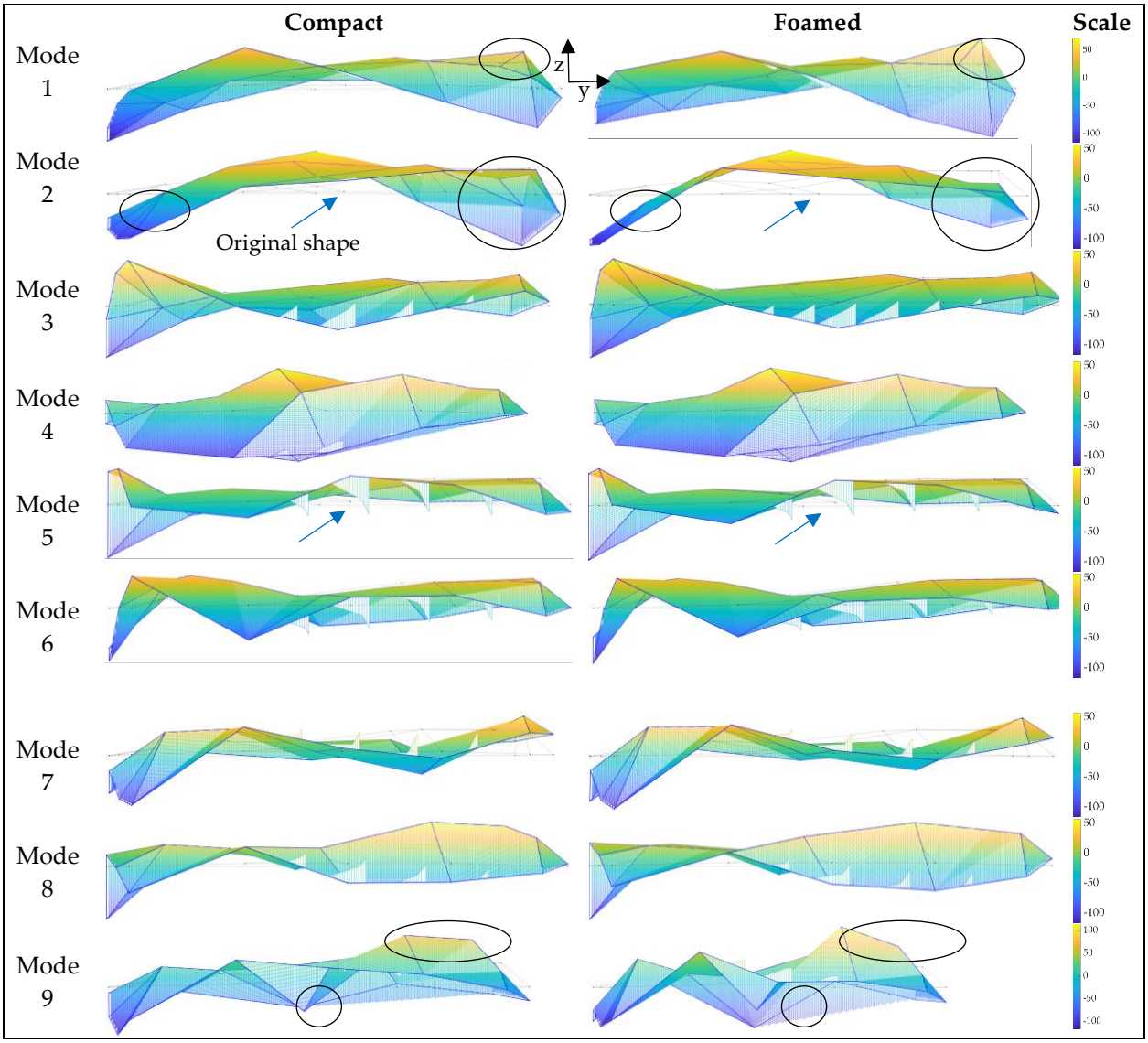

Figure 3.24. Plate mode shapes for compact and foamed door panels. Dotted lines represent the undeformed wireframe of the panel (indicated by arrows). Circles highlight local differences in deflection. Lined triangles jutting from the part are caused by the employed surface color visualization method.

Beam cutout samples were also used to reveal differences between foamed and compact door panels. The frequency span was limited to the first three natural frequencies, and the corresponding composite FRFs are shown in Figure 3.25. Three distinct peaks can be seen, ranging from about 70 to 600 Hz. Their mode shapes were inspected and consisted of the Bernoulli-Euler beam bending modes 1, 2, and 3. Their frequency values and damping ratios are listed in Table 3.7. For foamed panels, peaks are shifted to lower frequencies by about 6% for each mode. Damping ratios in the foamed beam increased by about 8% for the first and third modes and was reduced by 2% for the second mode.

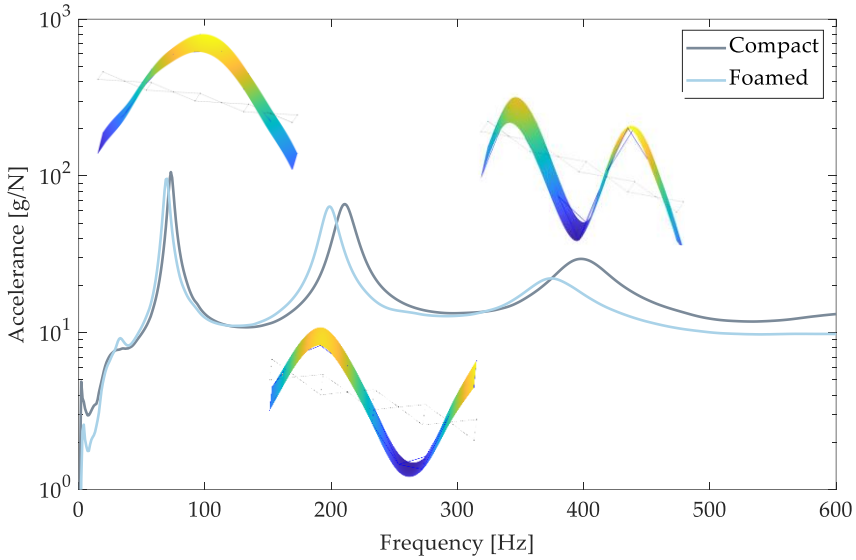

Figure 3.25. Composite FRF of compact and foamed beams. Mode shapes are shown for the foamed beam cut-out.

Table 3.7: Estimated natural frequencies, mode descriptions and damping ratios of tested composite beams. All bending modes are along the y-axis.

	Frequency [Hz]		Damping Ratio [%]		Mode Description
	Compact	**Foamed**	**Compact**	**Foamed**	
Mode 1	72.98	69.41	2.80	3.01	Bending Mode 1
Mode 2	210.65	198.50	3.44	3.37	Bending Mode 2
Mode 3	395.70	370.83	5.94	6.51	Bending Mode 3

The estimated elastic modulus is shown in Table 3.8. Elastic moduli ranging from 3.28-3.93 GPa were observed. A decreased modulus of about 8% was noted for foamed beams when compared to their compact counterparts. This indicates that for bending strains, the microstructure of foamed panels reduces the panel stiffness when using a first approximation to the anisotropic structure. This decrease in modulus is caused by the reduced density of foamed beams as well as the reduced natural frequencies. As door panels are interior automotive components, they are required to have a high stiffness to weight ratio.

Foaming improves specific mechanical properties. The estimated specific modulus (E/ρ) slightly increased by 1% for the foamed beam specimen. For a more accurate modulus determination, a smaller impact hammer should be used to reduce noise in vibration responses. Additionally, a model accounting for the anisotropic behavior of composite beams will yield a more accurate representation of the material behavior.

Table 3.8. Estimated specific elastic moduli.

	Compact $[m^2/s^2]$ x10^6	**Foamed** $[m^2/s^2]$ x10^6
Mode 1	3.58	3.36
Mode 2	3.93	3.61
Mode 3	3.61	3.28

3.4 Conclusions

The MS resulting from the Ku-Fizz™ process caused relevant changes in the mechanical response of door panels. The introduction of gas affects structural variables in two ways; first, it generates a cell distribution, second, it modifies the matrix rheology, and thus, it impacts the main fiber characteristics (FL, FC, FO). For foamed panels, 14% increase in FL (L_W), increased randomization of FO, and fiber displacement towards the mold surface were observed. Cell MS analysis revealed high CDs and small CSs close to the cavity wall and decreased CD and larger cells in the core region of the part. CD values up to 1.14 x 10^5 were recorded. The impact of gas on the MS varies in magnitude and is dependent on the gas pressure operating window, which is one of the main differences between traditional MIM Mu-Cell and the more recent technology Ku-Fizz™.

For DMA testing, a 3-point bend configuration and 0.05% strain were used. For these conditions, compact samples showed a 20% higher E' over a 1-50 Hz frequency range. $tan\delta$ exhibited little difference between foam and compact specimen. Modal analysis revealed a shift towards lower frequencies for MIM panels. The general shape of the vibration modes presented little change. The modulus determined from the beam cutout sections decreased for foamed samples for the first 3 modes of vibration. Unexpectedly, the presence of foam cells increased the absorbed energy before reaching a complete failure during impact testing. Cells act as stress relievers, slowing down or hindering crack propagation in the transverse direction.

As vehicles become lighter, even percentual weight reductions can represent important savings in battery life and fuel efficiency. In this study, there was a 10% weight reduction for foamed door panels. However, weight reduction comes at the cost of decreased mechanical performance. Although it is difficult to draw

direct correlations between individual MS variables and the mechanical response due to the complex geometry and mold filling pattern, it is useful to look a generalized properties to assess the impact of MIM. Figure 3.26 presents the comparison of specific properties of the foamed part with respect to the compact one. Except for absorbed energy, the compact material still performs better per unit of mass. Yet, studies have shown it is possible to increase some specific properties by using MIM [195], [196]. Optimizing the performance for foamed LGF composites is no trivial task. Therefore, design and material engineers need to include the interaction between fiber and foam MS in their design consideration during component development. Modeling tools have improved to the point where both microstructural variables predictions are fairly accurate. Nevertheless, strong understanding of the underlying physics is necessary to make the right decisions during the simulation process.

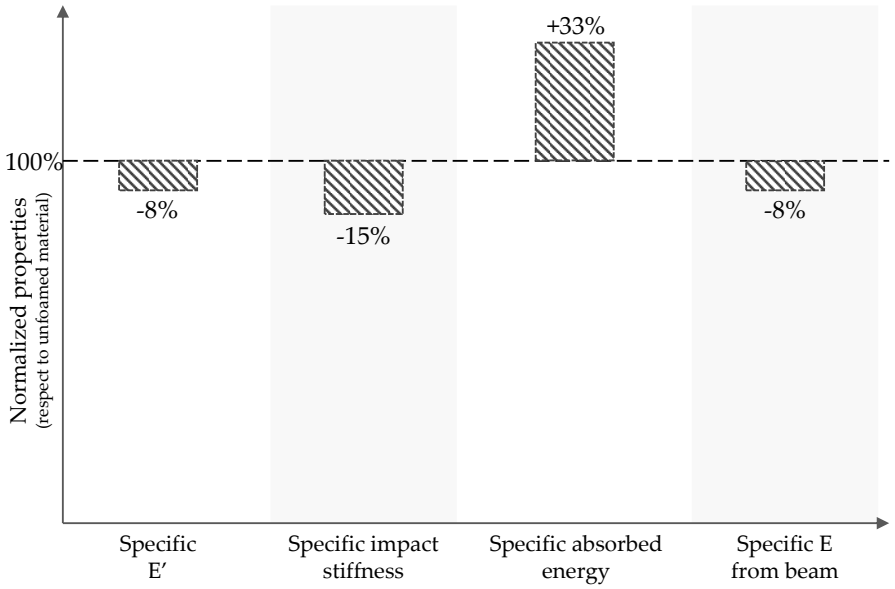

Figure 3.26. Normalized mechanical properties with respect to compact specimen.

4 Modeling and Simulation of the Ku-Fizz™ Technology

4.1 Introduction

To aid Ku-Fizz™ into becoming an appealing and competitive process within the automotive industry, the underlying physics of this technology must be well understood. Implementation of the process in current mold filling simulation tools to predict the foam MS is key. Commercial software, such as Moldex3D, have implemented cell nucleation and bubble growth models into their simulation suite and found good results in predicting the foam MS for simple MuCell foamed components. Since there are key differences between Ku-Fizz™ and MuCell technologies, the purpose of this work is to evaluate if the current model and its implementation in Moldex3D can predict the foam MS from the Ku-Fizz™ process in an accurate way. In case the prediction is not accurate, the model and its parameters will be modified based on the specific physics of the Ku-Fizz™ process to better describe the foaming kinetics.

This work is divided into four sections which address the steps taken to simulate the Ku-Fizz™ MIM process using Moldex3D.

i. The gas dynamics along the different stages of the process will be studied. The concept and pressure operating window of Ku-Fizz™ are notably different compared to the market leader MuCell. Ku-Fizz™ has multiple mechanisms of gas diffusion into the polymer: gas diffusion into solid state pellets, gas diffusion into the melt boundary and mixing of gas into the melt pool. We will calculate gas diffusion times and gas contents in the solid and molten states of the polymer matrix.

ii. Evaluation of current mold filling simulation tools for foam MS predictions. Moldex3D has developed a simulation tool for MuCell. We want to verify if this tool can be used to predict the foam MS obtained with Ku-Fizz™ or if their model needs to be updated. Our approach is to, first, compare experimental data with simulations conducted with default FP. Secondly, perform a FPD, and finally, conduct cross validation simulation runs.

iii. As the core difference between MuCell and Ku-Fizz™ is the mechanism of gas injection, screw pull out experiments will be carried out to better understand the gas mixing behavior during plastication. From these experiments a pressure correction factor for the cell nucleation model will be proposed. Additionally, molding trials will be performed to determine this correction factor followed by a new FP optimization.

iv. Finally, the newly adapted model will be used to simulate the foam MS for a real complex automotive component. An internal door panel, injection molded with PPGF using Ku-Fizz™, will be used in this case study. Molding parameters will be used as input for the MIM simulation. The accuracy of the foam MS prediction will be evaluated against MS measurements taken at key locations over the door panel body.

4.2 Modeling Gas Diffusion and Gas Solubility in Ku-Fizz™

The rate of diffusion was calculated by employing Crank and Carslaw et al., diffusion equation for gas uptake for a hollow cylinder [197], [198]. A hollow cylinder approximation was employed as gas does not dissolve into glass fibers, and thus, gas diffusion is restricted to the polymer shell (Figure 4.1).

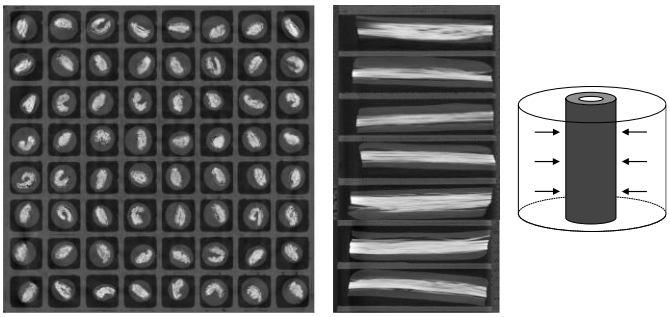

Figure 4.1. Left: Top view of SABIC pellets, center: side view of pellets, right: Pellets modeled as a hollow cylinder.

The solution for gas diffusion into a hollow cylinder can be obtained in terms of Bessel functions. Diffusion times were calculated by assuming a long circular cylinder in which diffusion is everywhere radial. As diffused gas is replaced with new one in Ku-Fizz™, no pressure drop will occur, thus, a constant gas concentration on the cylinder surface can be assumed. The gas concentration is initially uniform throughout the cylinder. Therefore, the amount of diffusing substance entering or leaving the hollow cylinder shell as a function of time can be described as

$$\frac{M_t}{M_\infty} = 1 - \frac{4}{b^2-a^2}\sum_{n=1}^{\infty}\frac{J_0(a\alpha_n)-J_0(b\alpha_n)}{\alpha_n^2\{J_0(a\alpha_n)+J_0(b\alpha_n)\}}exp(-D\alpha_n^2 t) \quad (27)$$

where M_t denotes the quantity of diffusing substance which has entered the cylinder in time t and M_∞ the corresponding quantity after infinite time. a and b denote the cylinder's inner and outer radius. D is the diffusion coefficient, J_0 are Bessel functions of the first kind of order zero and α_n are roots of J_0 providing that $J_o(a\alpha_n) = 0$ [198].

Experimentally measured diffusion coefficients for a PP/N_2 system obtained by [199] and calculated activation energies from [42] were used to determine diffusion coefficients for various temperatures by

$$\frac{D_1}{D_2} = e^{\frac{E_d}{R_g}\left(\frac{1}{T_2}-\frac{1}{T_1}\right)} \tag{28}$$

where D_2 is the diffusion coefficient of 1.54*10^{-7} cm^2/s at the corresponding temperature T_2 of 25 °C [199]. E_d is the activation energy of diffusion and R_g the ideal gas constant. Calculated diffusion coefficients are shown in Table 4.1. Gas diffusion is slow at room temperature and increases with elevated temperatures as gas molecules have greater kinetic energy. As a result, gas particles will move faster, thus also diffuse faster.

Table 4.1. Calculated diffusion coefficients for various temperatures.

Gas	E_d [kJ/mol]	D at 25 °C [cm^2/s]	D at 40 °C [cm^2/s]	D at 157.7 °C [cm^2/s]
N_2	34.31	0.02x10^5	0.03x10^5	1.09x10^5

Equation 29 and 30 can then be solved for the gas uptake ($\frac{M_t}{M_\infty}$). $\frac{M_t}{M_\infty}$ as a function of time is shown in Figure 4.2. The rate of gas diffusion was calculated for the upper and lower chambers of the Ku-Fizz™ hopper unit as well as until the material reaches its melting point (157.7 °C). Calculated gas diffusion times as a function of temperature to reach a 25%, 50%, 75% and 99% gas saturation are shown in Table 4.2. At increased temperatures, diffusion times significantly decrease leading to pellets being loaded with gas before reaching their melting point (theoretically). At increased temperatures (157.7 °C), diffusion times significantly decrease to 18 seconds and 52 seconds for a 25% and a 50% gas saturation, respectively. Gas diffusion can occur in solid pellets. However, given the high material throughputs, short cycle times (<60 seconds) and the brief time before melting, this mechanism is secondary when compared to gas diffusion into the melt. Additionally, Crank's and Carlslaw's model assumes an ideal case of an isolated pellet, in our case the packing and compressing of pellets slows down gas diffusion. Zones closer to the nozzle are kept at elevated temperatures and diffusion times into melt will further be reduced. Additionally, rotation of the screw will accelerate the gas uptake even further.

Table 4.2. Diffusion times for 25%-99% gas saturation of 30 wt% GF PP employing a hollow cylinder approximation.

Temperature [°C]	$t_{25\%}$ [min]	$t_{50\%}$ [min]	$t_{75\%}$ [min]	$t_{99\%}$ [h]
Ku-Fizz™ upper chamber [25 °C]	1.9	60.8	249.6	20.7
Ku-Fizz™ lower chamber [40 °C]	1.0	31.3	128.6	10.6
Pellet melting point [157.7 °C]	0.3	0.9	3.5	0.3

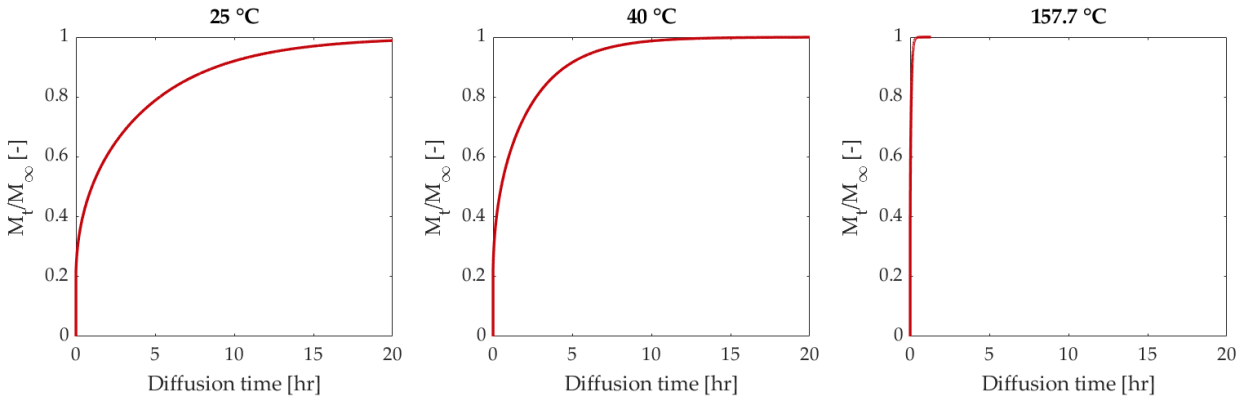

Figure 4.2. Gas diffusion times at different gas uptakes for a hollow cylinder at various temperatures.

For gas solubility calculations, experimental data from [41] and Henry's law with a temperature-dependent Henry's law constant were used [14], [24], [42], [44], [200], [201]. The enthalpy of sorption (E_s) was calculated as follow

$$\frac{S_1}{S_2} = e^{\frac{E_S}{R_g}\left(\frac{1}{T_2}-\frac{1}{T_1}\right)} \tag{29}$$

where S_2 is the solubility of N_2 in molten PP corresponding to temperature T_2. E_s represents the heat of solution and R_g the ideal gas constant. As shown in Figure 4.3, E_s increases with pressure. A positive E_s value indicates an increasing gas absorption with temperature. Therefore, no gas will exude from the melt and the gas remains solved as long as the melt pressure is higher than the gas pressure. A negative E_s value causes gas absorption to decrease with temperature. Therefore, diffused gas can leave the polymer again [80]. If E_s equals zero an equilibrium state is reached where temperature has no influence on gas solubility.

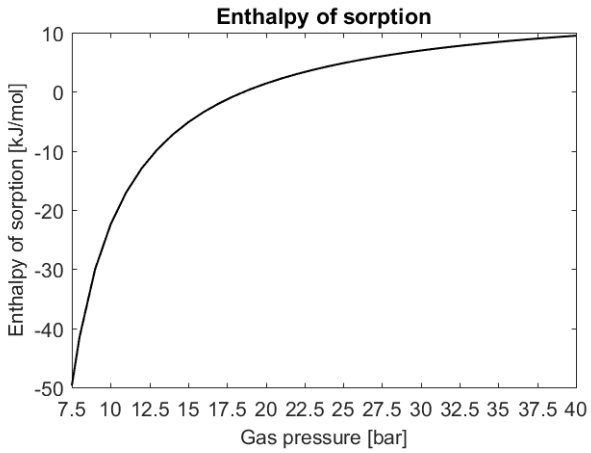

Figure 4.3. Enthalpy of sorption versus gas pressure calculated from published data from Sato et al. [45].

Equation 32 was used to calculate gas solubility at varying temperatures. Since gas only dissolves into amorphous regions of semi-crystalline polymers, results were corrected to account for the material's crystallinity of 42 % as follows

$$S_c = (1 - X_c)X_a \tag{30}$$

where X_c is the extent of crystallinity in PP, and X_a as the solubility of gas in the amorphous portion of the semi crystalline material [14], [42], [202]. X_c was determined with DSC measurements.

Given static conditions and unlimited diffusion times, Figure 4.4 shows the dissolved gas amount in both, solid pellet, and melt. Ku-Fizz™ can achieve a theoretical N_2 content of 0.2 wt% at 20 bar and 0.4 wt% at 30 bar. MuCell uses a common N_2 content of 0.1-1 wt% [16], [30]–[36]. Gas solubility is fairly constant at 20 bars since the value of E_s is 1.39 kJ/mol and thus, there is only a small temperature dependency. Below and above 20 bar, solubility is heavily dependent on temperature. An increasing gas solubility with temperature is typical for PP-N2 systems as they show "reverse solubility" [14], [41]. The jump in solubility at 175 °C indicates melting of crystalline regions, thus gas absorption capacity increases due the additional available amorphous regions. As Ku-Fizz™ is mostly operated at 20-30 bar to maximize CD, diffused gas will stay solved in the melt if the melt pressure is higher than the gas pressure.

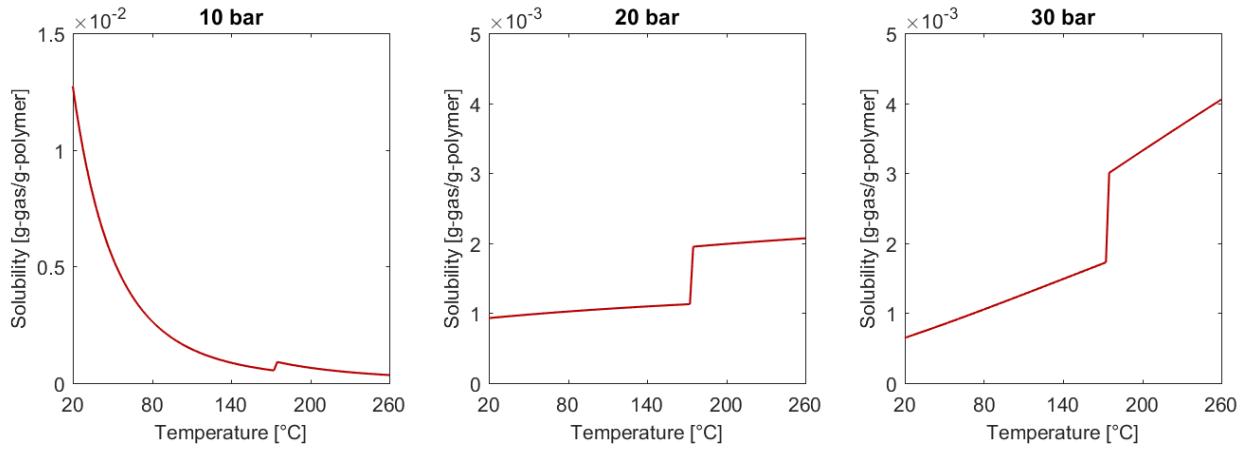

Figure 4.4. Solubility of N_2 in solid pellets and melt.

Solubility limits found in literature for a PP/N_2 system at 200 °C, for 35, 70 and 276 bar showed gas contents of 0.5 wt%, 1 wt%, and 4 wt%, respectively [36], [203]. Kastner et al., found dynamic solubility limits for PP/N_2 at 200 °C in foam IM of 0.6 wt%, 1.4 wt% and 2.4 wt% for 80, 140, and 200 bar, respectively [204]. The typical pressure range for MuCell is 80-200 bar, leading to typical employed N_2 contents of 0.1-1 wt% (Table ***4.3***). Ku-Fizz™ can employ a maximum gas pressure of 30 bar (50 bar possible with high pressure seals)

which leads to a maximum gas content of 0.3 wt% for 200 °C and 0.4 wt% for 260 °C. However, when comparing the calculated gas content and their effect on cell MS (Figure 2.3) with related literature, Ku-Fizz™ data shows CD's 1-2 magnitudes lower than MuCell, even though wt% calculations showed gas contents being within the MuCell range. This highlights that a static gas solubility calculation might not correctly represent the actual process. Given the complex process, where pellets are melting, mixing into the melt, generating gas pockets that later will be sheared, broken up and ultimately dissolved into the melt, a dynamic approach might be more accurate.

Table 4.3. Employed super critical nitrogen content for latest published work on MuCell foamed polypropylene.

Material	Melt Temperature [°C]	Nitrogen [wt%]	Reference	Publication year
20-30% CF PP	220 - 240	0.3, 0.5, 0.7	[205]	2022
20% CF PP	220	0.3, 0.5, 0.7	[206]	2021
10-30% CF PP	230	0.5, 0.7, 1	[207]	2020
20% GF PP	230	0.5	[208]	2020
iPP	200	48 bar	[209]	2019
PP	215	0.11, 0.23	[210]	2019
20% GF PP	240	0.5	[28]	2019
20% GF PP	210, 220	0.15, 0.5	[122]	2019
20% GF PP	235	0.76, 0.86	[107]	2018
20% GF PP	240	0.3	[211]	2018

4.3 Microcellular Injection Molding Simulations with Moldex3D

4.3.1 Injection Molding Trials

A simple plate geometry (400 mm x 100 mm x 3.5 mm) was molded on a Krauss Maffei 200–1000/390/CZ Multinject IM machine equipped with a Ku-Fizz™ unit. This work employed a 30 wt% glass fiber-reinforced PP (STAMAX PPGF30 YM 243) supplied by SABIC. The material was dried at 80°C for at least 4 hours to remove any moisture in the material. The processing settings followed the processing guidelines by SABIC™ [212] and are summarized in Table 3.2.

For foam MS analysis, three sub-samples along the center line of the part were extracted as shown in Figure ***2.1***, embedded into resin, grinded and polished. CD and CS values of microscopic images were obtained by using Image Pro. More information about the analysis technique can be found in [148].

4.3.2 Simulation Set-Up

The MuCell simulation tool in Moldex3D (Version R21) was used to predict CD and CS distributions. Simulation parameters are shown in Table 4.4. As the gas dosage amount is unknown in Ku-Fizz™, the gas saturation pressure (P_{sat}^{*}) simulation input was set equal to hopper pressure. For a valid quantitative comparison of simulation and experimental data, an accurate set of fitting FP (f_0, F) for the cell nucleation rate equation must be employed. Default FP can only be applied for homogenous nucleation. This work used a long glass fiber-reinforced PP, thus, a FPD needs to be conducted (Figure 4.5). Similar to Taki, 2008, f_0 and F were varied to fit the number density of bubbles to experimental data by a trial-and-error method [89]. Additionally, FP need to be adjusted to account for the foaming behavior seen in Ku-Fizz™. The optimized set of FP is shown in Table 4.4. Once determined, these FP can be applied to different processing conditions and part designs according to Moldex3D.

Table 4.4. Input parameter for injection foaming simulations.

Input Parameter	Value
Nitrogen Gas Pressure [bar]	7.5-25
Gas Molecular Weight M_w [g/mol]	28
Gas Diffusion Coefficient [cm²/s]	8.07 x 10^{-5}
Gas Solubility k_H [mol/(cm³Pa)]	3 x 10^{-11}
Surface Tension γ [N/cm]	1.78 x 10^{-4}
Threshold of Bubble $J(t)$ [1/cm³s]	0.1
Default f_0 [-]	7.4 x 10^{-25}
Default F [-]	1 x 10^{-3}
Optimized f_0 [-]	5.6135 x 10^{-24}
Optimized F [-]	9 x 10^{-4}

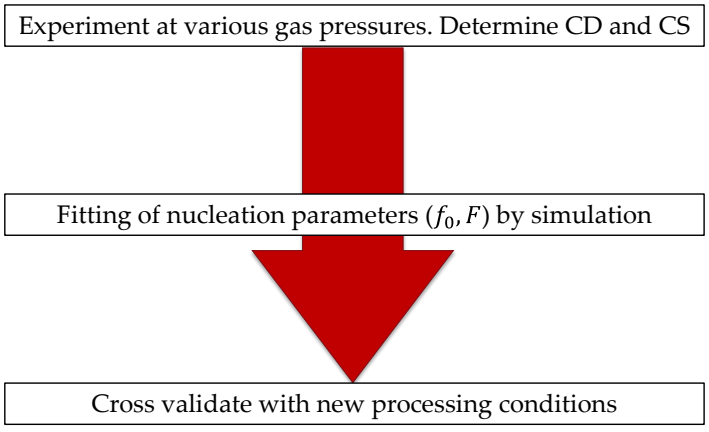

Figure 4.5. Fitting parameter determination flow chart.

Simulations employed the Han and Yoo model for the mass-transfer equation. The plate geometry was meshed with a fit boundary mesh and a solver accuracy of 1 was applied. For foaming simulations, a solid part weight of 154.7 g was used.

4.3.3 Simulation Evaluation

Process conditions from experimental trials were used to run equivalent simulations in Moldex3D to evaluate the performance of default FP. As shown in Figure 4.6 and Table 4.5, the simulation underpredicts CD and overpredicts CS, due to the low pressures employed in Ku-Fizz™. The foaming tool cannot account for the early introduction of gas and thus prolonged gas diffusion times. At low gas pressures the experimental data is magnitudes off from the predicted foam MS; with no foaming being predicted at 7.5 bar. This highlights the importance of an accurate determination of FP tailored to the material and process used.

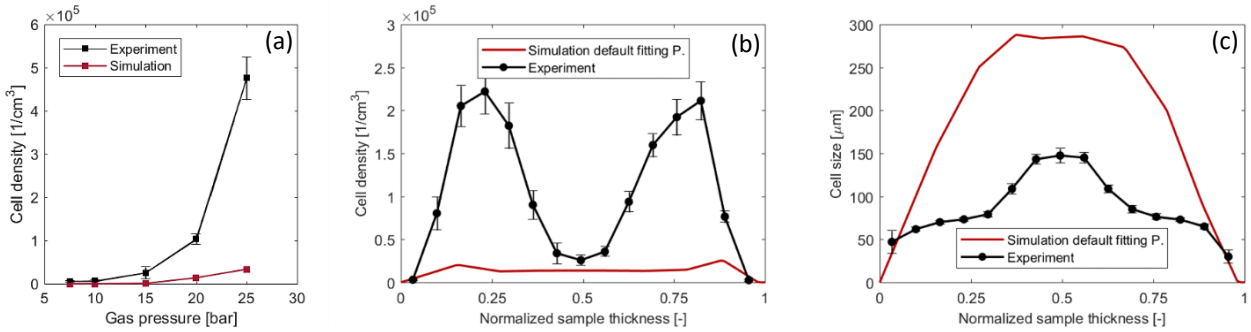

Figure 4.6. Comparison experimental and simulation data at plate location 2. Simulations were performed with default FP. (a) Comparison for available pressure range in Ku-Fizz™, (b)-(c) Through-thickness information at 20 bar.

Table 4.5. Experiment and simulation data in plate location 2 for 20 bar. Simulations were performed with default FP. Red indicates an unacceptable error between experiment and simulation of >30%.

Experiment			Simulation		Percentage Error [%]	
N_2 P [bar]	CD [1/cm³]	CS [μm]	CD [1/cm³]	CS [μm]	CD	CS
7.5	$4.2 \times 10^3 \pm 7.5 \times 10^2$	182.9 ± 22.3	0	0	200	200
10	$5.6 \times 10^3 \pm 1.0 \times 10^3$	162.4 ± 16.0	5.3×10^{-2}	367.8	165	78
15	$2.1 \times 10^4 \pm 3.8 \times 10^3$	142.5 ± 17.7	8.6×10^2	368.3	184	88
20	$1.1 \times 10^5 \pm 1.5 \times 10^4$	87.6 ± 4.9	1.4×10^4	195.7	154	73
25	$5.0 \times 10^5 \pm 4.1 \times 10^4$	55.7 ± 3.3	3.4×10^4	158.2	175	96

FPs after optimization are shown in Table 4.6. Compared to values for homogenous nucleation of neat PP, the pre-exponential factor f_0 increased while F decreased. Compared to default FP our value for f_0 is bigger, thus favoring nucleation. F is smaller, therefore also increasing the nucleation rate.

Table 4.6. FP after parameter optimization. Values are compared to literature.

Material/Gas system	f_0	F	Reference
30 wt% GF PP/N_2	5.6135 x 10^{-24}	9 x 10^{-4}	This work
PP/CO_2	3.5 x 10^{-25}	1.4 x 10^{-2}	[89]
2.5 % nano-$CaC0_3$ iPP/CO_2	3.5 x 10^{-21}	1.3 x 10^{-2}	[98]
5 % nano-$CaC0_3$ iPP/CO_2	3.5 x 10^{-19}	1.1 x 10^{-2}	[98]

Figure 4.7 and Table 4.7 show the comparison of experimental MS and simulation results obtained after parameter optimization. A good agreement was found for sample location 1 and 2, however simulation diverts considerably from the experimental data at the end of the cavity. Moldex3D assumes a perfectly vented cavity which is an ideal case and does not align with the experimental set-up.

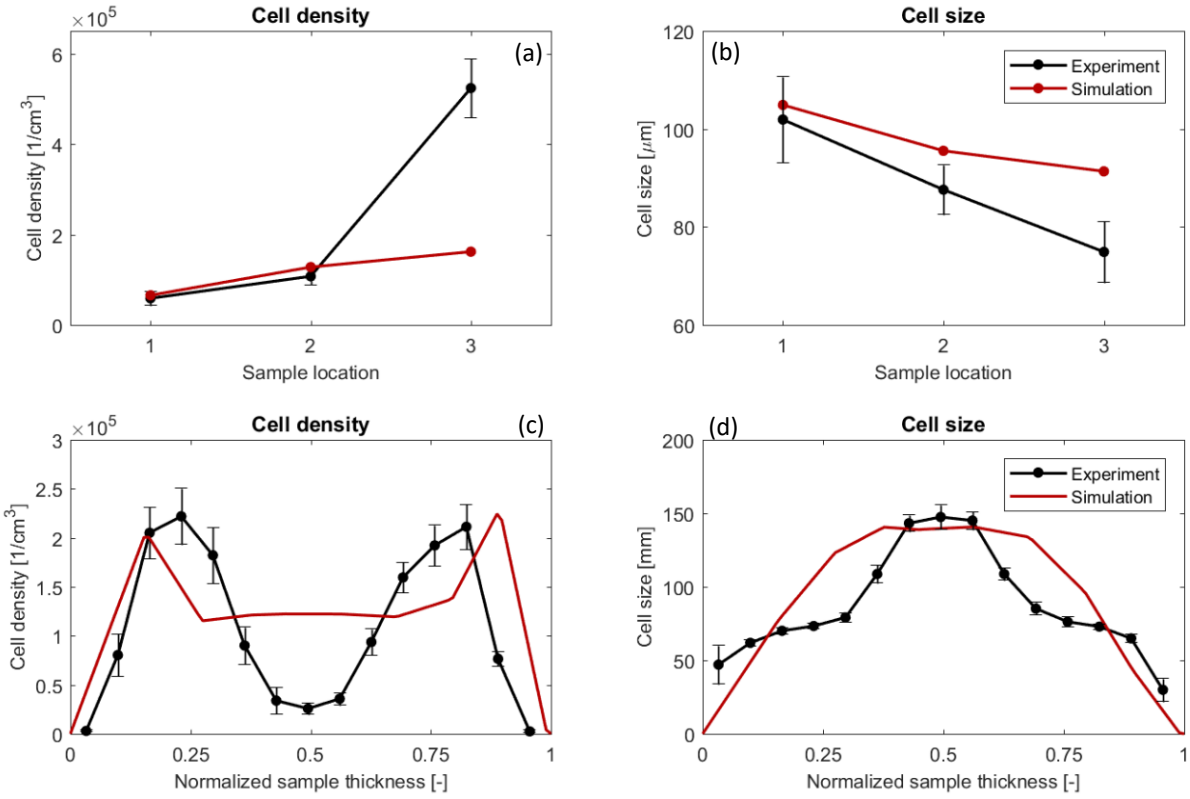

Figure 4.7. Comparison between experimental and predicted global CD and CS values along the plate length at 20 bar gas pressure. (c)-(d) Thickness-wise cell information in plate location 2 at 20 bar.

Table 4.7. Experiment and simulation for plate. Simulations were performed with optimized FP and at 20 bar. Green indicates a percentage difference of ≤ 20% (ideal), yellow an error between 20% and 30% (acceptable), and red an unacceptable error of >30%.

Location	Experiment		Simulation		Percentage Error [%]	
	CD [1/cm³]	CS [µm]	CD [1/cm³]	CS [µm]	CD	CS
1	$5.8 \times 10^4 \pm 1.5 \times 10^4$	101.9 ± 8.8	5.6×10^4	104.9	4	3
2	$1.1 \times 10^5 \pm 1.5 \times 10^4$	87.6 ± 4.9	1.3×10^5	95.6	17	9
3	$5.2 \times 10^5 \pm 7.9 \times 10^4$	74.9 ±6.2	1.6×10^5	91.4	106	20

CD was overpredicted in the center of part, as cell merging is not accounted for in Moldex3D. This physical behavior is present in all MIM technologies, however, is more pronounced in Ku-Fizz™ due to the generally increased CS when compared to MuCell. To study the importance of having accurate though-thickness predictions, its effect on flexural properties was studies. Thickness-wise FO, FC, and cell information (mean bubble radius, cell aspect ratio and void volume fraction) were divided into 15 ROIs across the sample thickness (Figure 4.8, top left). A global FL values was used. For global information each ROI had identical cell data and varying fiber data (Figure 4.8, top right). The procedure outlined in chapter 2 was employed to obtain the flexural modulus of the beam.

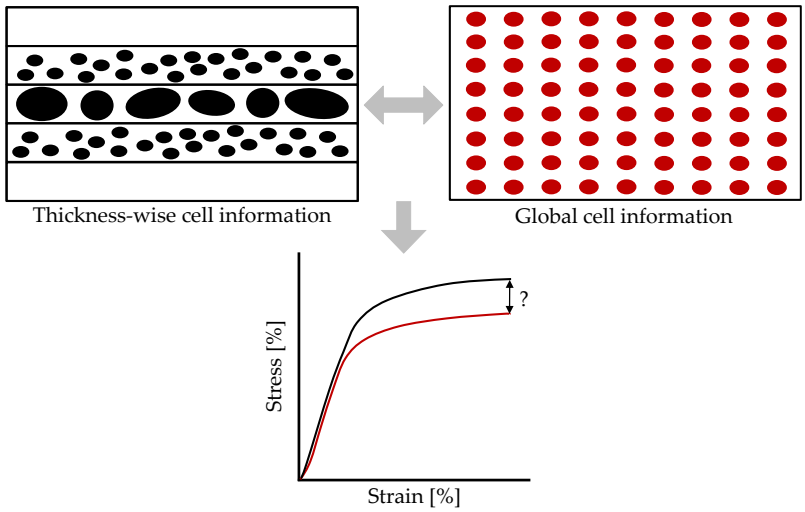

Figure 4.8. Procedure to determine the importance to accurately predict through-thickness information in Moldex3D. Beam is modeled with thickness-wise fiber/cell information and with global data.

Simulations with global cell data showed weaker shells, thus, the beam deforms more and exhibits a lower flexural modulus (Table 4.8). ROI 1 & 15 are mostly comprised by a solid skin and a small "cell strip". Assigning global cell data will increase the occurrence and size of bubbles, thus weakening the outer layer.

An increased modulus was recorded in the center of the plate as global CS and void volume fraction will underestimate the real CS and CD in the core. Small differences in modulus can be seen in Figure 4.9 and Table 4.8. Therefore, predicted global cell values in Moldex3D are sufficient when modeling flexural properties if experiment and simulation only deviate by 17% for CD and 9% for CS. For larger deviations this analysis needs to be repeated.

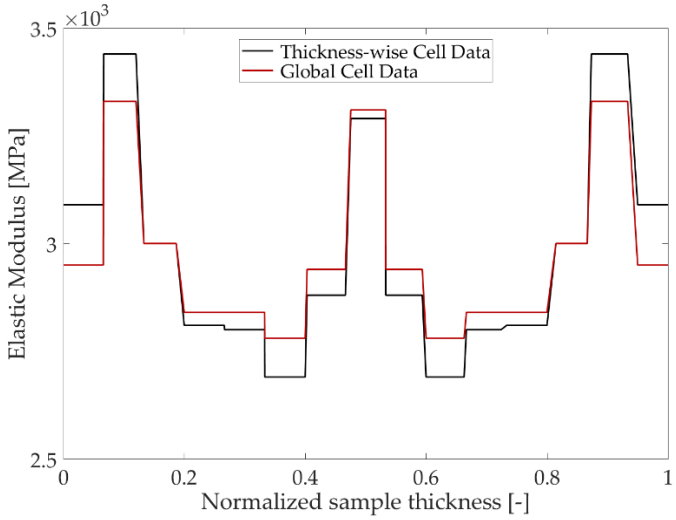

Figure 4.9. Equivalent elastic modulus for thickness-wise and global cell data.

Table 4.8. Comparison in total displacement and flexural modulus for a composite beam employing global and thickness-wise cell data. A vertical center load of 200 N/m was applied.

Parameter	Global	Thickness-wise
Total displacement [μm]	88.50	87.96
Flexural Modulus [GPa]	1.32	1.33

To confirm or refute the optimized FP's ability to correctly predict the foam MS seen in Ku-Fizz™, cross validations with new processing conditions were conducted (Table 4.9).

Table 4.9. Processing conditions for cross validations trials at 20 bar.

Settings	Reference	High
Melt Temperature [°C]	230	260
Mold Temperature [°C]	50	70

An example for a through-thickness fit between simulation and experiment is shown in Figure 4.10. Global CD and CS values are presented in Table 4.10-11. While the found set of FP achieves a good prediction (<20% error) for some cases, in most cases the simulation results are on average more than 65% off when compared to experimental data.

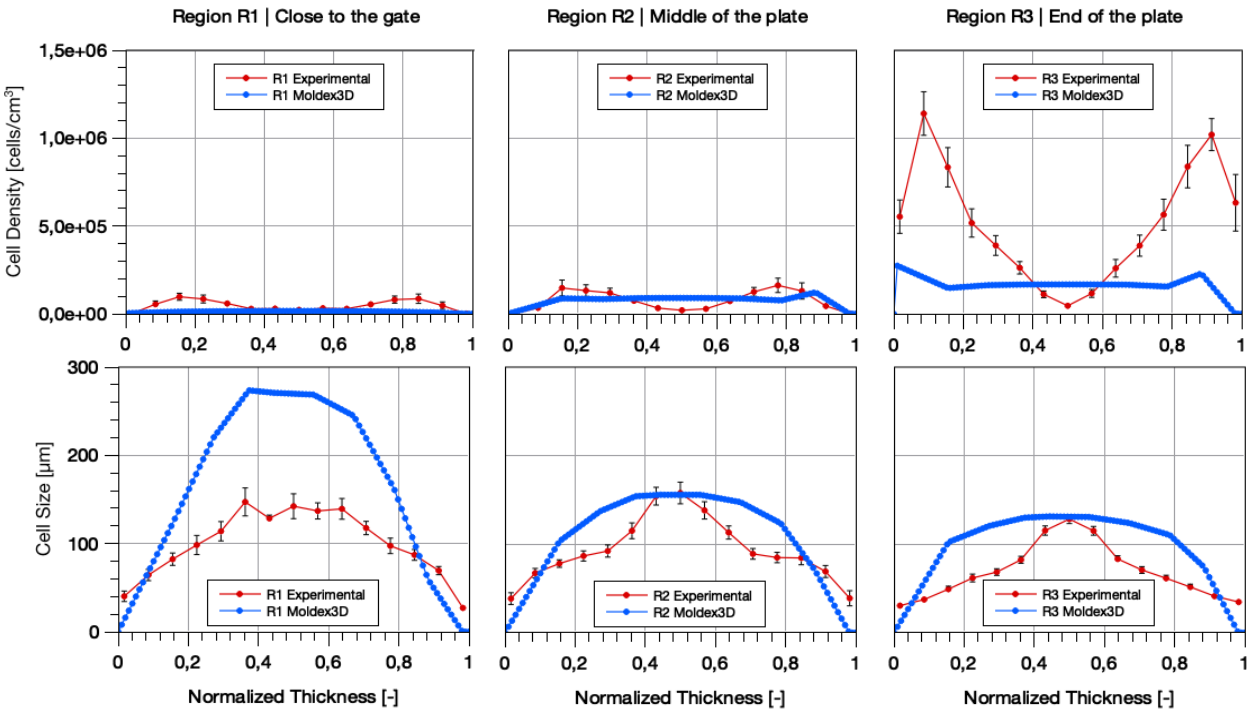

Figure 4.10. Evaluation of found FP. Plates were molded at 20 bar with an elevated melt temperature of 260 °C.

Table 4.10. Experiment and simulation of plate foamed at 20 bar and increased melt temperature of 260 °C. Green indicates a percentage difference of ≤ 20% (ideal), yellow an error between 20% and 30% (acceptable), and red an unacceptable error of >30%.

	Experiment		Simulation		Percentage Error [%]	
Location	CD [1/cm³]	CS [µm]	CD [1/cm³]	CS [µm]	CD	CS
1	$4.7 \times 10^4 \pm 1.6 \times 10^4$	99.5 ± 9.4	1.2×10^4	172.6	119	54
2	$7.5 \times 10^4 \pm 2.6 \times 10^4$	93.8 ± 7.8	7.8×10^4	112.3	4	18
3	$5.1 \times 10^5 \pm 8.6 \times 10^4$	68.8 ± 3.7	1.6×10^5	99.3	104	36

Table 4.11. Experiment and simulation of plate foamed at 20 bar and increased mold temperature of 70 °C. Green indicates a percentage difference of ≤ 20% (ideal), yellow an error between 20% and 30% (acceptable), and red an unacceptable error of >30%.

	Experiment		Simulation		Percentage Error [%]	
Location	CD [1/cm³]	CS [µm]	CD [1/cm³]	CS [µm]	CD	CS
1	$4.6 \times 10^4 \pm 1.3 \times 10^4$	100.9 ± 11.1	3.0×10^4	134.2	42	28
2	$1.1 \times 10^5 \pm 2.7 \times 10^4$	88.1 ± 6.7	1.6×10^5	89.0	37	1
3	$5.0 \times 10^5 \pm 9.1 \times 10^4$	67.3 ± 5.5	1.2×10^5	102.9	122	42

These results underline that changing the FP alone is not sufficient to correctly capture the behavior of the Ku-Fizz™ process. This is because, the Ku-Fizz™ experimental data is out of the simulation window which was initially determined for MuCell (Figure 4.11). As the FP were obtained outside the window, the FP cannot predict the foaming behavior in the Ku-Fizz™ processing window. Therefore, the simulation window needs to be expanded.

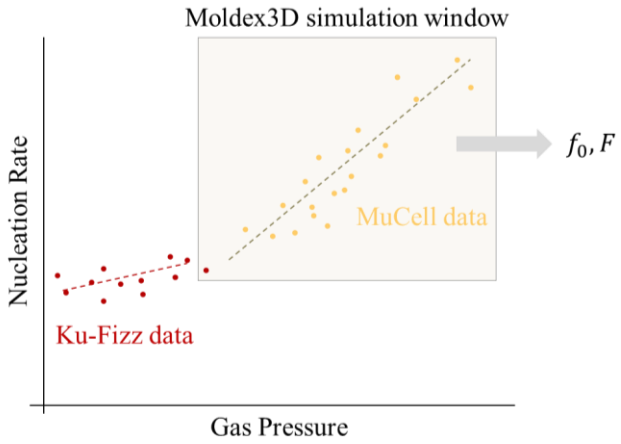

Figure 4.11. Moldex3D MuCell simulation window and Ku-Fizz™ processing window.

4.4 Determination of pressure correction factor

4.4.1 Screw Pull Out Experiments

Ku-Fizz™ and Profoam introduce gas alongside pellets by employing a modified pressurized hopper unit. This leads to a particular mechanism of gas introduction into the melt. As pellets start melting, gas pockets are formed. As the melt continues moving forward in the plasticating unit, these pockets are sheared and compressed until the gas is completely dissolved into the melt. To be able to simulate Ku-Fizz™/Profoam with Moldex3D's MIM tool, the gas weight/volume fraction or gas saturation pressure must be determined first. This is difficult since there is no direct measurement of the gas weight/volume percentage introduced in the melt.

To better understand the gas mixing mechanism, screw pull out experiments were performed using a single screw extruder. SABIC STAMAX 30YH611 extrusion grade glass fiber PP was dried at 100 °C for 2 hours before processing. The Extrudex Kunstoffmaschinen single-screw extruder was used to plasticize the material. Extruder barrel temperatures from hopper to die were set to 200, 210, 220, 230, 230, and 230 °C, the screw speed was 34.7 RPM. Under steady-state operating conditions, the extruder was abruptly stopped,

and both the barrel and the screw were left to cool. Afterwards, the screw was pulled, and the solidified helical polymer was unwound.

X-ray μ-CT (Metrotom 800, Carl Zeiss AG) was used to obtain the interior material structure in the channels. Throughout the reported studies, the voltage was set to 80 kV, the current to 110 μA, the integration time to 1000 ms, the gain to 8, the number of projections to 2200, the spot size to 20 μm, and the voxel size was 40 μm. The μCT data set was processed with ImageJ to obtain slices of the cross-sections of the channels. Full screw pictures and Image Pro were used to verify the presence of enclosed pockets and their location along the screw (Figure 4.12).

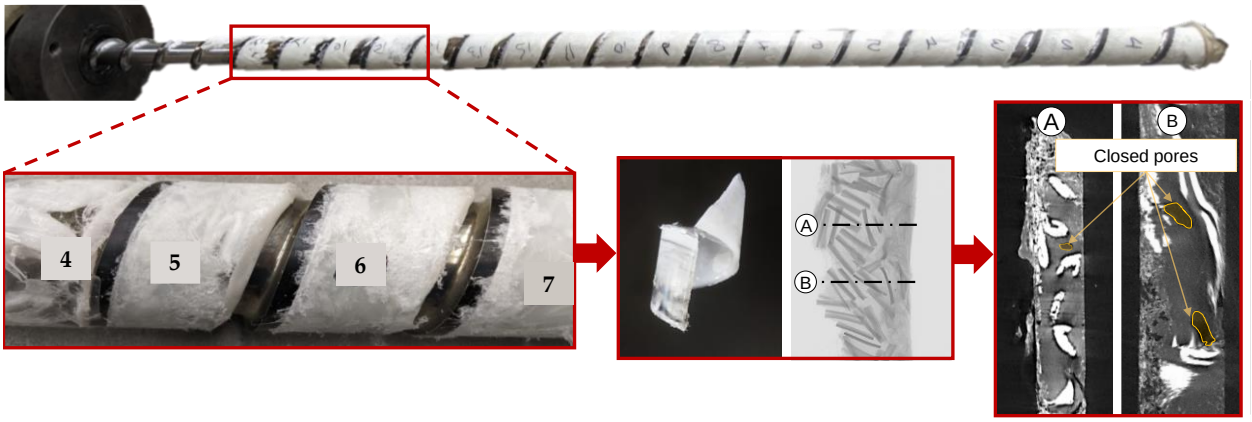

Figure 4.12. Procedure of gas content determination under dynamic conditions. Pitch 4-7 are shown which represent 1/5 and 1/3 of the screw, respectively.

Plastication process parameters such as temperature profile, back pressure and plasticating speed will impact gas mixing mechanism and pocket formation. For this experiment (single screw extrusion), the enclosed pocket formation occurred between 1/5 and 1/3 of the screw length. The gas pressure inside these pockets right after their formation can be used along with the temperature profile, to determine the amount of gas introduced into the melt. Unfortunately, there is no direct way of measuring this quantity in Ku-Fizz™/Profoam. However, a first approach to estimate this pressure is by using a linear interpolation between the gas pressure in the hopper and the nozzle pressure measured during plastication.

4.4.2 Box Injection Molding Trials

To determine the relationship between the measured pressures (P_{hopper} and P_{nozzle}) and the saturation pressure (P^*_{sat}), IM trials were performed with a box geometry and SABIC STAMAX™ 30 wt% long glass

fiber-reinforced PP. Demo boxes (195 mm x 150 mm x 1.65-3.3 mm) were molded by SABIC, Netherlands, on a 150-ton Arburg 520H 1500-800-50 IM machine equipped with a Profoam hopper unit. Profoam and Ku-Fizz^{TM} units are based on the same technology, and only show interior design variations, thus, a similar MS is expected. The processing settings are summarized in Table 4.12. The cavity was filled from a single gate as shown in Figure 4.13. Applications of sensors enabled P_{nozzle} readings during the IM cycle.

Table 4.12. Processing conditions for the foam injection molding trials.

Settings	Foamed
Gas pressure [bar]	20, 25, 35,40
Melt Temperature [°C]	240
Mold Temperature [°C]	40
Back Pressure [bar]	40
Injection Pressure [bar]	~558
Injection Time [s]	1.39
Holding Pressure [bar]	25
Holding Time [s]	0

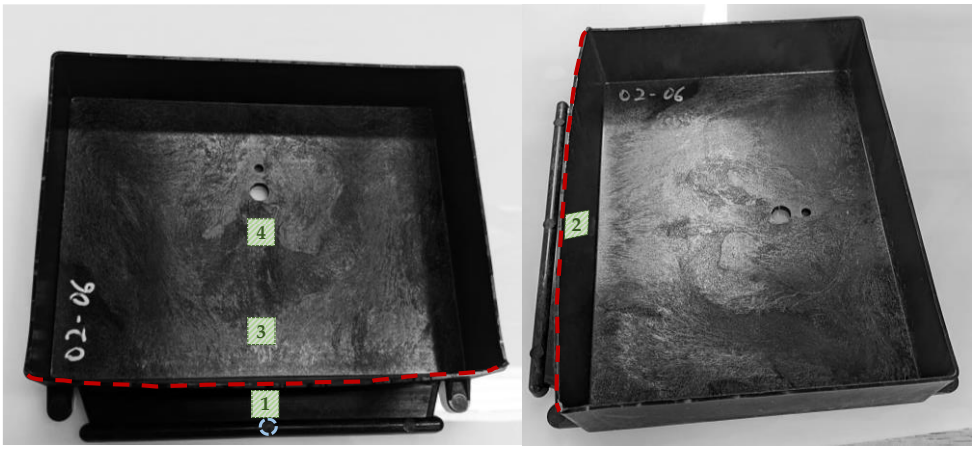

Figure 4.13. Molded demo box. Blue circles indicate injection point, dashed red line shows a bent side to ease in part extraction.

4.4.3 Pressure correction and parameter determination

Moldex3D simulation parameters for box foaming trials are shown in Table 4.12 and Table 4.13. The presence of fibers leads to a heterogenous nucleation, thus default FP (f_0, F) for homogeneous nucleation cannot be used. Similar to Taki, 2008, f_0 and F were varied to fit the number density of bubbles to experimental data by a trial-and-error method [89]. The optimal values of FP parameters are shown in Table ***4.13***. All simulations employed the modified Han and Yoo model for the mass-transfer equation. The box

geometry was meshed with a fit boundary mesh and a solver accuracy of 1 was applied. For foaming simulations, a solid part weight of 172.12 g was used.

Table 4.13. Input parameters for Moldex3D R22 injection foaming simulations.

Input Parameter	Value
Nitrogen Gas Pressure [bar]	20, 25, 30, 35
Nitrogen Molecular Weight M_w [g/mol]	28
Gas Diffusion Coefficient [cm²/s]	8.07 x 10^{-5}
Gas Solubility k_H [mol/(cm³Pa)]	3 x 10^{-11}
Surface Tension γ [N/cm]	1.78 x 10^{-4}
Threshold of Bubble $J(t)$ [1/cm³s]	0.1
Default f_0 [-]	8.30 x 10^{-25}
Default F [-]	1.1 x 10^{-3}
Optimized f_0 [-]	5.8 x 10^{-25}
Optimized F [-]	1.5 x 10^{-3}

Figure 4.14 shows the averaged P_{nozzle} as a function of time for compact and foamed boxes. The spike in pressure indicates melt injection into the cavity, followed by a lower pressure plateau corresponding to the pressure during plastication. Little variations in the pressure profile can be seen for the different gas pressures.

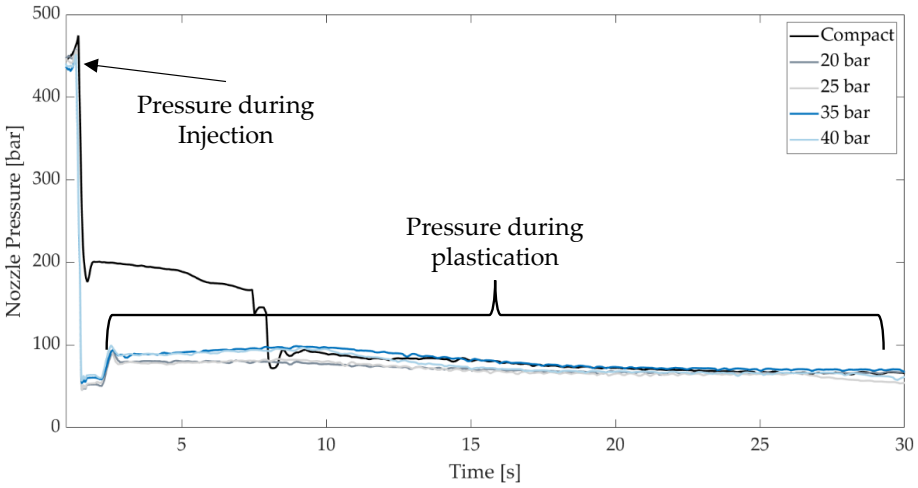

Figure 4.14. Averaged pressure readings in the nozzle. Highlighted region represents pressure P_{nozzle} readings used for P^*_{sat} calculation.

To estimate P^*_{sat} for the simulation input, a liner interpolation between the pressure at the hopper and the pressure at the nozzle will be used. From the screw pull out experiments it was determined that gas is

enclosed by the melt between 1/5 and 1/3 of the screw length. Since melting occurs much faster for an IM screw, the value of 1/5 of the screw length was used for the interpolation as illustrated in Figure 4.15.

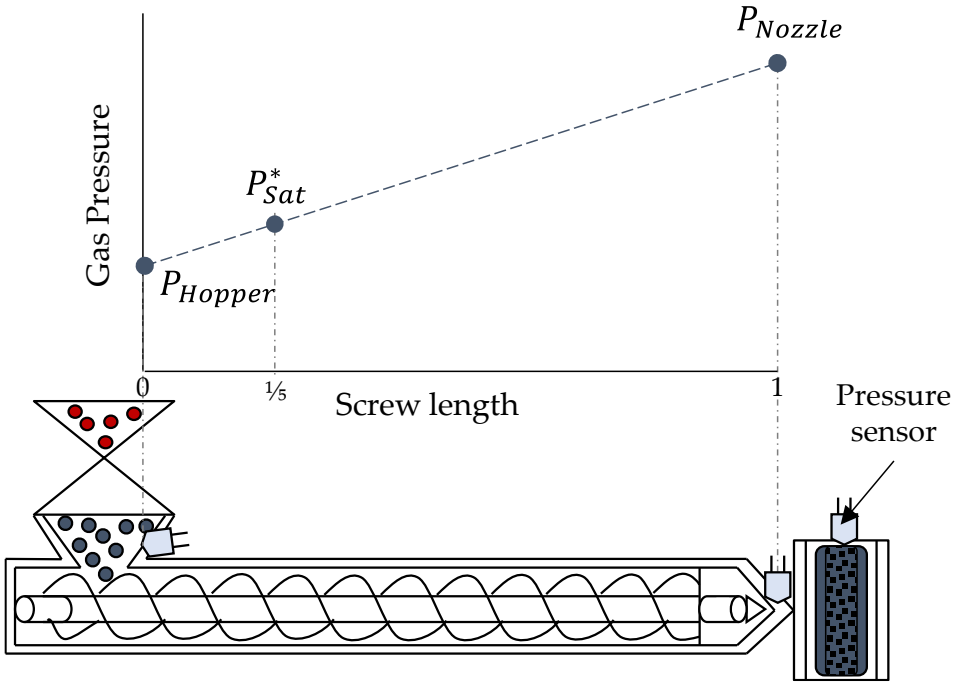

Figure 4.15. Gas saturation pressure determination.

From this linear interpolation, the following expression for P^*_{sat} was deduced:

$$P^*_{sat} = \frac{1}{5}\left(P_{Nozzle} - P_{Hopper}\right) + P_{Hopper} \tag{31}$$

Gas pressures used for the molding trials and calculated values of P^*_{sat} can be found in Table 4.14. Since similar nozzle pressure readings were obtained for the different hopper pressures, an average value of 67.34 bar was used for the calculation.

Table 4.14. Averaged nozzle pressure and calculated gas saturation pressures for simulation input.

P_{hopper} [bar]	P_{nozzle} [bar]	P^*_{sat} [bar]
20	67.34	29.4
25		33.4
35		41.4
40		45.4

To evaluate this approach, Moldex3D simulations were performed with obtained P^*_{sat} values. Predictions were compared with experimental data. Microscopic images of foam MS for the boxes are shown in Figure ***4.16***. Generally, CD increases with flow length; except for location 2 (box wall) which shows a decreased CD.

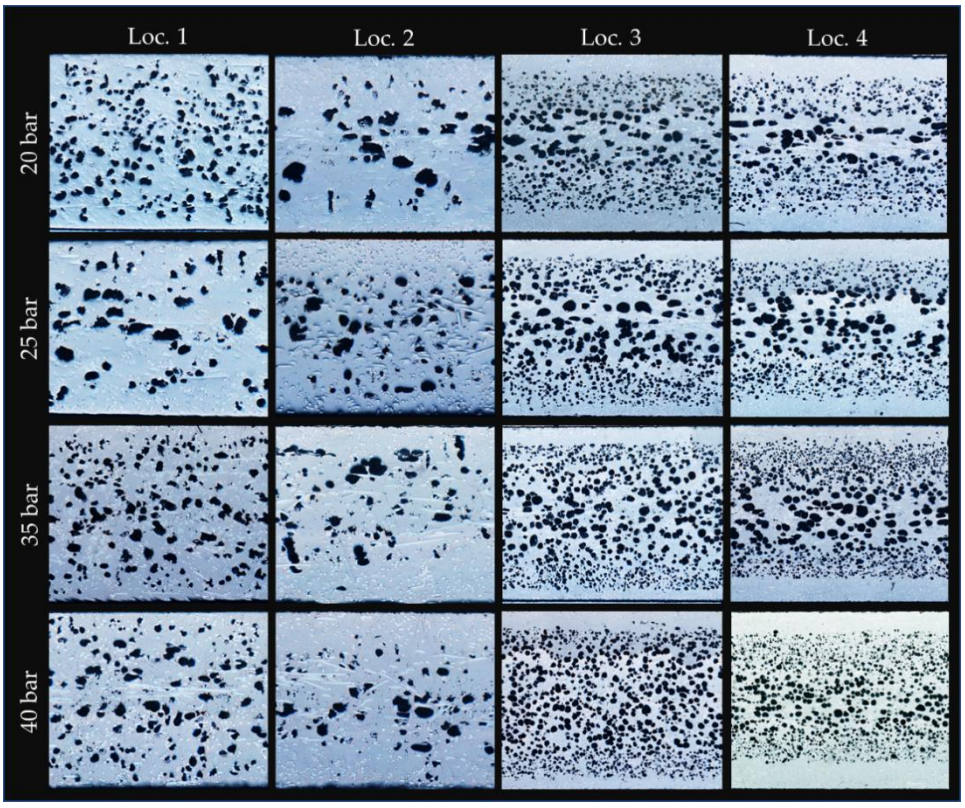

Figure 4.16. Microscopic images of cross-sections of microcellular injection molded boxes.

Global experimental and predicted CD and CS values are presented in Table 4.15-4.18. Green indicates a percentage difference of ≤ 20% (ideal), yellow an error between 20-30% (acceptable), and red an unacceptable error of >30%.

Table 4.15. Experiment and simulation data along the box. Simulations were performed at P^*_{sat}= 29.4 bar.

	Experiment		Simulation		Error [%]	
Location	**CD [1/ccm]**	**CS [µm]**	**CD [1/ccm]**	**CS [µm]**	**CD**	**CS**
1	$2.1 \times 10^5 \pm 8.7 \times 10^4$	77.7 ± 7.4	1.8×10^5	62.6	15.4	21.5
2	$7.5 \times 10^4 \pm 2.6 \times 10^4$	64.6 ± 8.3	8.3×10^4	60.1	10.1	7.2
3	$2.1 \times 10^5 \pm 5.2 \times 10^4$	75.1 ± 3.6	2.2×10^5	62.5	4.7	18.3
4	$3.5 \times 10^5 \pm 3.7 \times 10^4$	65.0 ± 4.0	2.7×10^5	55.4	25.8	16.0

Table 4.16. Experiment and simulation data along the box. Simulations were performed at P^*_{sat}= 33.4 bar.

	Experiment		Simulation		Error [%]	
Location	**CD [1/ccm]**	**CS [µm]**	**CD [1/ccm]**	**CS [µm]**	**CD**	**CS**
1	$7.0 \times 10^4 \pm 1.5 \times 10^4$	61.4 ± 4.3	7.9×10^4	71.4	12.7	15.1
2	$8.3 \times 10^4 \pm 8.5 \times 10^3$	57.1 ± 4.2	1.7×10^5	49.1	66.5	15.0
3	$3.3 \times 10^5 \pm 1.2 \times 10^4$	65.8 ± 9.7	3.2×10^5	66.6	3.1	1.2
4	$5.5 \times 10^5 \pm 3.9 \times 10^4$	66.5 ± 1.7	4.8×10^5	68.2	13.6	8.7

Table 4.17. Experiment and simulation data along the box. Simulations were performed at P^*_{sat}= 41.4 bar.

	Experiment		Simulation		Error [%]	
Location	**CD [1/ccm]**	**CS [µm]**	**CD [1/ccm]**	**CS [µm]**	**CD**	**CS**
1	$1.1 \times 10^5 \pm 3.8 \times 10^4$	65.1 ± 4.9	1.4×10^5	82.76	24.0	23.9
2	$7.0 \times 10^4 \pm 1.8 \times 10^4$	43.5 ± 2.9	1.0×10^5	47.12	35.3	7.9
3	$4.2 \times 10^5 \pm 8.0 \times 10^4$	68.4 ± 4.4	3.4×10^5	64.90	21.1	5.3
4	$8.6 \times 10^5 \pm 2.2 \times 10^4$	60.4 ± 4.1	8.1×10^5	65.15	6.0	7.5

Table 4.18. Experiment and simulation data along the box. Simulations were performed at P^*_{sat}= 45.4 bar.

	Experiment		Simulation		Error [%]	
Location	**CD [1/ccm]**	**CS [µm]**	**CD [1/ccm]**	**CS [µm]**	**CD**	**CS**
1	$1.8 \times 10^5 \pm 5.1 \times 10^4$	51.3 ± 4.3	1.8×10^5	57.6	0.0	11.6
2	$7.0 \times 10^4 \pm 1.3 \times 10^4$	51.4 ± 9.9	6.3×10^4	47.7	10.5	7.5
3	$6.5 \times 10^5 \pm 4.1 \times 10^4$	58.0 ± 1.6	5.4×10^5	63.7	18.5	9.4
4	$1.1 \times 10^6 \pm 1.8 \times 10^5$	50.9 ± 1.4	8.6×10^5	49.7	24.5	2.5

A good agreement between simulation and experiment was found as average deviations for CD and CS are less than 18.2 % and 11.2 %, respectively. This indicates that the P^*_{sat} calculation approach and the obtained values of f_0 & F can be used to predict the Ku-Fizz™/Profoam MIM process in Moldex3D.

4.5 Industrial Case Study - Internal Door Panel Molded with Ku-Fizz™

4.5.1 Door Panel molding trials

To validate Step 2, P^*_{sat} parameters were applied to SCANIA AB R-Series truck door panels (Figure 4.17). Manufacturing of these parts has been presented in the previous chapter. Panels were molded at 20 bar, thus the P^*_{sat} value was set to 29.4 bar.

Figure 4.17. (a) SCANIA AB R-Series truck door, (b) Metal door frame, (c) CAD drawing highlighting the composite door module in purple.

4.5.2 Simulation Set-Up

Moldex3D parameters for door panel simulations are shown in Table 4.13. All simulations employed the modified Han and Yoo model for the mass-transfer equation. The geometry was meshed with a fit boundary mesh and a solver accuracy of 1 was employed. For foaming simulations, a solid part weight of 932.6 g was used.

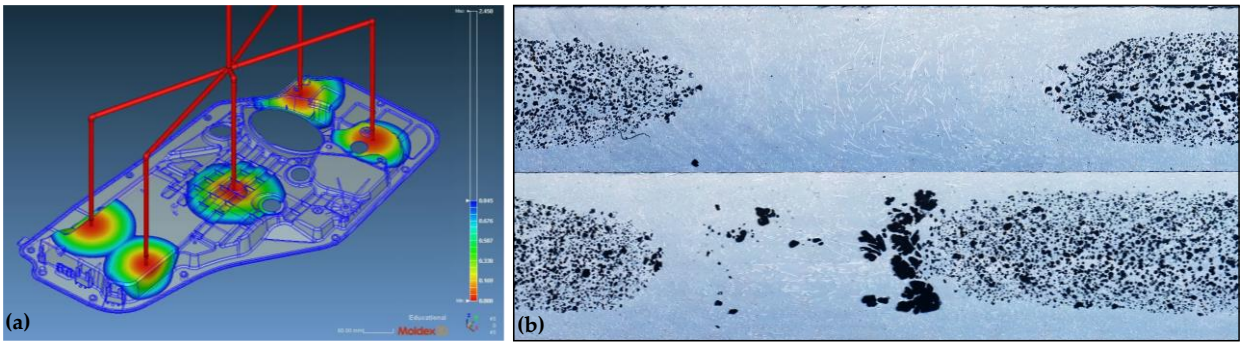

Figure 4.18. (a) Mold filling simulation. (b) Micrographs of weld lines.

4.5.3 Simulation Evaluation

Table 4.19 shows the comparison between experimental and predicted values. A poor prediction was found for location 2 (weldline). Weld lines are complex to model since their particular behavior is not described by the constitutive equations used by the simulation tools. For example, Figure 4.18b shows uneven cell formation in one case and nonexistent foam MS in another case.

Table 4.19. Experiment and simulation data for foamed door panels. Simulations were performed at P^*_{sat}= 29.4 bar. Green indicates a percentage difference of ≤ 20% (ideal), yellow an error between 20% and 30% (acceptable), and red an unacceptable error of >30%.

	Experiment		Simulation		Error [%]	
Location	**CD [1/ccm]**	**CS [μm]**	**CD [1/ccm]**	**CS [μm]**	**CD**	**CS**
1 Weld	$1.8 \times 10^2 \pm 6.8 \times 10^1$	42.6 ± 5.9	7.6×10^2	2.1	123.4	181.2
2 Gate	$1.1 \times 10^5 \pm 2.2 \times 10^4$	64.7 ± 7.2	1.4×10^5	48.8	24.0	28.0
3	$7.0 \times 10^4 \pm 1.5 \times 10^4$	57.3 ± 5.8	7.8×10^4	44.8	10.8	24.5
4	$3.8 \times 10^4 \pm 7.1 \times 10^3$	78.5 ± 8.7	3.4×10^4	58.0	11.1	30.0
5	$5.6 \times 10^4 \pm 9.0 \times 10^3$	67.4 ± 8.2	5.6×10^4	68.2	0.2	1.2
6	$5.5 \times 10^4 \pm 1.3 \times 10^4$	76.2 ± 8.5	4.5×10^4	50.8	20.0	40.0

Foam MS predictions were improved by introducing a pressure scaling factor. Yet, this is a first approach and there is potential for improvement. For example, accounting for the P^*_{sat} dependence on screw speed during plastication as this parameter will affect the abscissa in the pressure interpolation. Nevertheless, the authors are confident this approach can be used to model different part geometries molded under different processing conditions with Ku-Fizz™.

4.6 Conclusions

In this work, the fundamental gas dynamics of the foaming technology Ku-Fizz™ was studied and a simulation tool for foam microstructure prediction was evaluated.

It was found that gas diffusion into solid state pellets, in the hopper or early on in the barrel, is negligible when compared with gas mixing during and after melting. Therefore, the mixing of gas during melting was the focus of this research.

Current simulation models fall short when predicting the foam MS obtained with Ku-Fizz™. The error in CD between simulation and experiments was above 150%. Default FP in the simulation tools are produced for the MuCell technology; and this process operates at a much higher gas pressure range. This causes the main source of error in the simulation results.

Thus, an exploration study to understand the underlying mechanism of gas addition in the Ku-Fizz™ process was conducted via screw pull out experiments. Gas initially occupies the space between pellets, then is slowly trapped in enclosed pockets as the pellets melt and move along the screw. The formation of these sealed pockets occurred early in the melting zone. Based on these results, a pressure scaling equation was proposed, and the updated model was optimized with a set of foam MS measurements obtained from IM trials. In these trials, demo boxes were molded using Profoam (similar technology as Ku-Fizz™). The

foam MS models were updated using the scaled gas pressure, and the FP were optimized to bring the average error between simulation and experiment below 30%.

An automotive door panel manufactured with Ku-Fizz™ MIM and PPGF was used as a case study to test the performance of the updated foaming model. Results showed an average error of 13% for CD and 25% for CS (not including the weld line).

5 Summary

5.1 Recommendations for Future Work

Future work should involve testing of the assembled door module with the inserted Ku-Fizz™ foamed door panel. Analyses should include a modal analysis on a shaker rig, determination of bending stiffness and strength, testing of fatigue durability, crash worthiness, and NVH testing. In parallel, FEA analysis (ABAQUS, LS-DYNA, ANSYS) need to be conducted to verify if the assembly meets design requirements.

It is recommended to study Ku-Fizz™ with other polymers, such as biopolymers (PLA) for an improved economic, environmental, and ecological impact. The process should also be tested with natural reinforcing fillers such as flax, sisal, kenaf, hemp, bamboo, and cellulose fibers to determine the differences in the seen foam and fiber MS.

As numerical simulations are a standard task in early design phases of automotive components, there is need for reliable and accurate commercial software tools. In the case of Ku-Fizz™, further validation and enhancements of the proposed model are required. We propose to assess the model for other complex mold structures and processing conditions using Ku-Fizz™ or ProFoam. In addition, future work should add upon current mathematical models in Moldex3D to capture the complex mechanisms found in the MIM process. This work showed cell merging and irregular bubble shapes for all foamed parts. These behaviors are currently not implemented in the computation simulation package leading to less accurate predictions.

5.2 Publications

The following list details publications related to the research conducted at the Polymer Engineering Center.

5.2.1 Peer reviewed Journal Publications

- Simon, S.A.; Bechara Senior, A.; Osswald, T. Experimental Validation of a Direct Fiber Model for Orientation Prediction. J. Compos. Sci. 2020, 4, 59. https://doi.org/10.3390/jcs4020059
- Simon, S.A.; Hain, J.; Osswald, T. Effect of gas pressure on the microstructure of parts foamed with the novel microcellular injection molding technology Ku-Fizz™. SPE Polymers. 2021, 2, 311-324. https://doi.org/10.1002/pls2.10044
- Simon, S.A.; Hain, J.; Sracic, M.W.; Tewani, H.R.; Prabhakar, P.; Osswald, T. Mechanical response of fiber-filled automotive body panels manufactured with the Ku-Fizz™ microcellular injection molding process. Polymers, 2022 [under review]

5.2.2 Conference Proceedings

- Goris, S.; Simon, S.A.; Montoya, C.; Bechara, A.; Brands, D.; Angel, Y.; Candal, M.V.; Osswald, T.A. Experimental Study on Fiber Attrition of Long Glass Fiber-Reinforced Thermoplastics under Controlled Conditions in a Couette Flow. ANTEC, 2017, Anaheim, CA. https://par.nsf.gov/servlets/purl/10063467
- Simon, S.A.; Bechara Senior, A.; Osswald, T. Direct fiber model validation: Orientation evolution in simple shear flow. ACCE - Automotive Composites Conference & Exhibition, 2019, Novi, MI. https://www.researchgate.net/publication/354254540_DIRECT_FIBER_MODEL_VALIDATION_ORIENTATION_EVOLUTION_IN_SIMPLE_SHEAR_FLOW
- Simon, S.A.; Hain, J.; Osswald, T.A. Modeling and simulation of an alternative microcellular injection molding process Ku-Fizz™. PPS-37 – International Conference of the Polymer Processing Society, 2019, Fukuoka, Japan. Will be published in AIP proceedings for PPS-37.

5.2.3 Conference Posters

- Simon, S.A.; Goris, S.; Bechara, A.; Osswald, T.A. Study on fiber attrition of long glass fiber-reinforced thermoplastics under controlled conditions in a Couette flow. ACCE - Automotive Composites Conference & Exhibition, 2016, Novi, MI
- Simon, S.A.; Bechara, A.; Osswald, T.A. Predicting fiber orientation evolution using particle-level simulation: an experimental validation. ACCE - Automotive Composites Conference & Exhibition, 2018, Novi, MI
- Simon, S.A.; Hain, J.; Osswald, T.A. Novel microcellular injection molding technology Ku-Fizz™ – effect of gas pressure on the fiber microstructure and flexural properties. ACCE - Automotive Composites Conference & Exhibition, 2021, Novi, MI

6. Bibliography

[1] EPA, "U.S. Greenhouse Gas Emissions and Sinks 1990-2019," 2021.

[2] J. Kühlwein, "Driving resistances of light-duty vehicles in Europe: Present situation, trends, and scenarios for 2025," *International Council on Clean Transportation Europe*, 2016.

[3] J. Hain, "Physcial foaming of injection molded thermoplastic parts with IQ-Foam," 2019.

[4] R. Byron Bird and F. Curtiss, "Fascinating polymeric liquids," *Physica Todays*, vol. 37, 1984.

[5] L. Cheah, "Cars on a diet: the material and energy impacts of passenger vehicle weight reduction in the US," Massachusetts Institute of Technology, 2010.

[6] United States Department of Energy, "Lightweight materials for cars and trucks." https://www.energy.gov/eere/vehicles/lightweight-materials-cars-and-trucks#:~:text=A%2010%25%20reduction%20in%20vehicle,%25-8%25%20fuel%20economy%20improvement.&text=Research%20and%20development%20into%20lightweight,maximizing%20their%20fuel%20economy%20benefits. (accessed Oct. 02, 2022).

[7] W. J. Joost, "Reducing vehicle weight and improving U.S. energy efficiency using integrated computational materials engineering," *JOM*, vol. 64, no. 9, pp. 1032–1038, 2012.

[8] EA, "CO2 & Road Transport - Position & messages of the European Aluminium Industry," 2007.

[9] "Automotive Lightweight Material Market by Material (Metal, Composite, Plastic, Elastomer), Application & Component (Frame, Engine, Exhaust, Transmission, Closure, Interior), Vehicle Type (ICE, Electric & Hybrid), Region-Global Forecast to 2025," 2020.

[10] J. L. Thomason, "The influence of fibre length and concentration on the properties of glass fibre reinforced polypropylene. 6. the properties of injection moulded long fibre PP at high fibre content," *Compos Part A Appl Sci Manuf*, vol. 36, no. 7, pp. 995–1003, doi: 10.1016/j.compositesa.2004.11.004, 2005.

[11] B. Nghiep Nguyen and V. Kunc, "An elastic-plastic damage model for long-fiber thermoplastics," *International Journal of Damage Mechanics*, vol. 19, no. 6, pp. 691–725, doi: 10.1177/1056789509338319, 2010.

[12] G. Zhang and M. R. Thompson, "Reduced fibre breakage in a glass-fibre reinforced thermoplastic through foaming," *Compos Sci Technol*, vol. 65, no. 14, pp. 2240–2249, doi: 10.1016/j.compscitech.2005.04.050, 2005.

[13] R. Jain and L. Lee, *Fiber Reinforced Polymer (FRP), Composites for Infrastructure Applications*. Springer Netherlands, 2012.

[14] J. Xu, *Microcellular injection molding*. John Wiley and Sons Inc., 2010.

[15] M. Kutz, *Applied plastics engineering handbook - processing, materials, and applications*, 2nd editio. Elsevier Inc. doi: https://doi.org/10.1016/C2014-0-04118-4, 2017.

[16] K. S. Lee, P. J. Jeong, H. Lee, S. J. Lee, and S. W. Cha, "Conceptual design of microcellular plastics bumper parts using axiomatic approach," *Polymer Plastics Technology and Engineering*, vol. 48, pp. 1101–1106, 2009.

[17] H. Heitkamp and M. Betsche, "Renaissance of foam processes - Injection molding - More than just foam bubbles," in *Kunststoffe international*, 2014.

[18] "VW opts for MuCell to lighten dashboard weight," *Plastics Today* [Online]. Available: https://www.plasticstoday.com/vw-opts-mucell-lighten-dashboard-weight. 2012.

[19] L. J. Hyde and L. A. Kishbaugh, "The MuCell Injection Molding Process : A Strategic Cost Savings Technology for Electronic Connectors," 2003.

[20] J. Hain, "Physical foaming of injection molded thermoplastic parts with IQ-Foam," 2019.

[21] W. Kienzl, "ENGEL foammelt - (MuCell®) precision lightweight parts made of micro-foam structures," 2022. https://www.engelglobal.com/en/ca/blog/lighter-dimensionally-stable-components-thanks-to-plastic-foaming.html (accessed Oct. 03, 2022).

[22] L. Kishbaugh, "Five cases where microcellular foaming paid of," 2012. https://www.ptonline.com/articles/five-cases-where-microcellular-foaming-paid-off (accessed Oct. 03, 2022).

[23] J. E. Martini, "The production and analysis of microcellular foam," Massachusetts Institute of Technology, 1981.

[24] N. P. Suh, *Innovation in polymer processing*, Chapter 3. New York: Hanser/Gardner Publications, 1996.

[25] S. Han, P. Kennedy, R. Zheng, J. Xu, and L. Kishbaugh, "Numerical analysis of microcellular injection molding," *Cellular Plastics*, vol. 39, pp. 475–485, 2003.

[26] A. Handschke and J. Mitzler, "Injection molding - physical foaming made very easy," in *Kunststoffe international*, Carl-Hanser Verlag, 2012.

[27] J. G. Monterde, "Characterization of microcellular plastics for weight reduction in automotive interior parts," PhD thesis, Polytechnic University of Catalonia, 2016.

[28] J. G. Monterde, J. Hain, M. Sanchez-Soto, and M. L. Maspoch, "Microcellular injection molding: A comparison between MuCell process and the novel micro-foaming technology IQ Foam," *J Mater Process Technol*, vol. 268, pp. 162–170, 2019.

[29] C. Hopmann, N. Lammert, and Y. Zhang, "Improvement of foamed part surface quality with variothermal temperature control and analysis of the mechanical properties," *Journal of Cellular Plastics*, vol. 55, no. 5, pp. 507–522, doi: 10.1177/0021955X19841050, 2019.

[30] Z. Wentao, Y. Jian, and H. Jiasong, "Research progresses in preparation of microcellular polymers by supercritical fluid technique," *Chinese polymer bulletin*, vol. 3, pp. 1–10, 2009.

[31] H. Guanghong and W. Yue, "Microcellular Foam Injection Molding Process," *Some Critical Issues for Injection Molding*, doi: 10.5772/34513. 2012.

[32] S. Habibi-Naini, "Neue Verfahren fuer das Thermoplasrschaumspritzgiessen," PhD thesis, RWTH Aachen, 2004.

[33] C. B. Park and N. P. Suh, "Filamentary extrusion of microcellular polymers using a rapid decompressive element," *Polym Eng Sci*, vol. 36, no. 1, pp. 34–48, 1996.

[34] J. Xu, "Effect of Injection Molding Process Parameters on the Morphology and Quality of Microcellular Foams," in *SPE ANTEC*, pp. 2770–2774, 2006.

[35] J. Xu and P. J. Pierick, "Injection Molding Technology," vol. 5, pp. 152–159, 2001.

[36] K. Okamoto, *Microcellular Processing*. Cincinnati: Hanser/Gardner Publications, 2003.

[37] N. P. Suh, "Impact of microcellular plastics on industrial practice and academic research," in *Macromolecules Symposium 201*, pp. 187–202, 2003.

[38] V. Altstädt and A. Mantey, *Thermoplast-Schaumspritzgießen / Thermoplystic foam injection molding*. Carl-Hanser Verlag GmbH & CO. KG., 2010.

[39] J. K. Lee, S. X. Yao, G. Li, M. B. G. Jun, and P. C. Lee, "Measurement Methods for Solubility and Diffusivity of Gases and Supercritical Fluids in Polymers and Its Applications," *Polymer Reviews*, doi: 10.1080/15583724.2017.1329209, 2017.

[40] L. Wang, X. Huang, and D. Wang, "Solubility and diffusion coefficient of supercritical CO2 in polystyrene dynamic melt," *E-Polymers*, vol. 20, no. 1, pp. 659–672, doi: 10.1515/epoly-2020-0062, 2020.

[41] Y. Sato, K. Fujiwara, T. Takikawa, Sumarno, S. Takishima, and H. Masuoka, "Solubilities and diffusion coefficients of carbon dioxide and nitrogen in polypropylene, high-density polyethylene, and polystyrene under high pressures and temperatures," *Fluid Phase Equilib*, vol. 162, no. 1–2, pp. 261–276, doi: 10.1016/S0378-3812(99)00217-4, 1999.

[42] Throne, *Thermoplastic foams*. Sherwood Publishers, 1996.

[43] G. Li, F. Gunkel, J. Wang, C. B. Park, and V. Altstädt, "Solubility measurements of N2 and CO2 in polypropylene and ethene/octene copolymer," *J Appl Polym Sci*, vol. 103, no. 5, pp. 2945–2953, doi: 10.1002/app.25163, 2007.

[44] J. L. Throne, *Thermoplastic foam extrusion*. Cincinnati: Carl-Hanser Verlag, Hanser Garnder, 2004.

[45] Y. Yang, A. K. Narayanan Nair, and S. Sun, "Adsorption and diffusion of methane and carbon dioxide in amorphous regions of crosslinked polyethylene: A molecular simulation study," *Ind Eng Chem Res*, vol. 124, no. 7, pp. 1301–1310, 2019.

[46] Y. Yang, A. K. Narayanan Nair, and S. Sun, "Adsorption and Diffusion of Methane and Carbon Dioxide in Amorphous Regions of Cross-Linked Polyethylene: A Molecular Simulation Study," *Ind Eng Chem Res*, vol. 58, no. 19, pp. 8426–8436, doi: 10.1021/acs.iecr.9b00690, 2019.

[47] Y. Sato and T. Takikawa, "Solubility and diffusion coefficient of carbon dioxide in biodegradable polymers," *Ind Eng Chem Res*, vol. 39, pp. 4813–4819, 2000.

[48] Y. Sato, T. Takikawa, S. Takishima, and H. Masuoka, "Solubilities and diffusion coefficients of carbon dioxide in poly(vinyl acetate) and polystyrene," *Journal of Supercritical Fluids*, vol. 19, no. 2, pp. 187–198, 2001.

[49] Y. Sato, T. Takikawa, M. Yamane, S. Takishima, and H. Masuoka, "Solubility of carbon dioxide in PPO and PPO/PS blends," *Fluid Phase Equilib*, vol. 194, no. 5, pp. 847–858, 2002.

[50] E. Aionicesei, M. Škerget, and Ž. Knez, "Measurement of CO2 solubiblity and diffusivity in poly(L-lactide) and poly(L-lactide-co-glycolide) by magnetic suspension balance," *Journal of Supercritical Fluids*, vol. 47, no. 2, pp. 296–301, 2008.

[51] E. Aionicesei, M. Škerget, and Ž. Knez, "Measurement and modeling of the CO2 solubility in poly(ethylene glycol) of different molecular weights.," *J Chem Eng Data*, vol. 53, no. 1, pp. 185–188, 2007.

[52] G. Li, J. Wang, C. B. Park, and R. Simha, "Measurement of gas solubility in linear/branched PP melts," *J Polym Sci B Polym Phys*, vol. 45, pp. 2497–2508, doi: 10.1002/polb.21229, 2007.

[53] M.-L. Wang, R.-Y. Chang, and C.-H. Hsu, *Molding Simulation: Theory and Practice*. Carl-Hanser Verlag, 2018.

[54] J. H. Han and C. D. Han, "Bubble nucleation in polymeric liquids. Part 2: Theoretical considerations," *J Polym Sci B Polym Phys*, vol. 28, pp. 743–761, 1990.

[55] J. H. Saunders, *Fundamentals of foam formation*, Hanser Pub. New York, 1991.

[56] V. Altstädt, A. Mantey, and A. Cramer, *Thermoplast-Schaumspritzgiessen*. Hanser, 2011.

[57] R. Cole, "Boiling nucleation," *Adv Heat Transf*, vol. 10, pp. 85–166, 1974.

[58] A. W. Hodgson, "Homogneous nucleation," *Adv Colloid Interface Sci*, vol. 21, pp. 303–327, 1984.

[59] P. Pichler, "Modeling and simulation of microcellular foams," Johannes Kepler Universität Linz, 2016.

[60] J. R. Youn and N. P. Suh, "Processing of microcellular polyester composites," *Polym Compos*, vol. 6, no. 3, pp. 175–180, doi: 10.1002/pc.750060308, 1985.

[61] J. S. Colton and N. P. Suh, "The nucleation of microcellular thermoplastic foam with additives: Part 1: Theoretical considerations," *Polym Eng Sci*, vol. 27, no. 7, pp. 485–492, 1987.

[62] J. Tatibouet, R. Gendron, A. Hamel, and A. Sahnoune, "Effect of different nucleating agents on the degassing conditions as measured by ultrasonic sensors," *Journal of Cellular Plastics*, vol. 38, pp. 203–218, 2002.

[63] D. Sykutera, P. Czyżewski, and P. Szewczykowski, "The microcellular structure of injection molded thick-walled parts as observed by in-line monitoring," *Materials*, vol. 13, pp. 1–22, doi: 10.3390/ma13235464, 2020.

[64] S. N. Leung, C. B. Park, and H. Li, "Effects of nucleating agents shapes and interfacial properties on cell nucleation," *Journal of Cellular Plastics*, vol. 46, pp. 441–460, doi: 10.1177/0021955X10369418, 2010.

[65] J. Wang, "Rheology of foaming polymers and its influence on microcellular processing ," University of Toronto, Toronto, 2009. Available: http://support.moldex3d.com/r15/en/solutionadd-ons_mucell_reference_mathematicalmodelsandassumptions.html. Accessed: Oct. 04, 2022. [Online].

[66] K. Taki, K. Tabata, S. I. Kihara, and M. Ohshima, "Bubble coalescence in foaming process of polymers," *Polym Eng Sci*, pp. 680–690, 2006.

[67] H. P. Heim, *Specialized injection molding techniques*. Elsevier, 2016.

[68] J. R. Anderson, S. W. Cha, D. E. Laing, D. E. Pierick, and J. E. Stevenson, "Injection molding of microcellular material," EP0952908, 1998

[69] D. E. Pierick, J. R. Anderson, S. W. Cha, L. Chen, D. E. Laing, and J. E. Stevenson, "Injection molding of polymeric material," US6884823, 1999

[70] J. E. Martine-Vvedensky, N. P. Suh, and F. A. Waldman, "Microcellular closed cell foams and their method of manufacture," US Patent No. 4,473,665, 1985

[71] J. H. Schut, "Competition bubbles up again in physical foam molding," *SPE Plastics Engineering - Plastics Engineering Blog*, 2016.

[72] Wittmann-Battenfeld, "CELLMOULD - Foam injection molding for light-weight parts." https://www.wittmann-group.com/sites/default/files/2020-10/cellmould-en_2019-04_web.pdf (accessed Oct. 03, 2021).

[73] H. Eckardt, "Physical Foaming with Cellmould®. Properties and Possibilities," *Cellular Polymers*, vol. 33, no. 5, pp. 259–286, doi: 10.1177/026248931403300503, 2014.

[74] S. Habibi-Naini and C. Schlummer, "A new and flexible process for thermoplastic foams," in *SPE ANTEC*, vol. 2, pp. 54–58, 2005.

[75] W. Michaeli, O. Pfannschmidt, and S. Habibi-Naini, "Spritzgießen mikrozellulärer Schäume," *Kunststoffe*, vol. 92, pp. 56–60, 2002.

[76] W. Michaeli and H. Schumacher, "A new approach for the injection of physcial blowing agents in foam extrusion," in *SPE ANTEC*, pp. 3043–3047, 2007.

[77] "Das SmartFoam-Verfahren der Stieler Kunststoff Service GmbH," [Online]. Available: https://www.youtube.com/watch?v=BJegcRQZ2fs&t=7s, 2010.

[78] W. Michaeli, C. Hopman, and D. Obeloer, "Examination on the influencing factors on the foamability using the profoam process," in *SPE ANTEC*, pp. 1–11. doi: PENG-11-2010-0059.R1, 2011.

[79] W. Michaeli, T. Krumpholz, and D. Obeloer, "Profoam - a new foaming process of injection molding," 2008.

[80] D. Obeloer, "Thermoplastic foam moulding with combined supply of polymer pellets and gas," PhD thesis, RWTH Aachen University, 2012.

[81] C. Schütz, J. Hain, and M. Müller, "System zum schleusen, dosieren und spritzgießen von material," DE102014212048A1, 2014

[82] M. Knights, "Electric machines and new processes catch fire," *Plastics Technology*, 2002. https://www.ptonline.com/articles/electric-machines-and-new-processes-catch-fire (accessed Oct. 03, 2021).

[83] X. Sun and L. S. Turng, "A novel foaming injection molding process using gas-laden pellets," 2012.

[84] X. Sun, H. Kharbas, and L. S. Turng, "Enhancing cell nucleation for a novel microcellular injection molding process using gas-laden-pellets," in *SPE ANTEC*, pp. 1540–1545, 2014.

[85] J. Peng, X. Sun, Y. Srithep, X. F. Peng, and L. S. Turng, "Vapor-foamed injection molding of polycarbonate using sodium chloride and active carbon as nucleating agents," in *SPE ANTEC*, pp. 1726–1731, 2014.

[86] J. Lee, L. S. Turng, E. Dougherty, and P. Gorton, "Novel foam injection molding technology using carbon dioxide-laden pellets," *Polym Eng Sci*, vol. 51, no. 11, pp. 2295–2303, doi: 10.1002/pen.22004, 2011.

[87] J. J. Feng and C. A. Bertelo, "Prediction of bubble growth and size distribution in polymer foaming based on a new heterogeneous nucleation model," *J Rheol (N Y N Y)*, vol. 48, pp. 439–462, doi: 10.1122/1.1645518, 2004.

[88] M. A. Shafi, J. G. Lee, and R. W. Flumerfelt, "Prediction of cellular structure in free expansion polymer foam processing," *Polym Eng Sci*, vol. 36, no. 14, pp. 1950–1959, doi: 10.1002/pen.10591, 1996.

[89] K. Taki, "Experimental and numerical studies on the effects of pressure release rate on number density of bubbles and bubble growth in a polymeric foaming process," *Chem Eng Sci*, vol. 63, no. 14, pp. 3643–3653, doi: 10.1016/j.ces.2008.04.037, 2008.

[90] M. Amon and C. D. Denson, "A study of the dynamics of foam growth: analysis of the growth of closely spaced spherical bubbles," *Polym Eng Sci*, vol. 24, pp. 1026–1034, 1984.

[91] E. J. Barlow and W. E. Langlois, "Diffusion of Gas from a Liquid into an Expanding Bubble," *IBM J Res Dev*, pp. 329–337, doi: 10.1147/rd.63.0329, 1962.

[92] R. D. Patel, "Bubble growth in a viscous Newtonian liquid," *Chem Eng Sci*, vol. 35, no. 11, pp. 2352–2356, doi: 10.1016/0009-2509(80)87016-3, 1980.

[93] C. D. Han and H. J. Yoo, "Studies on structural foam processing. IV. Bubble growth during mold filling," *Polym Eng Sci*, vol. 21, no. 9, pp. 518–533, doi: 10.1002/pen.760210903, 1981.

[94] P. Payvar, "Mass transfer-controlled bubble growth during rapid decompression of a liquid," *Int J Heat Mass Transf*, vol. 30, no. 4, pp. 699–706, doi: 10.1016/0017-9310(87)90200-6, 1987.

[95] N. S. Ramesh, D. H. Rasmussen, and G. A. Campbell, "The heterogenous nucleation of microcellular foams assisted by the survival of microvoids in polymers containing low glass-transition particles. 1. Mathematical-modeling and numerical-simulation," *Polym Eng Sci*, vol. 34, pp. 1685–1697, 1994.

[96] N. S. Ramesh, S. T. Lee, and C. B. Park, *Foam Extrusion: Principles and Practice*, 2nd editio. CRC Press, 2014.

[97] D. Tammaro *et al.*, "Validated modeling of bubble growth, impingement and retraction to predict cell-opening in thermoplastic foaming," *Chemical Engineering Journal*, vol. 287, pp. 492–502, doi: 10.1016/j.cej.2015.11.034, 2016.

[98] Z. Xi, J. Chen, T. Liu, L. Zhao, and L. S. Turng, "Experiment and simulation of foaming injection molding of polypropylene/nano-calcium carbonate composites by supercritical carbon dioxide," *Chin J Chem Eng*, vol. 24, no. 1, pp. 180–189, doi: 10.1016/j.cjche.2015.11.016, 2016.

[99] M. Tromm, "Controlling cellular structure in thermoplastic foam injection molding – influence of processing and mold technologies," University of Kassel, 2020.

[100] Moldex3D, "Mathematical Models and Assumptions." (accessed Oct. 10, 2022).

[101] T. Y. Shiu, Y. J. Chang, C. T. Huang, D. Hsu, and R. Y. Chang, "Dynamic behavior and experimental validation of cell nucleation and growing mechanism in microcellular injection molding process," in *SPE ANTEC*, p. 6, 2012.

[102] J. Stange, "Influence of rheological properties on the foaming behavior of polypropylenes of different molecular structure," PhD thesis, University of Erlangen-Nürnberg, 2006.

[103] M. Blander, "Bubble nucleation in liquids," *Advances in Co*, vol. 10, pp. 1–32, 1979.

[104] M. Blander and J. Katz, "Bubble nucleation in liquids," *American Institute of Chemical Engineers*, vol. 21, pp. 833–848, doi: 10.1016/0001-8686(79)87002-5, 1975.

[105] K. I. Y. Kim, S. L. Kang, and H. Y. Kwak, "Bubble nucleation and growth in polymer solutions," *Polym Eng Sci*, vol. 44, no. 10, pp. 1890–1899, doi: 10.1002/pen.20191, 2004.

[106] D. Kashchiev, "Multicomponent nucleation: Thermodynamically consistent description of the nucleation work," *Journal of Chemical Physics*, vol. 120, no. 8, pp. 3749–3758, doi: 10.1063/1.1643711, 2004.

[107] G. J. Monterde, M. Sánchez-Soto, and M. L. Maspoch, "Microcellular PP/GF composites: Morphological, mechanical and fracture characterization," *Compos Part A Appl Sci Manuf*, vol. 104, 2018.

[108] J. Gómez-Monterde *et al.*, "Morphology and Mechanical Characterization of ABS Foamed by Microcellular Injection Molding," *Procedia Eng*, vol. 132, pp. 15–22, doi: 10.1016/j.proeng.2015.12.462, 2015.

[109] H. Y. Mi, X. Jing, J. Peng, L. S. Turng, and X. F. Peng, "Influence and prediction of processing parameters on the properties of microcellular injection molded thermoplastic polyurethane based on an orthogonal array test," *Journal of Cellular Plastics*, vol. 49, no. 5, pp. 439–458, doi: 10.1177/0021955X13488399, 2013.

[110] B. Bujanic, M. Sercer, and M. Rujnic-Sokele, "Comparison of Moldex3D and Moldflow injection moulding simulations," 2006.

[111] M. Heneczkowski and G. Kopeć, "Simulations of thick-wall injection molding part using the Moldex3D program," *Mechanik*, vol. 92, no. 4, pp. 226–228, doi: 10.17814/mechanik.2019.4.30, 2019.

[112] T. Y. Shiu, Y. J. Chang, C. T. Huang, C. H. Hsu, R. Y. Chang, and S. S. Hwang, "Foaming morphology of microcellular injection molded parts - simulation and experimental characterization," 2013.

[113] S.-Y. Fu, X. Hu, and C.-Y. Yue, "Effects of fiber length and orientation distributions on the mechanical properties of short-fiber-reinforced polymers: A Review," 1999.

[114] V. Kumar and N. P. Suh, "A process for making microcellular thermoplastic parts," *Polym Eng Sci*, vol. 30, no. 20, pp. 1323–1329, doi: 10.1002/pen.760302010, 1990.

[115] D. F. Baldwin, C. B. Park, N. P. Suh, and N. P. Suh, "A microcellular processing study of poly(ethylene terephthalate) in the amorphous and semicrystalline states. Par 1: Microcell nucleation," *Polym Eng Sci*, vol. 36, pp. 1437–1445, 1996.

[116] S. Goris, "Characterization of the Process-Induced Fiber Configuration of Long Glass Fiber-Reinforced Thermoplastics," PhD Thesis, University of Wisconsin-Madison, 2017.

[117] S. Goris and T. A. Osswald, "Process-induced fiber matrix separation in long fiber-reinforced thermoplastics," *Compos Part A Appl Sci Manuf*, vol. 105, pp. 321–333, doi: 10.1016/j.compositesa.2017.11.024, 2018.

[118] M. Krause, J. M. Hausherr, B. Burgeth, C. Herrmann, and W. Krenkel, "Determination of the fibre orientation in composites using the structure tensor and local X-ray transform," *J Mater Sci*, vol. 45, no. 4, pp. 888–896, doi: 10.1007/s10853-009-4016-4, 2010.

[119] B. N. Nguyen *et al.*, "Fiber length and orientation in long-fiber injection-molded thermoplastics - Part I: Modeling of microstructure and elastic properties," *J Compos Mater*, vol. 42, no. 10, pp. 1003–1029, doi: 10.1177/0021998308088606, 2008.

[120] S. Goris, T. Back, A. Yanev, D. Brands, D. Drummer, and T. A. Osswald, "A novel fiber length measurement technique for discontinuous fiber-reinforced composites: A comparative study with existing methods," *Polym Compos*, vol. 39, no. 11, pp. 4058–4070, doi: 10.1002/pc.24466, 2018.

[121] V. Kunc, B. Frame, B. N. Nguyen, C. L. T. Iii, and G. Velez-Garcia, "Fiber length distribution measurement for long glass and carbon fiber reinforced injection molded thermoplastics," in *SPE Automotive Composites Conference and Exhibition*, p. 11, 2007.

[122] C. Kastner, G. Steinbichler, S. Kahlen, and M. Jerabek, "Influence of process parameters on mechanical properties of physically foamed , fiber reinforced polypropylene parts," *J Appl Polym Sci*, pp. 1–11, doi: 10.1002/app.47275, 2019.

[123] N. Ykhlef and E. Lafranche, "Injection-moulding of nitrogen-foamed bio-based microcellular poly(butylene succinate): Processing conditions/foam structure/flexural properties relationship," *Polymers from Renewable Resources*, vol. 11, no. 1–2, pp. 30–46, doi: 10.1177/2041247920952653, 2020.

[124] J. Lee, L. S. Turng, E. Dougherty, and P. Gorton, "A novel method for improving the surface quality of microcellular injection molded parts," *Polymer (Guildf)*, vol. 52, no. 6, pp. 1436–1446, doi: 10.1016/j.polymer.2011.01.026, 2011.

[125] L. Zhang, G. Zhao, and G. Wang, "Formation mechanism of porous structure in plastic parts injected by microcellular injection molding technology with variable mold temperature," *Appl Therm Eng*, vol. 114, pp. 484–497, doi: 10.1016/j.applthermaleng.2016.11.180, 2017.

[126] P. Xie *et al.*, "Effect of mold opening process on microporous structure and properties of microcellular polylactide-polylactide nanocomposites," *Polymers (Basel)*, vol. 18, no. 554, pp. 1–11, doi: 10.3390/polym10050554, 2018.

[127] Z. Xi, X. Sha, T. Liu, and L. Zhao, "Microcellular injection molding of polypropylene and glass fiber composites with supercritical nitrogen," *Journal of Cellular Plastics*, vol. 50, no. 5, pp. 489–505, doi: 10.1177/0021955X14528931, 2014.

[128] A. Ahmadzai, A. H. Behravesh, M. T. Sarabi, and P. Shahi, "Visualization of foaming phenomena in thermoplastic injection molding process," *Journal of Cellular Plastics*, vol. 50, no. 3, pp. 279–300, doi: 10.1177/0021955X14525797, 2014.

[129] H. bin Wu, H. J. Haugen, and E. Wintermantel, "Supercritical CO 2 in injection molding can produce open porous polyurethane scaffolds-a parameter study," *Journal of Cellular Plastics*, vol. 48, no. 2, pp. 141–159, doi: 10.1177/0021955X11432970, 2011.

[130] J. W. S. Lee, J. Wang, J. D. Yoon, and C. B. Park, "Strategies to achieve a uniform cell structure with a high void fraction in advanced structural foam molding," *Ind Eng Chem Res*, vol. 47, no. 23, pp. 9457–9464, doi: 10.1021/ie0707016, 2008.

[131] M. Mahmoodi, A. H. Behravesh, M. S. A. Rezavand, and A. Pashaei, "Visualization of bubble dynamics in foam injection molding," *J Appl Polym Sci*, vol. 116, pp. 3346–3355, 2010.

[132] F. J. Gómez-Gómez, D. Arencón, M. Á. Sánchez-Soto, and A. B. Martínez, "Influence of the injection moulding parameters on the microstructure and thermal properties of microcellular polyethylene terephthalate glycol foams," *Journal of Cellular Plastics*, vol. 49, no. 1, pp. 47–63, doi: 10.1177/0021955X12460044, 2012.

[133] G. Wang, G. Zhao, J. Wang, and L. Zhang, "Research on formation mechanisms and control of external and inner bubble morphology in microcellular injection molding," *Polym Eng Sci*, 2015.

[134] G. Dong, G. Zhao, Y. Guan, S. Li, and X. Wang, "Formation mechanism and structural characteristics of unfoamed skin layer in microcellular injection-molded parts," *Journal of Cellular Plastics*, vol. 52, no. 4, pp. 419–439, doi: 10.1177/0021955X15577149, 2015.

[135] N. Mueller-Fischer, P. Tobler, M. Dressler, P. Fischer, and E. J. Windhab, "Single bubble deformation and breakup in simple shear flow," *Exp Fluids*, vol. 45, 2008.

[136] G. Yilmaz, T. Ellingham, and L. S. Turng, "Improved processability and the processing-structure-properties relationship of ultra-high molecular weight polyethylene via supercritical nitrogen and carbon dioxide in injection molding," *Polymers (Basel)*, vol. 10, no. 36, doi: 10.3390/polym10010036, 2017.

[137] J. H. Phelps, A. I. Abd El-Rahman, V. Kunc, and C. L. Tucker, "A model for fiber length attrition in injection-molded long-fiber composites," *Compos Part A Appl Sci Manuf*, vol. 51, pp. 11–21, 2013.

[138] V. Volpe, S. Lanzillo, G. Affinita, B. Villacci, I. Macchiarolo, and R. Pantani, "Lightweight high-performance polymer composite for automotive applications," *Polymers (Basel)*, vol. 11, no. 326, pp. 1–16, doi: 10.3390/polym11020326, 2019.

[139] S. A. Simon, A. Bechara Senior, and T. Osswald, "Experimental Validation of a Direct Fiber Model for Orientation Prediction," *Journal of Composites Science*, vol. 4, no. 59, doi: 10.3390/jcs4020059, 2020.

[140] G. H. Motlagh, A. N. Hrymak, and M. R. Thompson, "Improved through-plane electrical conductivity in a carbon-filled thermoplastic via foaming," *Polym Eng Sci*, pp. 687–696, 2008.

[141] V. Shaayegan, A. Ameli, S. Wang, and C. B. Park, "Experimental observation and modeling of fiber rotation and translation during foam injection molding of polymer composites," *Compos Part A Appl Sci Manuf*, vol. 88, pp. 67–74, doi: 10.1016/j.compositesa.2016.05.013, 2016.

[142] G. H. Motlagh, A. N. Hrymak, and M. R. Thompson, "Improved through-plane electrical conductivity in a carbon-filled thermoplastic via foaming," *Polym Eng Sci*, pp. 687–696, 2008.

[143] A. Roch, L. Kehret, T. Huber, F. Henning, and P. Elsner, "Investigations on injection molded, glab-fiber reinforced polyamide 6 integral foams using breathing mold technology," in *AIP Conference Proceedings*, vol. 1664. doi: 10.1063/1.4918488, 2015.

[144] Y. A. Orban, D. L. Manea, and C. Aciu, "Study of methods for simulating multiphase construction materials," *Procedia Manuf*, vol. 22, pp. 256–261, doi: 10.1016/j.promfg.2018.03.039, 2018.

[145] T. Mori and T. K., "Average stress in the matrix and average elastic energy of materials with misfitting inclusions," *Acta Metallurgica et Materialia*, vol. 21, pp. 571–574, 1973.

[146] Xstream, "Digimat User's Manual," 2019.

[147] M. R. Barzegari and D. Rodrigue, "The effect of density profile on the flexural properties of structure foams," *Polym Eng Sci*, pp. 1459–1468, 2007.

[148] S. A. Simon, J. Hain, and T. Osswald, "Effect of gas pressure on the microstructure of parts foamed with the novel microcellular injection molding technology Ku-Fizz™," *SPE Polymers*, vol. 2, no. 4, pp. 311–324, doi: 10.1002/pls2.10044, 2021.

[149] P. K. Mallick, "Designing lightweight vehicle body," in *Materials, Design and Manufacturing for Lightweight Vehicles*, Elsevier, pp. 405–432. doi: 10.1016/b978-0-12-818712-8.00010-0, 2021.

[150] A. Reunis, A. Hogg, P. Naughton, T. Dau, N. Schoppmann, and R. Nickel, "Mass ABS development for high quality thin-walled interior door panels for the 1998 VW GOLF," 1999.

[151] S. A. Pradeep, R. K. Iyer, H. Kazan, and S. Pilla, "Automotive Applications of Plastics: Past, Present, and Future," in *Applied Plastics Engineering Handbook: Processing, Materials, and Applications: Second Edition*, Elsevier Inc., pp. 651–673. doi: 10.1016/B978-0-323-39040-8.00031-6, 2017.

[152] A. F. Tencer, R. Kaufman, C. MacK, and C. Mock, "Factors affecting pelvic and thoracic forces in near-side impact crashes: A study of US-NCAP, NASS, and CIREN data," *Accid Anal Prev*, vol. 37, no. 2, pp. 287–293, doi: 10.1016/j.aap.2004.09.005, 2005.

[153] A. Ghadianlou and S. bin Abdullah, "Crashworthiness design of vehicle side door beams under low-speed pole side impacts," *Thin-Walled Structures*, vol. 67, pp. 25–33, doi: 10.1016/j.tws.2013.02.004, 2013.

[154] A. Mohanty and S. Fatima, "An overview of automobile noise and vibration control," *Noise Notes*, vol. 13, no. 1, pp. 43–56, doi: 10.1260/1475-4738.13.1.43, 2014.

[155] M. Shalaby and K. Saitou, "Optimal heat-reversible snap joints for frame-panel assembly in aluminium space frame automotive bodies," *International Journal of Sustainable Manufacturing*, vol. 1, no. 3, pp. 302–317, doi: 10.1504/IJSM.2009.023976, 2009.

[156] F. Chen and D. McKillip, "Measurement and analysis of vibration and deformation using laser metrology for automotive application," in *Proceedings of the Institution of Mechanical Engineers, Part D: Journal of Automobile Engineering*, vol. 221, no. 6, pp. 725–738. doi: 10.1243/09544070JAUTO67, 2007.

[157] J. Pang, *Noise and Vibration Control in Automotive Bodies*. China Machine Press, 2019.

[158] M. Mavrigian, "Noise/vibration/harshness: Chasing the irritant gremlins," 2013. https://www.autoserviceprofessional.com/articles/7364-noise-vibration-harshness-chasing-the-irritant-gremlins (accessed Sep. 25, 2022).

[159] M. Shalaby and K. Saitou, "Optimal heat-reversible snap joints for frame-panel assembly in aluminium space frame automotive bodies," *International Journal of Sustainable Manufacturing*, vol. 1, no. 3, pp. 302–317, doi: 10.1504/IJSM.2009.023976, 2009.

[160] T. Bein, J. Bös, D. Mayer, and T. Melz, "Advanced materials and technologies for reducing noise, vibration and harshness (NVH) in automobiles," in *Advanced Materials in Automotive Engineering*, Elsevier, pp. 254–298. doi: 10.1533/9780857095466.254, 2012.

[161] B. Reff, "Noise and vibration refinement of chassis and suspension," doi: 10.1553/B9781845694975.3.318, 2010.

[162] R. C. Dante, "Noise and vibration," in *Handbook of Friction Materials and their Applications*, Elsevier, pp. 67–77. doi: 10.1016/B978-0-08-100619-1.00005-5, 2016.

[163] MatchID, "Vibration Analysis: High-speed stereo DIC on car door slamming." https://www.matchid.eu/en/applications/vibration-analysis-high-speed-stereo-dic-on-car-door-slamming (accessed Sep. 24, 2022).

[164] ASTM International, "D7136- 15 Standard Test Method for Measuring the Damage Resistance of a Fiber-Reinforced Polymer Matrix Composite to a Drop-Weight Impact Event," doi: 10.1520/D7136, 2015.

[165] M. S. Allen and J. H. Ginsberg, "A global, single-input-multi-output (SIMO) implementation of the algorithm of mode isolation and application to analytical and experimental data," *Mechanical Systems Signal Processing*, vol. 20, no. 5, pp. 1090–1111, 2006.

[166] M. Pastor, M. Binda, and T. Harčarik, "Modal assurance criterion," in *Procedia Engineering*, vol. 48, pp. 543–548. doi: 10.1016/j.proeng.2012.09.551, 2012.

[167] J. Ginsberg, *Mechanical and Structural Vibrations: Theory and Applications*, 1st edition. Wiley, 2001.

[168] A. Bechara, "Modeling fiber damage during processing of long fiber-reinforced thermoplastic composites," University of Wisconsin-Madison, Madison, 2021.

[169] S. T. Kang and J. K. Kim, "Numerical simulation of the variation of fiber orientation distribution during flow molding of ultra high performance cementitious composites (UHPCC)," *Cem Concr Compos*, vol. 34, no. 2, pp. 208–217, doi: 10.1016/j.cemconcomp.2011.09.015, 2012.

[170] M. Besher Baradi, C. Cruz, T. Riedel, and G. Régnier, "Frontal weld lines in injection-molded short fiber-reinforced PBT: Extensive microstructure characterization for mechanical performance evaluation," *Polym Compos*, vol. 40, no. 12, doi: 10.1002/pc.25310ï, 2019.

[171] H. K. Kim, J. S. Sohn, Y. Ryu, S. W. Kim, and S. W. Cha, "Warpage reduction of glass fiber reinforced plastic using microcellular foaming process applied injection molding," *Polymers (Basel)*, vol. 11, no. 2, doi: 10.3390/POLYM11020360, 2019.

[172] H. Yang *et al.*, "Cell morphologies, mechanical properties, and fiber orientation of glass fiber-reinforced polyamide composites: Influence of subcritical gas-laden pellet injection molding foaming technology," *Physics of Fluids*, vol. 34, no. 1, doi: 10.1063/5.0078055, 2022.

[173] J. L. Thomason and M. A. Vlug, "Influence of fibre length and concentration on the properties of glass fibre-reinforced polypropylene: 1. Tensile and flexural modulus," 1996.

[174] X. Wei, H. Zhou, F. Chen, and G. Wang, "Bending flexibility of Moso Bamboo (Phyllostachys Edulis) with functionally graded structure," *Materials*, vol. 12, no. 12, doi: 10.3390/ma12122007, 2019.

[175] B. Brylka, M. Schemmann, J. Wood, and T. Böhlke, "DMA based characterization of stiffness reduction in long fiber reinforced polypropylene," *Polym Test*, vol. 66, pp. 296–302, doi: 10.1016/j.polymertesting.2017.12.025, 2018.

[176] A. G. Castellanos and P. Prabhakar, "Elucidating the mechanisms of damage in foam core sandwich composites under impact loading and low temperatures," *Journal of Sandwich Structures and Materials*, vol. 24, no. 1, pp. 337–359, doi: 10.1177/1099636221993848, 2022.

[177] P. Breunig *et al.*, "Dynamic impact behavior of syntactic foam core sandwich composites," *J Compos Mater*, vol. 54, no. 4, pp. 535–547, doi: 10.1177/0021998319885000, 2020.

[178] M. Naebe, M. M. Abolhasani, H. Khayyam, A. Amini, and B. Fox, "Crack damage in polymers and composites: A review," *Polymer Reviews*, vol. 56, no. 1. Taylor and Francis Inc., pp. 31–69, doi: 10.1080/15583724.2015.1078352, 2016.

[179] L. Zhuang, R. Talreja, and J. Varna, "Transverse crack formation in unidirectional composites by linking of fibre/matrix debond cracks," *Compos Part A Appl Sci Manuf*, vol. 107, pp. 294–303, doi: 10.1016/j.compositesa.2018.01.013, 2018.

[180] C. Makabe, A. Murdani, K. Kuniyoshi, Y. Irei, and A. Saimoto, "Crack-growth arrest by redirecting crack growth by drilling stop holes and inserting pins into them," *Eng Fail Anal*, vol. 16, no. 1, pp. 475–483, doi: 10.1016/j.engfailanal.2008.06.009, 2009.

[181] Z. Wang, B. Tian, R. Boom, and A. J. van der Goot, "Air bubbles in calcium caseinate fibrous material enhances anisotropy," *Food Hydrocoll*, vol. 87, pp. 497–505, doi: 10.1016/j.foodhyd.2018.08.037, 2019.

[182] H. Dahlan, M. Rusli, and M. Bur, "The Reduction of Stress Concentration at a Crack Tip Using Multi Stop-Drilled Hole (MSDH)," *Journal of Ocean, Mechanical and Aerospace-Science and Engineering*, vol. 55, [Online]. Available: www.isomase.org., 2018.

[183] H. K. Kim, J. Kim, D. Kim, Y. Ryu, and S. W. Cha, "Vibration and Sound Response of Glass-Fiber-Reinforced Polyamide 6 Using Microcellular-Foaming-Process-Applied Injection Molding Process," *Polymers (Basel)*, vol. 14, no. 1, doi: 10.3390/polym14010173, 2022.

[184] A. Kramschuster, S. Gong, T. Li, T. Li, and L. S. Turng, "Microcellular Injection Molding of polylactide-montmorillonite nanoncomposites ," in *FOAMS* , pp. 59–63, 2006.

[185] S. A. Suarez, R. F. Gibson, C. T. Sun, and S. K. Chaturvedi, "The Influence of Fiber Length and Fiber Orientation on Damping and Stiffness of Polymer Composite Materials," 1985.

[186] M. Nofar, W. Zhu, and C. B. Park, "Effect of dissolved CO2 on the crystallization behavior of linear and branched PLA," *Polymer (Guildf)*, vol. 53, no. 15, pp. 3341–3353, doi: 10.1016/j.polymer.2012.04.054, 2012.

[187] M. Takada, S. Hasegawa, and M. Ohshima, "Crystallization Kinetics of Poly(L-lactide) in contact with pressurized CO2," 2004. Available: https://doi.org/10.1002/pen.20017. Accessed: Sep. 13, 2022. [Online].

[188] A. Ameli, M. Nofar, D. Jahani, G. Rizvi, and C. B. Park, "Development of high void fraction polylactide composite foams using injection molding: Crystallization and foaming behaviors," *Chemical Engineering Journal*, vol. 262, pp. 78–87, doi: 10.1016/j.cej.2014.09.087, 2015.

[189] S. K. Lee *et al.*, "Effect of fiber orientation on acoustic and vibration response of a carbon fiber/epoxy composite plate: Natural vibration mode and sound radiation," *Int J Mech Sci*, vol. 117, pp. 162–173, doi: 10.1016/j.ijmecsci.2016.08.023, 2016.

[190] C. J. Kim, "Comparison of mode shapes of carbon-fiber-reinforced plastic material considering carbon fiber direction," *Crystals (Basel)*, vol. 11, no. 3, doi: 10.3390/cryst11030311, 2021.

[191] O. Y. Bozkurt, M. Bulut, and O. O¨zbek, "Effect of fibre orientations on damping and vibration characteristics of basalt epoxy composite laminates," doi: 10.11159/icsenm16.115, 2016.

[192] I. Curtu, M. D. Stanciu, and V. Ciofoaia, "The modal analysis of plates made of woven composite materials ," *Buletinul AGIR*, vol. 1, 2011.

[193] N. Talekar and M. Kotambkar, "Modal Analysis of Four Layered Composite Cantilever Beam with Lay-Up Sequence and Length-To-Thickness Ratio," Available: www.sciencedirect.comwww.materialstoday.com/proceedings2214-7853, 2020. [Online].

[194] M. A. R. Shishir, Z. Zhang, D. Cai, X. Wang, and Q. Xu, "Free vibration analysis of polymer pin-reinforced foam core sandwich composite panels," *Journal of Reinforced Plastics and Composites*, doi: 10.1177/07316844221105287, 2022.

[195] J. Hou, G. Zhao, G. Wang, G. Dong, and J. Xu, "A novel gas-assisted microcellular injection molding method for preparing lightweight foams with superior surface appearance and enhanced mechanical performance," *Mater Des*, vol. 127, pp. 115–125, doi: 10.1016/j.matdes.2017.04.073, 2017.

[196] K. Yan, W. Guo, H. Mao, Q. Yang, and Z. Meng, "Investigation on foamed PP/nano-CaCO3 composites in a combined in-mold decoration and microcellular injection molding process," *Polymers (Basel)*, vol. 12, no. 2, doi: 10.3390/polym12020363, 2020.

[197] J. Crank, *The Mathematics of Diffusion*, 2nd edition. Oxford University Press, doi: 10.1021/ja01562a072, 1975.

[198] H. S. Carlslaw and J. C. Jaeger, *Conduction of heat in solids*. Oxford: Clarendon Press, 1959.

[199] P. Kjeldsen, "Evaluation of gas diffusion through plastic materials used in experimental and sampling equipment," *Water Res*, vol. 27, no. I, pp. 121–131, 1993.

[200] T. A. Osswald and G. Menges, *Materials Science of Polymers for Engineers*, 3rd ed. Hanser Publications, 2012.

[201] D. W. Van Krevenlen, *Properties of Polymers*. New York: Elsevier, 1976.

[202] W. R. Vieth, *Diffusion in and through polymers*. Munich: Hanser Publications, 1991.

[203] A. Spörrer, "Lightweight integral foams by foam injection molding with optimized materials and variothermal tools," PhD thesis, University of Kassel, Germany, 2010.

[204] C. Kastner and G. Steinbichler, "Development of measurement method for determination of dynamic solubility limits in injection foam molding," *AIP Conf Proc*, vol. 2065, pp. 1–6, doi: 10.1063/1.5088306, 2019.

[205] S.-C. Chen, M.-Y. Jien, C.-C. Hsu, S.-S. Hwang, and C.-T. Feng, "Processing Effects on the Through-Plane Electrical Conductivities and Tensile Strengths of Microcellular-Injection-Molded Polypropylene Composites with Carbon Fibers," *Polymers (Basel)*, vol. 14, no. 16, p. 3251, doi: 10.3390/polym14163251, 2022.

[206] Y. Liu, Y. Guan, X. Ye, X. Li, and J. Lin, "Effect of microstructure induced by microcellular injection molding on electromagnetic interference shielding properties," *J Appl Polym Sci*, doi: 10.1002/app.50532, 2021.

[207] R. Nobe, J. Qiu, M. Kudo, and G. Zhang, "Morphology and mechanical investigation of microcellular injection molded carbon fiber reinforced polypropylene composite foams," *Polym Eng Sci*, vol. 60, no. 7, pp. 1507–1519, doi: 10.1002/pen.25397, 2020.

[208] C. Kastner, G. Steinbichler, S. Kahlen, M. Jerabek, and T. Lummerstorfer, "Nonlinear influences of process parameters on mechanical properties of physically foamed, fiber-reinforced polypropylene parts," *J Appl Polym Sci*, vol. 137, no. 48, doi: 10.1002/app.49569, 2020.

[209] L. Wang *et al.*, "Preparation of Microcellular Injection-Molded Foams Using Different Types of Low-Pressure Gases via a New Foam Injection Molding Technology," *Ind Eng Chem Res*, vol. 58, no. 38, pp. 17824–17832, doi: 10.1021/acs.iecr.9b03330, 2019.

[210] P. Zhao *et al.*, "In-situ ultrasonic characterization of microcellular injection molding," *J Mater Process Technol*, vol. 270, no. pp. 254–264, 2019, doi: 10.1016/j.jmatprotec.2019.03.012, 2018.

[211] P. Kasemphaibulsuk, M. Holzner, T. Kuboki, and A. Hrymak, "Foam injection molding of glass fiber reinforced polypropylene composites with laminate skins," *Polym Compos*, vol. 39, no. 12, pp. 4322–4332, doi: 10.1002/pc.24512, 2018.

[212] SABIC, "Processing Guides: SABIC STAMAX," 2016.